Dedicated

to

Abel, Fatima, Marian, Sebastian and Teresa Gracias

Table of Contents

Chapter 1. Introduction

1.1 Surface mechanical properties.....1

1.2 Surface structural and chemical properties.....2

1.3 Thesis highlights..... ..2

Chapter 2. Scanning Force Microscopy- Theory and Principles

2. 1 Introduction..... ...7

2. 2. Forces in SFM..... 7

2. 3. Basic components of an SFM..... ...12

2. 4. Conclusions..... 14

Chapter 3. IR+ Visible Sum Frequency Generation (SFG) Vibrational Spectroscopy

3.1 Introduction..... 16

3.2 Theory..... 16

3.3 Experimental Considerations..... 18

Chapter 4. Quantitative measurement of the friction, elastic modulus and hardness of the surfaces of Polyethylene and Polypropylene with SFM.

4. 1 Introduction..... ..22

4. 2 The continuum force microscope: Scanning Force Microscopy with large tips. 23

4. 3 Experimental considerations..... 27

4.4 Results and Discussion:..... 43

4. 5. Conclusions.....58

Chapter 5. Modification of surface chemical and mechanical properties of Low Density Polyethylene (LDPE) by the presence of bulk additives. A combined SFG and SFM study

5. 1 Introduction..... 62

5. 2 Experiments..... 62

5. 3 Results and Discussion..... 63

5. 4 Conclusions 71

Chapter 6. Fabrication of a High Vacuum SFM to measure temperature dependent changes through the glass transition of polypropylene surfaces.

6. 1 Introduction..... ..74

6. 2 Overview of instrument..... 74

6.3 Images.....84

6.4 Conclusions..... 89

Chapter 7. Study of the Glass transition of Polypropylene surfaces by Sum-Frequency Vibrational Spectroscopy and Scanning Force Microscopy.

7.1 Introduction..... 91

7.2 Experiments..... 95

7.3 Results and Discussion.....108

7.4 Conclusions.....125

Chapter 8. Surface Studies of Polymer Blends by Sum Frequency Vibrational Spectroscopy, Atomic Force Microscopy and Contact Angle Goniometry.

8.1 Introduction.....129

8.2 Experimental..... 132

8.3 Results and Discussion..... 133

8.4 Conclusions..... 147

Chapter 9. Comparison of nano and microscale friction mechanisms on polyethylene and silicon.

9.1 Introduction..... 150

9.2 Experiments 151

9.3 Results and Discussion..... 155

9.4 Conclusions 167

Chapter 10. Miscellaneous Experiments.

10. 1 Introduction..... 170

10. 2. Electron beam damage of PMMA..... 170

10. 3 Surface modification of polymers with Diamond Like Carbon.173

10. 4 Microdeformation mechanism in Vectra-A..... 178

10. 5. Conclusions..... 180

1. Introduction

1. 1 Surface mechanical properties: The mechanical properties of bulk polymers have been extensively studied as there are many techniques which can be used to perform these measurements such as dynamic mechanical analysis, ultrasonic methods and indentation techniques[1-2]. Recently it has become possible to measure the mechanical properties of surfaces of these polymers[3]. The surfaces of polymers are crucial in controlling interfacial behavior such as adhesion, friction and biocompatibility[4]. For example polymer implants interact with the blood and body proteins at the interface of the polymer. The burgeoning field of nanotechnology implies that it will now be necessary and possible to study small structures, in which the ratio of atoms on the surface to those on the bulk is very high. It should be noted that due to surface energy and entropic effects there is evidence that the surfaces of polymers can be different from the bulk. Some of these phenomena will be addressed in this thesis.

The mechanical properties of polymer surfaces can be measured only at low loads, which can be carried out with Scanning Force Microscopy (SFM), which also provides a nano-scale level scrutiny of the polymer surface. The SFM is a generic term which includes a family of probe microscopies based on the Atomic Force Microscope (AFM) which was invented in 1986[5]. The SFM is capable of applying and measuring loads in nanonewton to micronewton load

range. By using these small loads the deformation region probed is restricted to the first 10 nm or less of the polymer surface.

Prior to the work detailed in this thesis, some methods had been developed and applied to measure (mostly qualitatively) the mechanical properties such as friction, adhesion, modulus and hardness of some surfaces.

1. 2. Surface structural and chemical properties: Many chemical and structural techniques[6] had been applied to study the surfaces of polymers. These properties are crucial in determining how a polymer surface behaves in both chemical and physical environments. Techniques that have been used include X-ray Photoelectron Spectroscopy (XPS), Secondary Ion Mass Spectrometry (SIMS), Attenuated IR spectroscopy and High Resolution Electron Energy Loss Spectroscopy (HREELS). Recently a new technique IR+Visible Sum Frequency Generation (SFG)[7] spectroscopy was developed to obtain vibrational spectra of surfaces and applied[8] to polymer surfaces. The key features of this technique are monolayer surface sensitivity, versatility, structural analysis capabilities and no vacuum requirements.

1. 3 Thesis highlights:

1. 3. 1 Quantitative measurement of the friction, elastic modulus and hardness of polymer surfaces: In this work the SFM was used for the first time to measure quantitatively the friction, hardness and modulus on polyethylene and polypropylene surfaces. The contact of the tip and the polymer surface was

found to be described by the theoretical Johnson-Kendall-Roberts (JKR)[9] model. Pressure effects under the SFM tip was demonstrated to be crucial in determining the mechanical response of the region being probed.

1. 3. 2. Use of blunt tips (radii ~1 micron) in SFM: Conventional SFM uses tips of radii of curvature of ~ 20-100 nm. The tendency has been to go towards sharper tips to obtain higher spatial resolution. However in this work we have found that the pressure under the SFM tip can be extremely high reaching values of hundreds of atmospheres even when loads as low as 1 nanonewton are applied. Hence for the first time blunt tips with radii of 1 micron have been used to do mechanical measurements with loads varying from 1 nN to thousands of nanonewtons, thereby varying the pressure at the contact by orders of magnitude. The pressure under the tip was found to affect dramatically the measured values of modulus and friction.

1. 3. 3 Combination of SFM and SFG to study polymer surfaces: SFM and SFG provide information about surfaces which can be used to complement each other. This fact was used to study various problems in polymer surface science for the first time using a combination of SFG and SFM. Strong correlations were obtained between surface structure, surface chemistry and mechanical properties of polymer surfaces. This points towards a molecular level explanation for mechanical properties. Non ideal surface phenomenon was observed on a polymer blend surface for the first time, which was explained by surface induced separation of a miscible polymer blend.

1. 3. 4 Fabrication of a novel vacuum SFM to measure temperature dependent mechanical properties: A novel SFM was built based on the STM design of Frohn et al[10] to do temperature dependent measurements. This instrument uses a head which carries the cantilever, the tip and the motion detection set-up and "walks" on the polymer sample. Temperature dependent measurements are possible with this instrument between -100 ^{0}C and 100 ^{0}C at a pressure ranging from 1 atm to 10 $^{-5}$ Torr.

1. 3. 5 Glass transition of polypropylene surfaces: SFG was used for the first time to study the changes in molecular orientation at the surface of a polymer during the glass transition. This facilitated the measurement of a surface glass transition temperature. SFM was used to measure the modulus and friction of the same polymer during the glass transition. The increased ordering of molecular chains below the glass transition temperature on the polymer surface as observed by SFG correlates well with the increased modulus measured on the same surfaces by SFM.

1. 3. 6 Comparison of frictional properties of polymers by different instruments: To understand how friction measured by different instruments from nanoscale instruments such as the SFM and macroscopic instruments such as the pin on disk compare with each other, quantitative friction measurements were done on polyethylene and silicon. These measurements were done over loads and contact areas which varied over around eight orders of magnitude.

Pressure and contact area effects were observed which puts measurements of these properties with different instruments into perspective.

In summary, during the course of the thesis it will be shown that SFM can be used successfully to measure quantitatively the adhesion, friction, elastic modulus and hardness of polymers and that these properties are strongly correlated to surface chemical and structural properties which can be probed by SFG.

Chapter 1. References:

[1] T. Murayama, *Dynamic Mechanical Analysis of Polymeric Material*, (Elsevier Scientific Publishing Company, New York 1978)

[2] H. Kausch, J. Hassell and R. Jaffee, *Deformation and Fracture of High Polymers*, (Plenum Press, New York 1973)

[3] see for example T. Kajiyama, K. Tanaka, K., I. Okhi, I. S. Ge, J. Yoon, and A. Takahara, Macromolecules **27,** 7932 (1994); R. M. Overney, E. Meyer., J. Frommer, H. J. Guntherodt, M. Fujihara, H. Takano and Y. Gotoh. Y Langmuir **10,** 1281 (1994).

[4] W. J. Feast, H. S. Munro and R. W. Richards, *Polymer Surfaces and Interfaces* (Wiley, Chichester, 1993)

[5] G. Binnig, C. F.Quate and Ch. Gerber, Phys Rev Lett. **56,** 930 (1986).

[6] D. P. Woodruff and T. A. Delchar *Modern techniques of surface science* 2nd ed (Cambridge University Press, New York 1994).

[7] Y. R. Shen, Nature, **337**, 519 (1988) .

[8] D. Zhang, R. Ward, Y. R. Shen, and G. A. Somorjai, J. Phys. Chem. **101,** 9060 (1997)

[9] K. L. Johnson, Contact Mechanics (Cambridge University Press,1985).

[10] J. Frohn, J.F. Wolf, K. Besocke and M. Teske, Rev. Sci. Instrum. **60**, 1200 (1989).

2. Scanning Force Microscopy-Theory and Principles

2. 1 Introduction: Following the invention of the Scanning Tunneling Microscope[1] (STM), a family of scanning probe microscopies have been developed[2]. In all of these microscopies, a probe is spatially scanned relative to the surface. The probe interacts with the surface through various potentials which can be both intrinsic (Van Der Waals, repulsive contact) or induced by applied electric or magnetic fields. In Scanning Force Microscopy (SFM)[3], the interaction between the probe and the surface is measured in terms of forces.

2. 2 Forces in SFM: Some of the commonly encountered forces that are observed in SFM are[4],

2. 2. 1 Van Der Waals (VDW): The VDW force is an attractive force that exists between all atoms and molecules. This interatomic pair potential can be expressed in the form $w = -\frac{A}{d^6}$ where A is a constant, and d is the separation distance between the two single atoms.

However in the SFM experiment the end of the tip consists of many atoms which interact with many atoms on the surface. If we assume that this interaction is nonretarded and additive, we can integrate over these various pair interactions present in various geometries of the tip and the surface, to obtain an expression for this potential between macroscopic bodies of different shapes. If we model the probe in SFM as a sphere of radius R and the surface as a flat plane, we obtain an expression of the form,

$w_{SPHERE-PLANE} = -\frac{HR}{6d}$ where H is called the Hamaker constant, defined as,

$H = \pi^2 A \rho_1 \rho_2$, A is the constant of the pair potential (above) and ρ_1 and ρ_2 are the atomic number densities of the two interacting bodies.

The VDW force can be obtained by differentiating and is given by,

$$F_{SPHERE-PLANE} = -\frac{HR}{6d^2}$$

For a hydrocarbon, $H = 0.5 \times 10^{-19} J$ and the force felt by a probe of radius $R = 100nm$, at a distance 1 nm from the surface ~ 1nN and the force constant of the interaction is ~ 1.6 N/m. In contrast, the force constant for the stretching of a C-H bond in methane[5] is 544 N/m.

2. 2. 2 Adhesive Forces: When the probe is in contact with the surface, an adhesive force is needed to separate the two bodies.

For a sphere in contact with a flat surface, the adhesive force can be approximated as $F_A = 4\pi R\gamma$, where γ is the interfacial energy.

For polystyrene, γ = 33 mJ/m^2 , the adhesive force = 41Nn for a tip of radius $R = 100nm$.

2. 2. 3 Capillary Forces: In the presence of humidity or contaminants at a surface, capillary forces are exerted whose magnitude is given by $F_c = 4\pi R\gamma \cos\theta$.

Assuming a contact angle $\theta = 0^0$, and a tip radius, $R = 100nm$.

for water which has a surface tension $\gamma = 73mJ/m^2$, the capillary force = 92nN

For a contaminant, (e.g. a hydrocarbon) $\gamma = 25mJ/m^2$, the capillary force = 31nN.

2. 2. 4 Electrostatic forces: The electrostatic force arises when a bias voltage is applied between the tip and the surface and is a long range force. When the radius of curvature of the tip R > d (the distance between the tip and the sample), the force can be approximated as,

$F_e \cong \frac{3RV^2}{d} \times 10^{-11} N$, where V is the voltage applied between the two surfaces.

For V = 1 Volt, d=1nm, $R = 100nm$, the force = 3nN.

2. 2. 5 Force required to break a covalent bond: The repulsive force required to break a chemical bond can be estimated as follows. A typical covalent bond, for e.g. a H_3C-CH_3 bond has a bond energy of ~376 KJ/mole[5]. We can assume that if we stretch the bond by a distance equal to its bond length ~ 0.1 nm it will break. This translates to a force of around 4 nN. With the SFM, forces of nanonewtons to micronewtons can be applied over several square nanometers to several square microns. We can thus remain in an elastic regime (do not break bonds) or in a plastic regime (break bonds).

2. 2. 6 Contact forces (mechanics): Different continuum mechanics models can be used to describe the physical contact of the tip and the surface, the three models widely used are,

2. 2. 6 . 1 The Hertz model[6]: The earliest solution to the analysis of stresses at the contact of two elastic solids was given by H. Hertz. The solution is valid when the radius of contact between the two solids (r) is small compared to the relative radius of curvature of the two solids (R) i.e. ($r << R$). Hertz also assumed that the surfaces were frictionless and neglected adhesion between them. The Hertz solution for the contact of a half sphere and a planar surface (which can be assumed to be the situation in SFM) gives,

$\Rightarrow$ the contact area, $a = \pi\left(\frac{3WR}{4E^*}\right)^{2/3}$; radius of contact, $r = \sqrt{\frac{a}{\pi}}$

$\Rightarrow$ the penetration depth of the sphere into the surface, $\delta = \frac{a^2}{R} = \left(\frac{9W^2}{16RE^{*2}}\right)^{1/3}$

$\Rightarrow$ and the mean pressure at the contact, $p_m = \frac{W}{\pi a^2} = \frac{2}{3}\left(\frac{6WE^{*2}}{\pi^3 R^2}\right)^{1/3}$

where W is the load applied,

and E^* is the modified elastic modulus defined as $\frac{1}{E^*} = \frac{1-\nu_1^2}{E_1} + \frac{1-\nu_2^2}{E_2}$

ν_1 and ν_2 are the Poisson ratios of the two solids, and E_1 and E_2 are the elastic moduli of the two solids. (When a material is stretched in one direction it contracts in a direction at right angles to the direction of stretching, this ratio is the Poisson ratio of the material. It is always a positive number less than 0.5)

2. 2. 6. 2 The JKR model[7]: In 1971, Johnson, Kendall and Roberts analyzed the influence of surface energy on the contact of elastic solids. After including

the interfacial surface energy γ, the authors obtained expressions for,

$$\Rightarrow \text{the contact area, } a = \left[\frac{3\pi^{3/2}R}{4E^*}.\left[W + 3\pi R\gamma + \sqrt{6\pi R\gamma W + (3\pi R\gamma)^2}\right]\right]^{2/3}$$

{Note: If we neglect the surface energy (i.e. $\gamma = 0$) in the above expression we get an expression identical to that obtained by Hertz (2.2.6.1)}

We can observe from above that there is a finite contact area,

$a_0 = \pi\left(\frac{9\pi\gamma R^2}{2E^*}\right)^{2/3}$ even at zero load (i.e. $W = 0$)

2. 2. 6. 3 The DMT theory[8]: Deraguin, Muller and Toporov include the surface energy into the Hertz model, by assuming that the Hertz deformation profile is mantained, but that the contact area is increased and is given by,

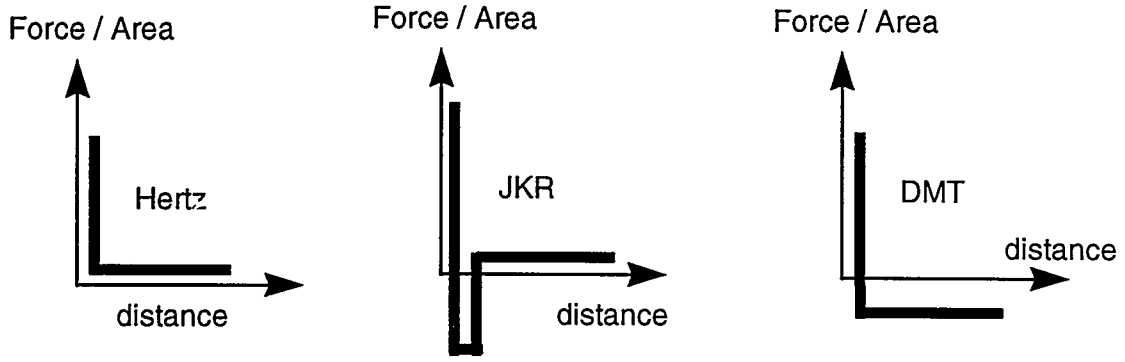

Figure 2.1 A schematic of the interaction force for the Hertz, JKR and DMT models.

$$a = \pi \left[\frac{3R}{4E^*} \left(W + 2\pi\gamma R \right) \right]^{2/3},$$

{Note: If we neglect the surface energy (i.e. $\gamma = 0$) in the above expression we get an expression identical to that obtained by Hertz (2.2.6.1)}

2. 2. 6. 4 Comparison of the Hertz, JKR and DMT models:

The interaction forces (normalized per unit area) for the three models are sketched in Figure 2.1[9] As can be seen in the figure the Hertz model totally neglects any attractive forces, and hence works well when large repulsive loads are applied or for negligible attractive forces ($\gamma = 0$). The JKR theory works well for soft solids, (small elastic modulus) with high surface energy and large contact radii. Alternatively the DMT theory works well for hard solids (large elastic modulus) with low surface energy and smaller radii of contact.

2. 3 Basic Components of an SFM: All SFM's contain the following components:

2. 3. 1 Scanning elements: In order to map out the spatial dependence of properties on a surface, it is necessary to move the probe relative to the sample with extreme precision on the nanometer scale. This is commonly achieved by piezoelectric materials. Piezoelectric materials are a class of non-centrosymmetric, crystalline materials. When a mechanical pressure is applied to these materials, the structure produces a voltage proportional to the pressure. Conversely when an electric field is applied to these materials a dimensional change in the material is achieved. Exact dimensional changes depend on the

shape, material and poling characteristics of the piezoelectric, typically a change of 10nm / Volt is observed.

2. 3. 2 Force Detection: The interaction force between the probe and the sample is measured by noting the displacement of a sensitive cantilever (Force constants 0.05 N/m to 300 N/m) to which the probe is attached. The displacement is measured by focusing a laser beam on the back side of the cantilever and using either optical interferometry or a position sensitive photodiode to monitor the movement of the laser spot.

2. 3. 3 Feedback electronics: The SFM can be used in an open loop configuration to generate a spatial map of a property. Alternatively in many cases some property measured (e.g. Van Der Waals or contact forces) is compared to a set value. The difference or the error signal is then used to control the distance of the probe and the sample through a feedback signal. Thus by using a closed loop circuitry a topographic map of the surface can be generated.

2. 3. 4 Noise damping components: If a signal has to be measured with angstrom resolution extreme care must be taken to reduce noise in the system.

The chief sources of noise are mechanical vibrations of the components, building vibrations, electronic noise and statistical noise.

2. 3. 5 Cantilever and tip: The force constant of the cantilever determines the sensitivity of the instrument. Cantilevers can either be prepared by using thin

wires, or microfabricated using conventional lithographic techniques. In this way cantilevers of different shapes (rectangular, triangular etc.) can be prepared, with force constants ranging from milli N/ m to hundreds of newtons/ m. As was seen in section 2.2, the tip shape and radius is important in determining the magnitude of the interaction between the tip and the surface and in general spherical or parabolic terminated tips are used.

2. 4 Conclusions : In this chapter, a brief outline of the critical issues in SFM was presented. In the experiments which will be described later in the text, it was necessary to use a total of three different SFM's (two of which were home-built) with different capabilities, and the specifics of these instruments will be described in detail later.

Chapter 2. References

[1]G. Binnig and H. Rohrer, Helvetica Physica Acta **55**, 6, 726 (1982).

[2] S. Dror, *Scanning force microscopy : with applications to electric, magnetic, and atomic forces* (Oxford University Press, New York, 1994)

[3] G. Binnig, C. F. Quate and Ch. Gerber, Phys. Rev. Lett. **12**, 930 (1986)

[4] J. N. Israelachvili, *Intermolecular and surface forces* (Academic Press, London, 1985)

[5] *CRC Handbook of Chemistry and Physics* edited by D. Lide (CRC Press, New York, 1998)

[6] H. Hertz, J. Reine Angew. Math. **92**, 156 (1881)

[7] K. L. Johnson, K. Kendall and A. D. Roberts, Proc. R. Soc. Lond. A. **324**, 301 (1971)

[8] B. V. Derjaguin, V. M. Muller and Y. P. Toporov, Journal of Colloid and Interface Science **67**, 314 (1975)

[9] R. W. Carpick, *The Study of Contact, Adhesion and Friction at the Atomic Scale by Atomic Force Microscopy* (Ph.D. Thesis, U.C. Berkeley, 1997)

3. IR+Visible Sum Frequency Generation (SFG) Vibrational Spectroscopy.

3. 1 Introduction: Since the observation of second harmonic generation by Franken et al[1], non-linear optics has been widely used as a spectroscopic tool to study surfaces[2]. Sum Frequency Generation (SFG)[3] is a second order non-linear optical effect which involves the mixing of two input waves of different frequencies to generate a third beam at the sum frequency of the two beams.

3. 2 Theory:

3. 2. 1 Surface sensitivity of SFG[4]: The second order non linear polarization which is the source of SFG is given by,

$\vec{P}^{(2)}(\omega) = \vec{\chi}^{(2)}(\omega = \omega_1 + \omega_2) : \vec{E}(\omega_1)\vec{E}(\omega_2)$, where $\vec{\chi}^{(2)}$ is the second-order nonlinear susceptibility tensor. In general the tensor depends on the material properties of the medium and for SFG has 27 terms. Since the tensor has an odd number of indices (an even order process), under the dipole approximation, it necessitates that the tensor vanish in a centrosymmetric medium. This is because under inversion symmetry in a centrosymmetric medium $\vec{\chi}_{ijk}^{(2)} = -\vec{\chi}_{ijk}^{(2)}$, which is possible if and only if $\vec{\chi}_{ijk}^{(2)} = 0$ Since centrosymmetry is necessarily broken at an interface, SFG is *surface sensitive*, even in the presence of a centrosymmetric bulk (which contributes only to quadrupole and higher order terms).

3. 2. 2 Efficiency of the process: To estimate the relative magnitude of the anharmonic terms (which are responsible for SFG) and the harmonic terms we note that the atomic field is of the order of ~ 3 x 10^8 V/cm. For the external laser field to induce significant higher order terms in a perturbation expansion, its magnitude must be on the order of the atomic field. Thus high power laser beams are required to observe non linear optical effects, this is why pulsed picosecond lasers are typically used.

3. 2. 3 Spectroscopy: The sum frequency signal from a surface can be written as composed of resonance and non-resonance components of the non linear susceptibilites as[5],

$$I_{SFG} \propto \left|\chi_{NR}^{(2)} + \chi_{R}^{(2)}\right|^2,$$

The resonant component can be obtained by perturbation theory which yields the following expression,

$\chi_R^{(2)} = \dfrac{B_v}{\omega_p - \omega_{IR} - i\tau_v}$ where τ_v is a relaxation constant which describes the homogeneous broadening of the vibrational response. B_v is an intensity factor which can be written as the product of the infrared transition moment, A, and the Raman transition moment, M, averaged over the orientation of the molecules as,

$$\left(B_v\right)_{ijk} = \frac{2\pi}{h} N \sum_{lmn} \left\langle \left(\hat{i}.\hat{l}\right)\left(\hat{j}.\hat{m}\right)\left(\hat{k}.\hat{n}\right)\right\rangle M_{lmn} A_n$$

Thus we note that there will be resonance enhancement when $\omega = \omega_{IR}$. Also we observe peaks only for modes for which the Raman and IR modes have non zero moments, i.e. only for the modes which are Raman and IR active.

3. 3 Experimental Considerations: The experimental arrangement for sum-frequency generation from an interface is shown in fig. 3.1.

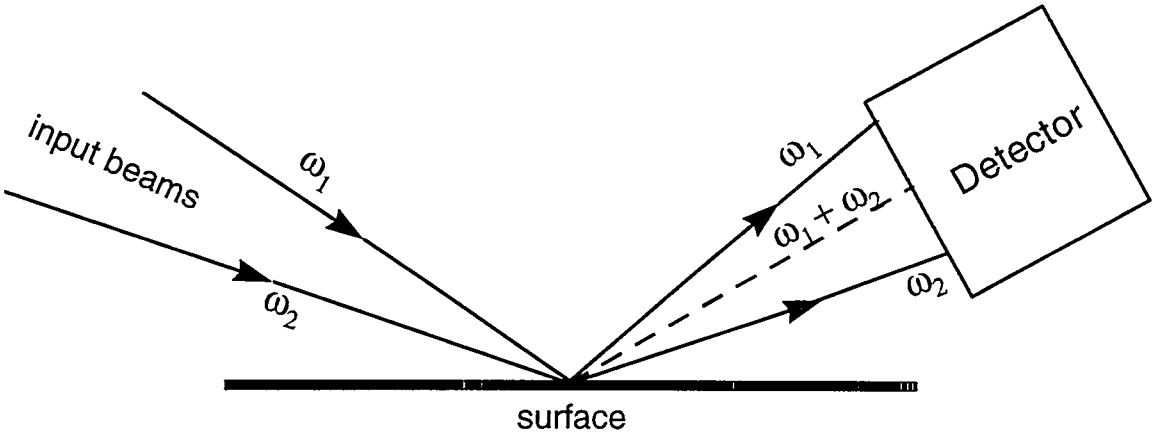

Figure 3. 1 A schematic diagram of the experimental set-up for SFG.

The SFG experiments were performed by using a visible beam and a tunable infrared beam as the input beams. The polarization quadratic in the electric field leads to the optical phenomena of second harmonic generation, sum and difference frequency mixing as well as rectification[6]. However in the current experiment only the SF signal is collected while frequency tuning the infra-red beam. Since the SF signal is in the visible Photo Multiplier Tubes (PMTs) may be used to detect the SF signal.

3. 3. 1 Input Beams: The laser used to generate both the visible and IR input beams was a Nd:YAG picosecond laser. The pulses have a width of 25 ps at 1064 nm and an energy of 40mJ per pulse.

3. 3. 1. 1 The Visible beam: The visible beam was generated by frequency doubling the 1064 beam through a KD*P non linear crystal to generate a 532 nm green beam by second harmonic generation.

3. 3. 1. 2 The tunable IR beam: The tunable infrared beam (tunable between 4000 and 2600 cm^{-1}) was generated via a $LiNbO_3$ optical parametric generation and amplification stage. (OPG/ OPA) depicted in figure 3.2. A fundamental beam at 1064 nm with an energy of 2 mJ/pulse passes through a $LiNbO_3$ crystal and generates weak idler and signal beams with a total energy of 30 microJoules. The signal beam and a delayed second 1064 beam (8 mJ/pulse) are then combined in a second $LiNbO_3$ crystal which puts out a tunable infrared beam with an energy of 300 microjoules. Frequency tuning is achieved by angle tuning $LiNbO_3$ crystals to change the phase matching condition for parametric generation which is determined by the refractive indices of the crystal at the three frequencies.

3. 3. 2 Detection: The signal was detected by a Hamamatsu R647-04 photomultiplier tube, then converted to a voltage and sent to a box car integrator and stored on a computer.

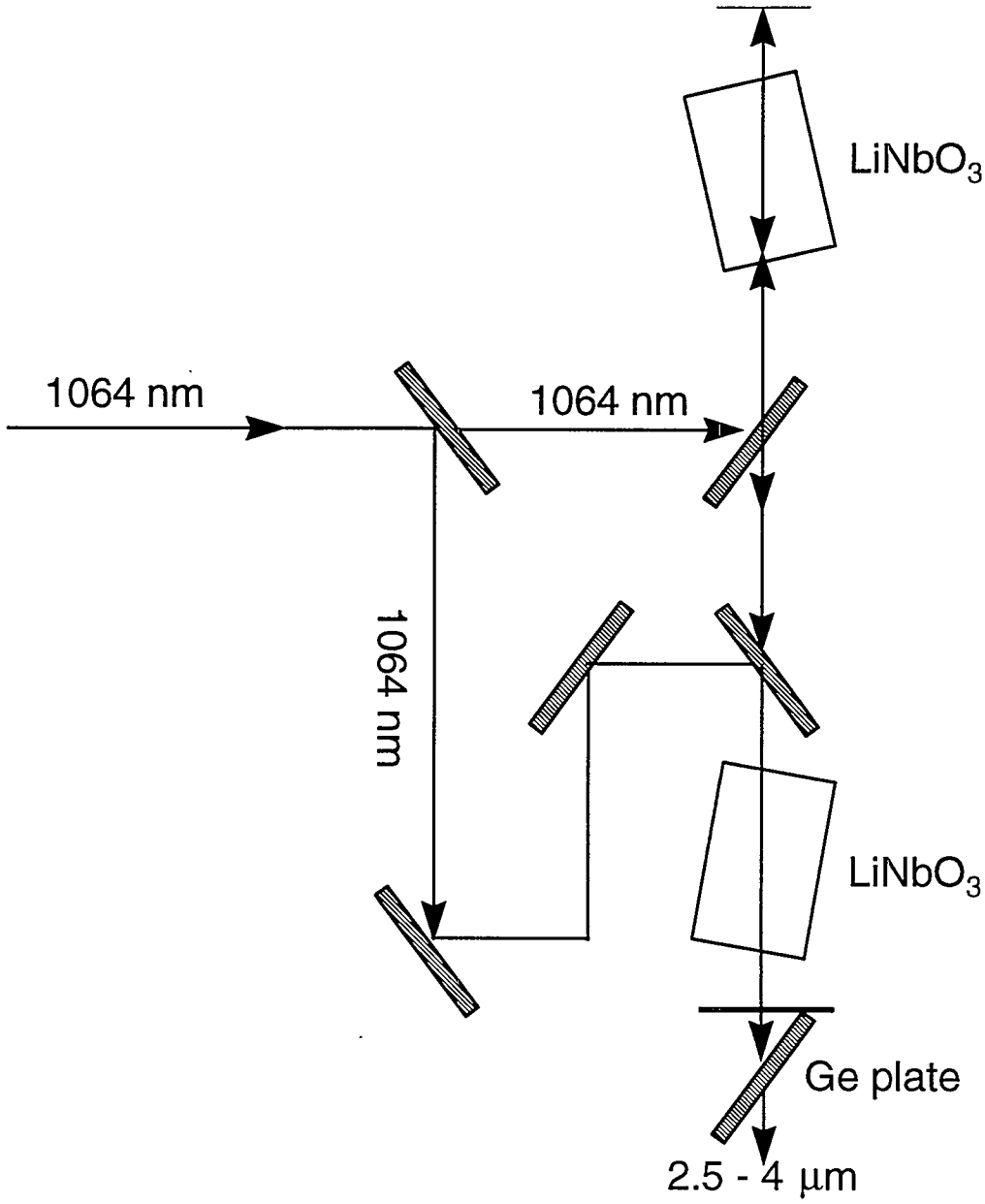

Figure 3. 2 Schematic of OPG/OPA composed of $LiNbO_3$ used to generate tunable infrared light.

Chapter 3. References:

[1] P. Franken, A. E. Hill, C. W. Peters and G. Weinreich, Phys. Rev. Lett. **7**, 118 (1961)

[2] Y. R. Shen, Surface Science **299/300**, 551 (1994)

[4] Y. R. Shen, *The Principles of Nonlinear Optics* (J. Wiley, New York, 1984)

[5] C.D. Bain, P.B. Davies, T. H. Ong, R. N. Ward and M. Brown, Langmuir **7**, 1563 (1991)

[6] N. Blombergen, Reviews of Modern Physics **54**, 3, 685 (1982)

4. Quantitative measurement of the friction, elastic modulus and hardness of the surfaces of Polyethylene and Polypropylene with SFM.

4. 1 Introduction: The SFM had been previously used to measure elastic modulus, hardness and friction on many systems[1-5]. However in these measurements conventional tips with radii of curvature << 0.1 micron were used. As will be described in this chapter, the pressure under the SFM tip is extremely high even at small loads and depends very strongly on the radius of curvature of the tip. While working on soft materials like polymers it is important to keep the pressure in the contact region low, in order to do meaningful experiments without considerable deformation of the polymer surface. To reduce the pressure at the contact, we must use blunt tips, thereby sacrificing spatial resolution, but keeping the pressure low. In the present study, we have used for the first time, a tip with a large radius of curvature (1 micron). The mean pressures being applied are considerably lower than similar experiments done with the SFM till date[1-5]. By using a tip of a large radius, however, we are now measuring continuum and not atomic forces and this justifies the term "continuum force microscopy" (CFM).

The polymers studied were low and high density polyethylene, (LDPE and HDPE), and isotactic and atactic polypropylene (IPP and APP). The reason for studying the above polymers is that they provide fundamental systems for studying the effect of density, tacticity, and crystallinity on the mechanical

properties of polymer surfaces composed of similar hydrophobic monomer units (made up of carbon and hydrogen only).

In order to do a systematic study of the surface mechanical properties, thereby justifying a comparison of the relative mechanical properties based on the intrinsic properties of the polymer, we have reduced the number of variables affecting the measurements. The polymers were processed in the same manner and characterized extensively. Special care was taken to prepare smooth surfaces, the mechanical measurements were done on all the polymers using the same well calibrated experimental set up, i.e. the same tip, the same environment, and at the same velocity/frequency.

To our knowledge this is the first quantitative measurement of the elastic modulus, hardness and friction of polyethylene and polypropylene in this load regime. We have measured the radius of the tip accurately and have applied continuum contact mechanics to explain the experimental results.

4. 2 The continuum force microscope: Scanning force Microscopy with large tips: In order to understand the fundamental differences between the use of tips with small radii of curvature and tips of large radii of curvature, the mean contact pressure, contact radius and penetration depth are plotted as a function of load for three tips of radii 20 nm, 100 nm and 1000 nm in Figs. 4. 1, 4. 2 and 4. 3.

These curves were plotted using Hertzian contact mechanics[6], discussed in section 2. 2. 6. 1.

4. 2. 1. Contact Pressure: From Fig. 4.1, we observe that the pressure is extremely high under the SFM tip, even at very small loads, which is due to the small area of contact. The pressure is more sensitive to the radius of the tip than to the load. Since the polymers studied have yield stresses in the range of 50-1000 atm, the pressures typically applied in SFM are very close to the yield stresses of polymers. However if we apply the same small loads with tips of

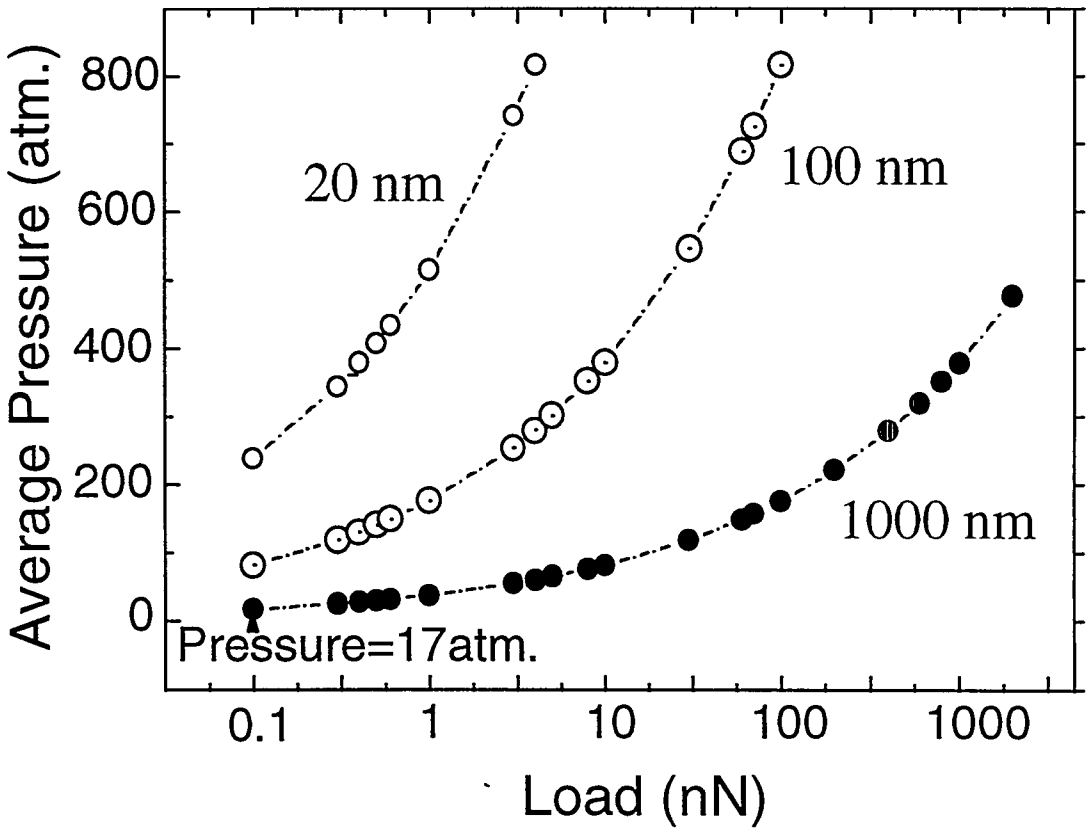

Figure 4.1 A plot of the contact pressure under the SFM tip vs load for three tips of radii of curvature 20 nm, 100 nm and 1000 nm.

larger radii we can do the same measurements by applying lower pressures thereby staying below the yield strengths of the polymers.

4. 2. 2. Radius of Contact: As we increase the radius of curvature of the tip, we make contact with a larger area on the surface at the same loads. This decreases the spatial resolution of imaging. Thus if it is necessary to image the surface with high resolution, sharp tips and high pressures are necessary. However in this work average spatial measurements of the surface friction,

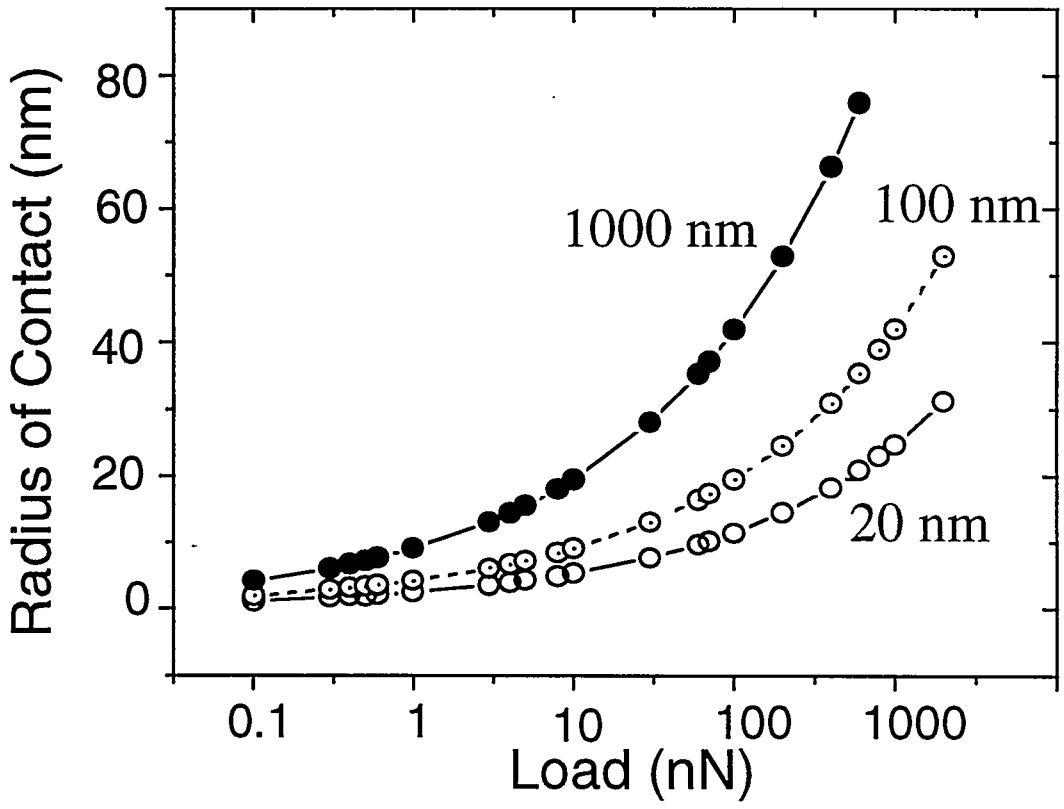

Figure 4. 2 A plot of the radius of contact vs load for three tips of radii of curvature 20 nm, 100 nm and 1000 nm.

modulus and hardness were of importance, and the large areas of contact were helpful. Polymers are inhomogenous, and consist of crystalline and amorphous domains. Hence if a spatially independent property is to be measured considerable spatial averaging must be done to get any kind of reproducibility. By using tips of large radii of curvature, the measurement averages over a large spatial region and we can comment more accurately on the average values for

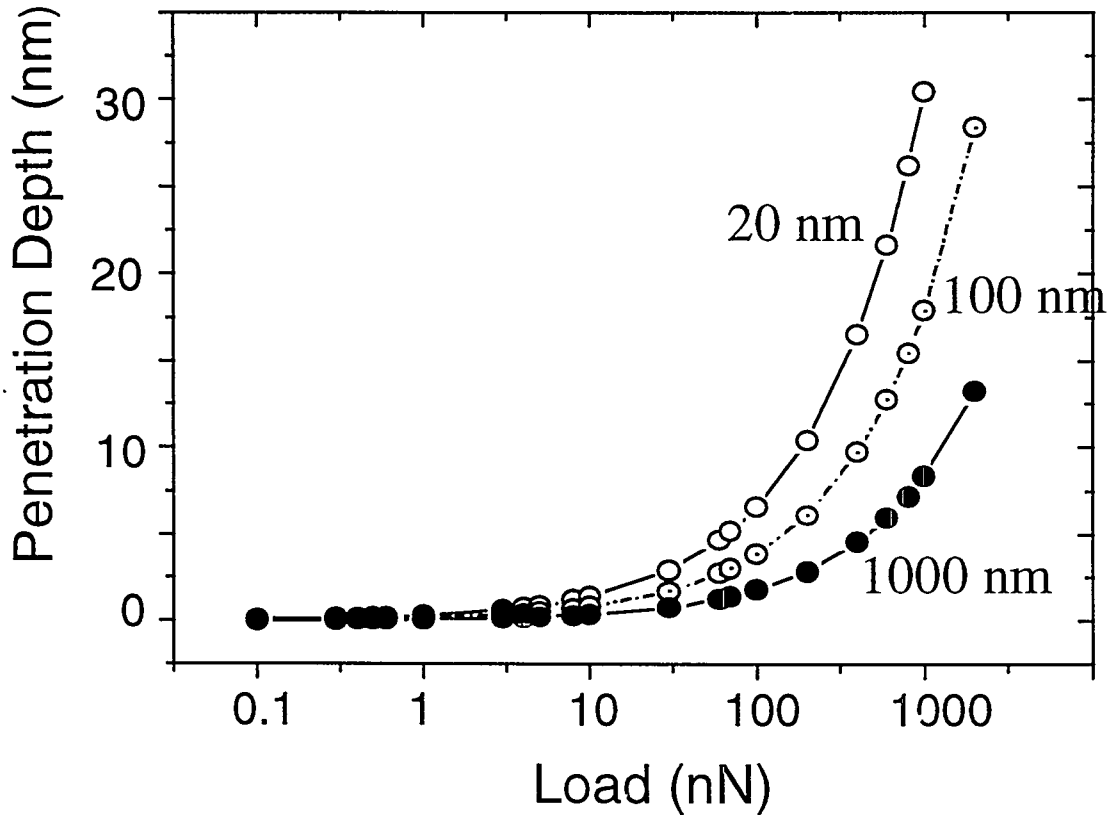

Figure 4.3 A plot of the penetration depth of the SFM tip vs load for three tips of radii of curvature 20 nm, 100 nm and 1000 nm.

the surface.

4. 2. 3 Penetration Depth: The whole purpose of the measurements is to be surface sensitive. Bulk values of mechanical properties have been well established. The penetration depth of the tip into the surface determines the spatial sensitivity of the measurement. By using tips of large radii of curvature, we have lower penetration depths for the same load, or are more surface sensitive as can be seen in Fig. 4.3

4. 3. Experimental considerations:

4. 3. 1. Sample Preparation: It is necessary to prepare smooth surfaces for the measurement of mechanical properties. This is illustrated by the effect of topography in the measurement of friction shown in Fig. 4.4.

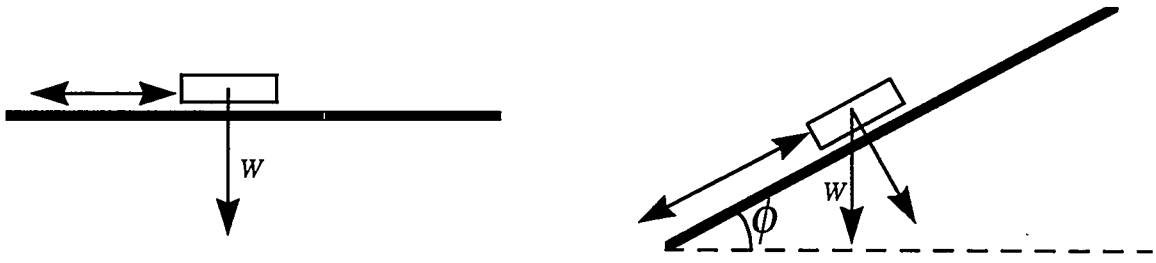

$Friction \propto W$ $Friction \propto W \cos\phi$

Figure 4. 4 The friction force felt while moving on a tilted surface is different from that felt on a flat surface.

Thus as the tip moves over different tilted surfaces (micro and nano asperities) a topographic effect is introduced. Hence special care was taken to prepare smooth surfaces of LDPE, HDPE, IPP and APP. The polymers were purchased from Aldrich in the form of pellets. They were then melted on a Pyrex glass plate in air while pressing on them with a weight of around 10 kilograms for an hour. The polymers were cooled by taking them off the hot plate. The polymer cools to room temperature in around 20 minutes. The polymer was then peeled off.

The surface of the polymer in contact with the glass plate molds to the surface roughness of the glass and was used for the measurement of the mechanical properties. The roughness of the surfaces were measured by imaging the surfaces of these polymers with a commercial Atomic Force Microscope, (Park Scientific Autoprobe) using ultralevers with radii of curvature of the order of 20nm. The r.m.s roughness is around 20nm on a 60 micron x 60 micron scale. (On an area of 200nm x 200nm, the r.m.s roughness is <1nm. (Fig. 4.5)).

The chemistry of the surface was analyzed by **X**-ray **P**hotoelectron **S**pectroscopy (*X*PS)[7] with a Perkin Elmer ESCA 5000 series instrument. XPS is a surface sensitive technique (probing depth< 0.1 micron) providing chemical information in the form of core level electronic excitation peaks characteristic of the chemical environment of the surface. A carbon and oxygen peak were seen. The amount of oxygen on the surface is small (<5%). The oxygen is there because the sample was heated in air. However no other contaminant like Si or Na from the glass was observed.

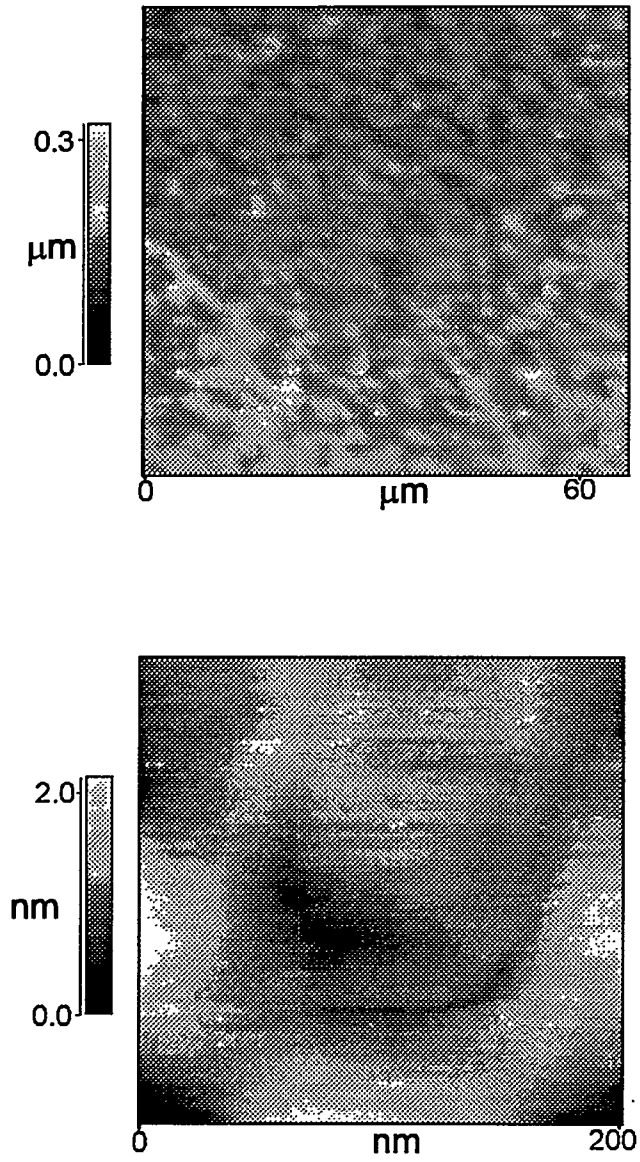

Figure 4.5. A (60 micron)^2 topographic image of the LDPE with a surface R.M.S. roughness of 18nm (above); and a (200 nm)^2 topographic image of the same surface with an R.M.S. roughness of 0.5 nm (below).

The contact angle of methylene iodide and water was measured on the polymer surfaces using a Rame-Hart contact angle goniometer, and was found to be approximately 95 and 52 degrees respectively on all the polymers. These

POLYMER	Properties of the original Polymer Obtained From the Supplier	% Crystallinity after molding
Low Density Polyethylene (LDPE)	Density = 0.92 g/c.c. T_m= 115 °C	~23
High Density Polyethylene (HDPE)	M_w=125x10^3g/mol, T_m=131°C Density = 0.95g/c.c	~65
Isotactic Polypropylene (IPP)	M_w=250x10^3g/mol T_m=189°C, T_g= -26°C Density = 0.90g/c.c	~ 63
Atactic Polypropylene (APP)	Viscosity= 23 poise T_g= -10°C	<2

Table 4.1. Listed in the table are the polymers used in the experiments and their properties, the % Crystallinity was obtained by measuring heats of fusion of the final sample, i.e. after molding, by DSC in our laboratory.

values are in agreement with literature values for the polymers[8-10] It was observed that we could make smoother surfaces when the polymer was molded against a mica surface (which is a flatter surface than glass), however this method yielded polymer surfaces which were contaminated by Si or Na and hence was not used.

The percentage crystallinity of the processed film was determined by measuring heats of fusion by **D**ifferential **S**canning **C**alorimetry (DSC)[11] on a Perkin Elmer (DSC 7) Differential Scanning Calorimeter. The heats of fusion were determined by integrating the peaks obtained on the resulting polymers at the melting point. The ratio of the heat of fusion measured to the heat of fusion of a 100% crystalline sample gives an approximate measure of the % crystallinity of the sample. The heats of fusion for 100% crystalline polyethylene and polypropylene used were 295.8 J/g and 208.8 J/g respectively[12]. HDPE and IPP are highly crystalline materials as opposed to LDPE and APP. This is expected as an increase in density from LDPE to HDPE (a decrease in side branches) promotes the possibility of the polymer to form well packed crystalline structures. Isotacticity in IPP also promotes order as the chains can pack better with well defined methyl stereoorientation[13].

4. 3. 2 The Instrument: Since the crucial part of this work was to measure *quantitative* values for the elastic modulus, hardness and friction, it was necessary to use a scanning force microscope which could be calibrated

accurately. This is a very cumbersome task with the conventional detection scheme used in commercial SFM's which employ a photosensitive diode to detect a laser spot bounced off the back side of the cantilever. Briefly our instrument uses optical interferometry to detect[14] the motion of the cantilevers shown in Fig. 4.6. A well cleaved optical fiber is impinged on the back of the cantilever so that the edge of the optical fiber is parallel to the cantilever and at a distance d from it. This is done using an optical microscope. The distance d is adjusted to be as small as possible to maximize the light reflected off the cantilever back into the optical fiber. However if d is too small, the optical fiber

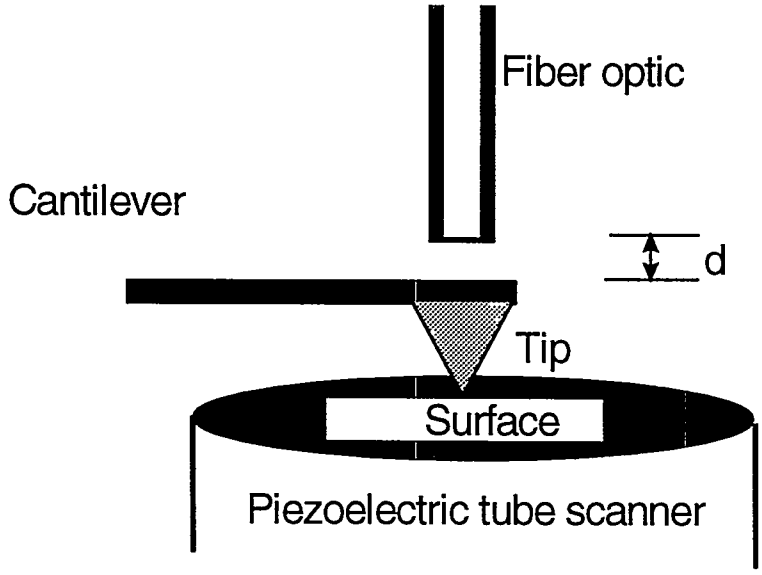

Figure 4. 6 : Schematic diagram of the fiber-optic interferometer SFM.

may physically touch the cantilever, thereby damaging the end. Around 4% of the light which is reflected back into the optical fiber at the glass-air interface

interferes with the light reflected off the cantilever. The difference in the distance traveled by these two beams is equal to $2d$.

We thus get constructive interference of light if, $2d = n\lambda$ and destructive interference if, $2d = \frac{m\lambda}{2}$ where λ is the wavelength of the light used, in our case 780 nm (red light). If we measure the light falling on a photodiode at the back side of the optical fiber and plot a voltage we get a periodic dependence

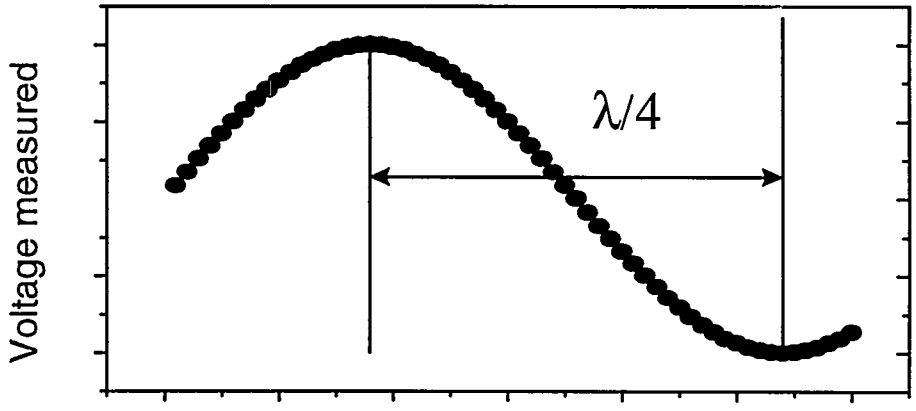

Figure 4.7 Periodic dependence of voltage on the distance between the edge of the fiber and the cantilever.

on the distance d. When d changes by $\frac{\lambda}{4}$ (195 nm) the signal goes from a maximum to a minimum as shown in Fig. 4.7. Thus calibration of distances is made against the wavelength and is very accurate. Also the normal and lateral forces are measured independently by two separate fiber-optic cables, hence the signals measured for the vertical and horizontal displacement of the

cantilever are independent of each other. The cantilever is prepared by bending a tungsten wire at a right angle and etching the end to a sharp tip. The resonance frequency of the cantilever was measured from its response to a driving oscillation at different frequencies, and was found to be 16KHz. The force constant was then calculated from the resonance frequency, diameter, and the density and elastic modulus of bulk tungsten. The cantilever was approximated as a cylinder of circular cross-section, clamped at one end and free at the other, and the following equations were used[15],

for the force constant, $k = \frac{3ED^4\pi}{64L^3}$

and the resonance frequency, $\nu = 0.327\sqrt{\frac{k}{m}} = 0.327\sqrt{\frac{4k}{L\rho\pi D^2}}$

where D is the diameter of the cantilever, which was measured with a micrometer. ρ is the density (19254 kg/m^3) and E is the elastic modulus of bulk tungsten (407 GPa)[16].

We can back calculate the length of the cantilever from the above treatment, and measure the length independently to check for any discrepancies. The force constant of the tip was calculated to be 235N/m($\pm 15\%$). The primary error comes from the measurement of the diameter; this is because the force constant of the tip scales as the diameter to the fourth power.

In all experiments, the sample was moved with respect to the tip, using a piezoelectric tube. All measurements were done while purging the chamber with dry nitrogen to avoid capillary condensation of water at the contact between the

tip and the surface.(Section 2. 2. 3) Humidity levels are below 10% when this is done.

4. 3. 3 Radius of the tip: The radius of the tip was measured by imaging the stepped surface, (305) of strontium titanate[17] in the contact mode. The ridges on this surface are sharper than the tip and hence the image obtained reflects the tip profile as shown in Fig. 4.8. This is a good method to determine the radius since, the radius is obtained under scanning conditions. The radius was determined by fitting a parabola to the features scanned and extracting a

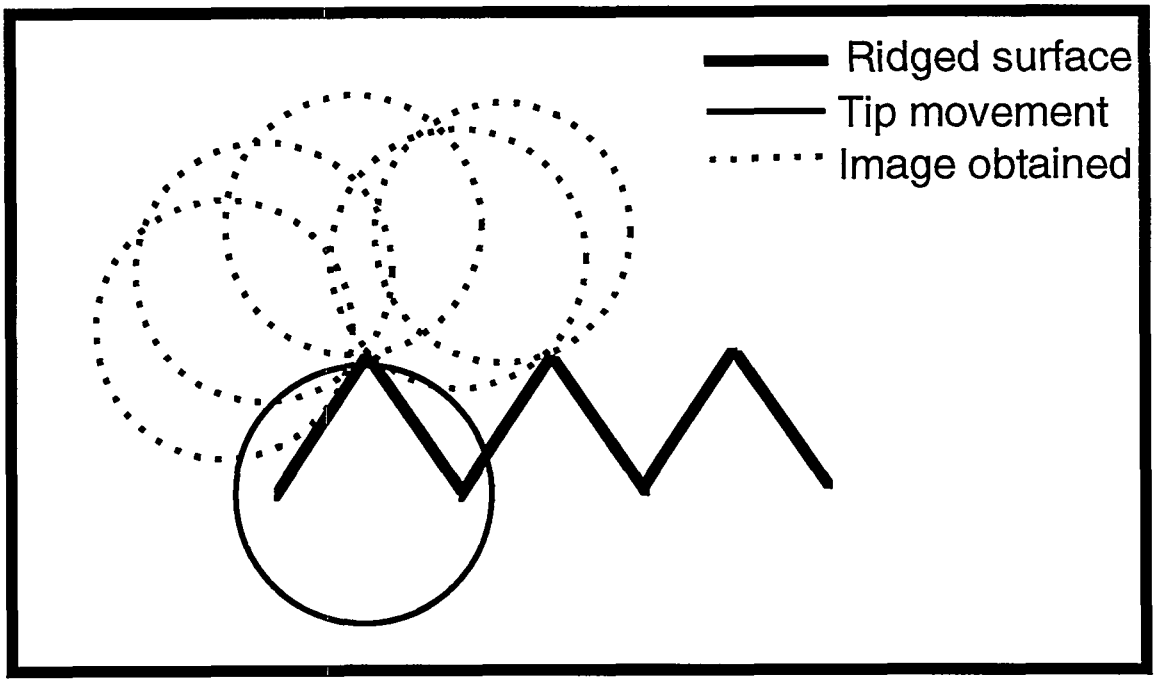

Figure 4.8: An illustration of how the radius of the tip is obtained by scanning a tip over a sharp ridged surface.

radius of curvature of 1000nm.

4. 3. 4 Measurement of elastic modulus: To measure the elastic modulus of the sample the cantilever was oscillated at a frequency (1.5KHz) far below its resonance frequency (16KHz) with an amplitude of 1-1.5nm. This was done by applying an AC signal to a piezoelectric chip on which the cantilever was

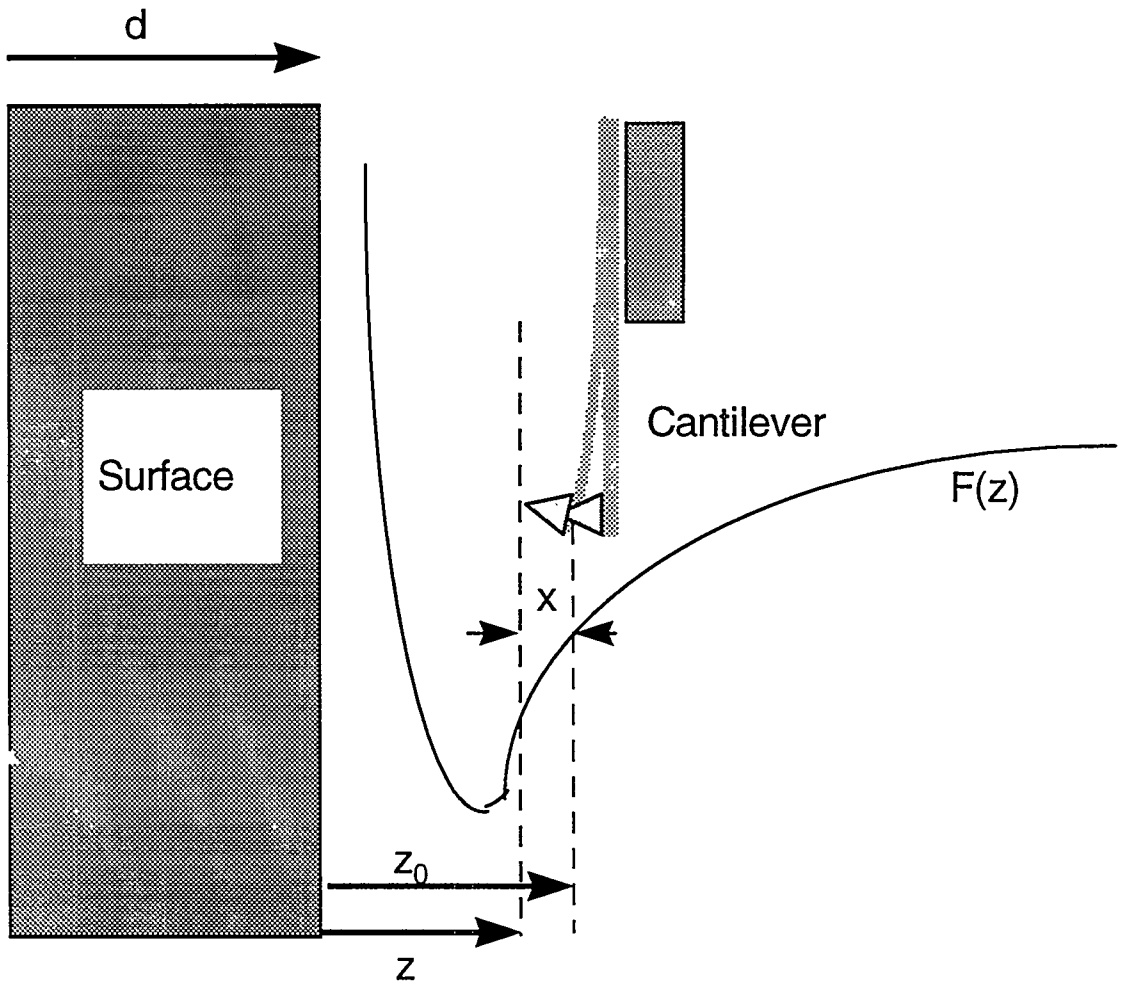

Figure 4.9: Schematic of the oscillation of the cantilever while it interacts with a force field $F(z)$.

mounted. When the tip feels an interaction force, the amplitude of the oscillation differs from the driving amplitude (or the amplitude for the free cantilever). Moreover a phase difference is introduced.

The problem can be modeled theoretically by treating the cantilever as a forced damped harmonic oscillator. (Fig. 4. 9.).

The Newtonian equation is, $F(z)+k(z_0-z)=m\frac{d^2z}{dt^2}+\frac{m\omega_0}{Q}\frac{dz}{dt}$ where z is the tip-surface distance, z_0 is the position of the cantilever at zero interaction, k is the force constant of the cantilever, Q is the quality factor of the cantilever and is related to the frictional forces acting on the tip or the width of the resonance peak. Hence depending on the forces acting on the cantilever, the characteristics of the cantilever will change. This will change the amplitude of oscillation of the cantilever and a phase difference will develop. These can be measured individually by feeding the signal to a lock-in amplifier to be compared with the signal used to drive the oscillation. The phase of the lock-in is chosen so that far away from the surface, the in-phase signal (A) or the amplitude is maximized while the out of phase component (B) is minimized. This problem has been solved by Salmeron et al[18] who obtained the following expressions for A and B.

$$A(z)=\frac{aQ}{(1-\delta+\delta^2Q^2)^{1/2}}\frac{1-\delta+\delta(\delta-f'(z))Q^2}{1-\delta+(\delta-f'(z))^2Q^2} \qquad (1)$$

$$B(z) = \frac{aQ}{\left(1-\delta+\delta^2Q^2\right)^{1/2}} \frac{f'(z)Q\sqrt{1-\delta}}{1-\delta+\left(\delta-f'(z)\right)^2Q^2} \qquad (2)$$

Here a is the amplitude of the applied oscillation of the tip out of contact , $\delta = 1-\frac{\omega^2}{\omega_o^2}$ where ω is the frequency at which the tip is driven and ω_o is the resonance frequency of the tip. $f'(z)$ is the derivative of the interaction force between the tip and the surface in units of the force constant of the tip, defined as,

$$f'(z) = \frac{1}{k}\frac{dF(z)}{dz} \qquad (3)$$

and is defined as positive for attractive interactions and negative for repulsive ones.

Let us call the derivative of the interaction force with distance as the stiffness of the junction (S), so that $S = \frac{dF(z)}{dz}$.

If we measure $A(z)$, at a frequency $\omega^2 << \omega_o^2$, so that $\delta \approx 1$. Then equation (1) becomes,

$$A(z) \approx \frac{a}{1+f'(z)} = \frac{ak}{S+k} \qquad (4)$$

Thus since $S = k(\frac{a}{A(z)} - 1)$ if we measure $A(z)$, we have determined S.

This expression is the same as that obtained by Pethica et al[19].

Now let us examine the quantity S. In non-contact S is related to the attractive Van Der Waals potential (Section 2.2.1), but is very difficult to model quantitatively as the tip is in contact with the surface for only a fraction of its period of oscillation. In order to get the elastic modulus of the sample, we analyze *S* when the tip is always in contact with the sample. Thus the amplitude of oscillation must be smaller than the mean deflection (load) of the tip, i.e.

$$a \leq \frac{W}{k} \qquad (5)$$

In the present experiment this occurs only at loads above ~300nN. At loads above ~300nN we can apply Hertzian contact mechanics (section 2.2.6.1) which gives us,

$$S \cong 1.8 E^{*2/3} W^{1/3} R^{1/3} \qquad (6)$$

where *W* is the external load applied, *R* is the radius of the tip and E^* is the modified elastic modulus of the junction defined as,

$$\frac{1}{E^*} = \frac{1-\nu_1^2}{E_1} + \frac{1-\nu_2^2}{E_2} \qquad (7)$$

where E_1 and E_2 are the elastic modulus of the polymer and tip respectively and ν_1 and ν_2 are the Poisson ratios of the polymer and tip respectively.

If we assume the tip to be composed of tungsten or tungsten oxide then $E_1 << E_2$. Thus we can approximate the above equation as,

$$\frac{1}{E^*} \approx \frac{1-\nu_1^2}{E_1} = \frac{1}{E_1^*} \qquad (8)$$

Thus if we measure *A* at a fixed load *W* with a tip of radius of curvature *R*, we can determine E_1^*. Since all the above polymers have Poisson ratios in a similar range[20], we are mainly measuring differences in E_1, the elastic modulus of the polymer. Also it should be noted from equation (6) that the effect of an error in the measurement of *R* does not have a very pronounced effect on the value of E^*. Another important point is that for a tip radius 1000nm, *S* is in the range 15-250 N/m for the polymers examined for loads ranging from 1-100nN, hence it is important to choose a tip with a large force constant *k*, so that the damping $\left(\frac{A}{a}\right)$ is not too significant and can be measured with a good signal to noise ratio.

4. 3. 5 Measurement of hardness: Hardness is measured by plastic deformation i.e. a deformation that does not recover on the time scale of the measurement. Here the tip was pushed into the surface with a large force (micronewtons for the radius used in the experiment). The tip was then removed and the surface was imaged in the topographic mode to observe any damage done to the surface. Typically the time elapsed between damaging and completing an image was on the order of a couple of minutes. We assume that the tip is not damaged during the measurement (since a tungsten tip is much harder than a polymer surface). The hardness is defined as the force required to produce an indent divided by the projected area of the indent in the plane of the surface.

4. 3. 6. Measurement of friction: Friction was measured by measuring the lateral deflection of the cantilever while moving laterally across the surface at a given load. This was done by scanning a single line around 200 nm in length and measuring the vertical and horizontal deflections of the cantilever as the voltage to the piezoelectric was increased linearly. (so that the sample was pushed into the tip). Moreover the tip was scanned from left to right and then

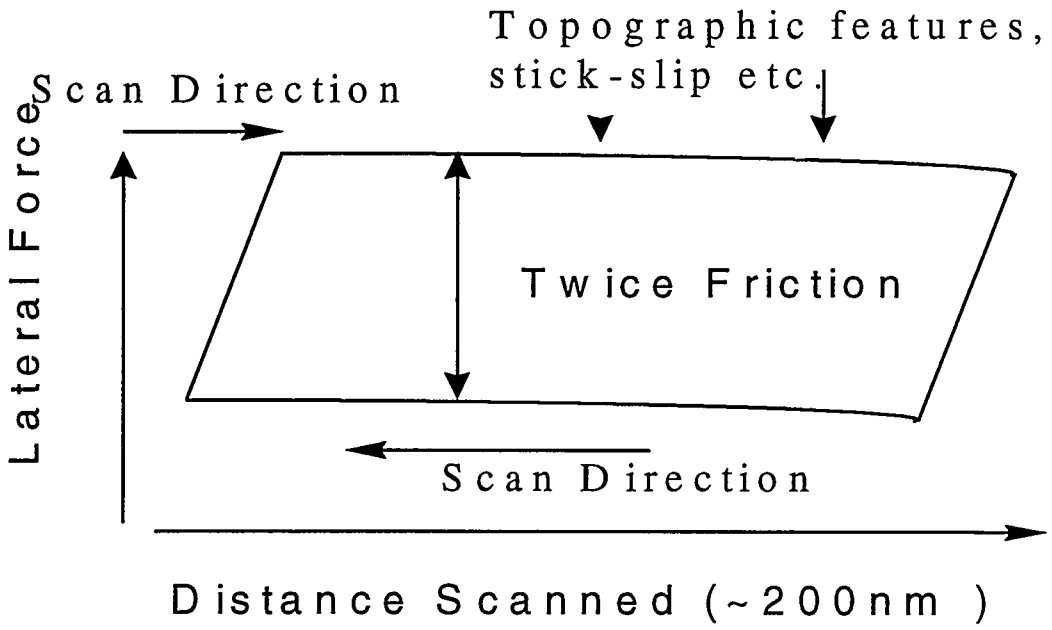

Fig. 4.10 A schematic diagram of a friction Loop

from right to left, generating a friction loop. The height of this loop represents twice the frictional force. The subtraction is performed as it is difficult to get the exact zero of the friction signal and to reduce the effect of topography by subtraction of signals, as can be seen in Fig. 4. 10

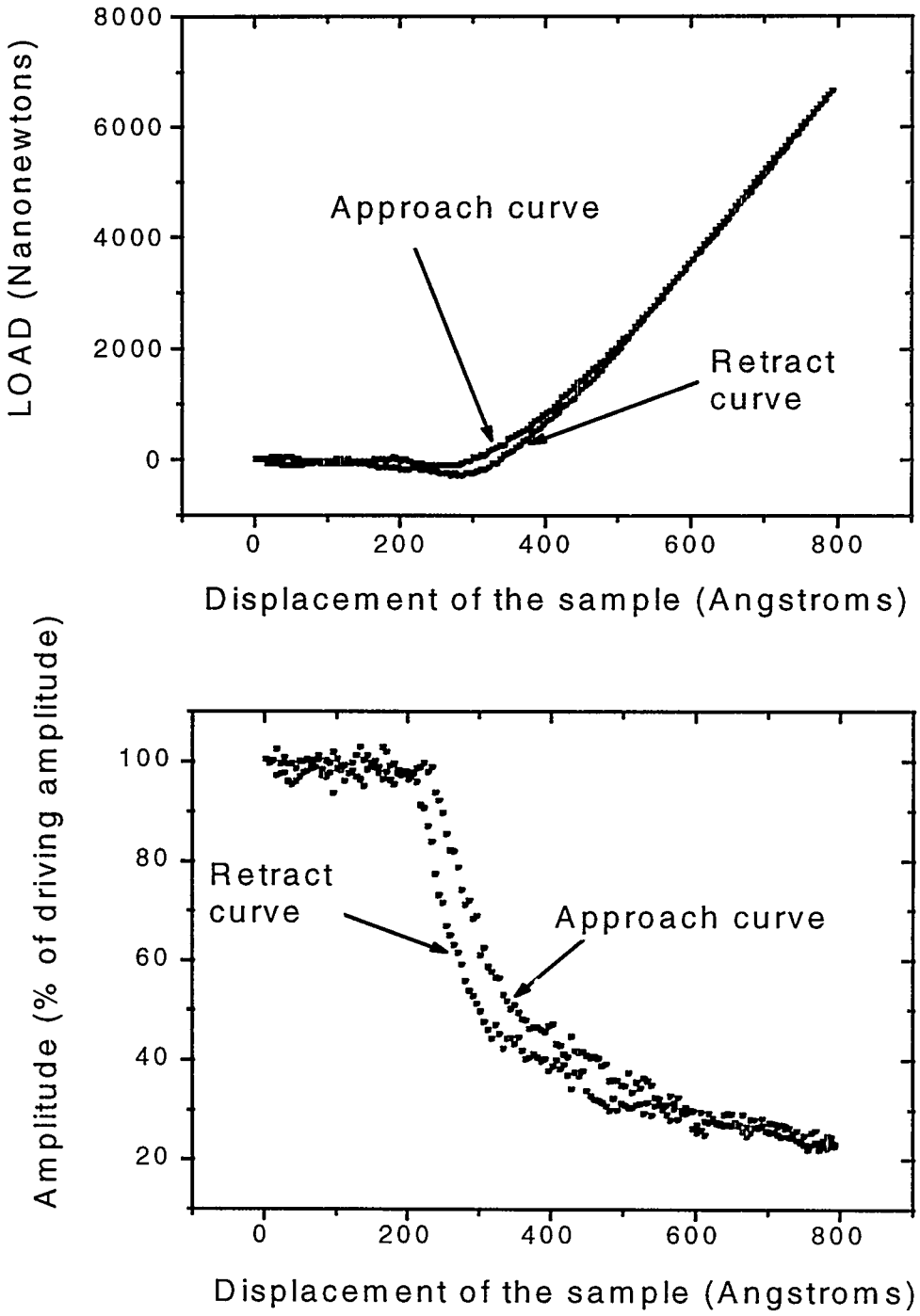

Fig. 4. 11 Force curves showing the deflection of the cantilever and the amplitude variation of an oscillating tip as the tip is pushed into the surface.

4.4. Results and Discussion:

4. 4. 1 Elastic Modulus: Shown in Fig. 4.11 are plots of Load W and amplitude damping $\left(\frac{A}{a}\right)$ in percentage vs sample displacement, obtained simultaneously on IPP , while approaching and retracting the sample and the tip. Initially the tip is

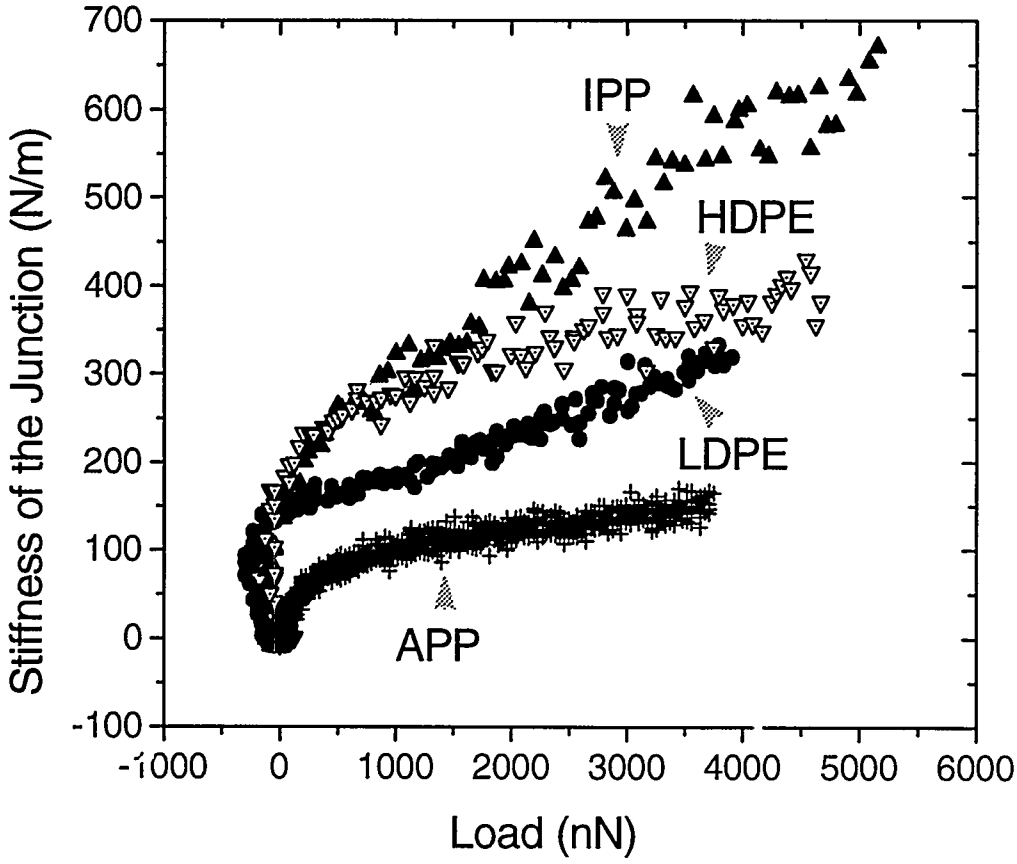

Figure 4.12 A plot of the Stiffness S , obtained from equation 4. vs the load W .

out of contact and the load and amplitude damping are unchanged. As the tip approaches the surface the amplitude gets damped.

There is further damping in repulsive contact of the tip and the surface, depicted by an increase in the load and a decrease in the amplitude. On retracting the tip a similar behavior is observed, there is however some hysteresis. This hysteresis is related to pull-off forces, piezo hysteresis and inelastic forces and is difficult to quantify. From approach curves like those in Fig. 4.11, we can plot the stiffness as a function of load using equation 4. (Fig. 4.12)

Moreover values for the elastic modulus from equation can be obtained using equation 6. We have assumed a Poisson ratio, (ν_1) of 0.34 for polyethylene and 0.32 for polypropylene[20] in the calculation. We have then plotted in Fig. 4.13, the elastic modulus Vs mean contact pressure (given by Hertzian contact mechanics equation 6) on sample approach, for loads when contact is maintained during the entire period of oscillation of the tip (i.e. the condition in equation (5)) i.e. above loads of ~300nN. Although the load regime analyzed (~300nN-5000nN) is similar for all the polymers, the contact pressure depends on the elastic modulus of the polymer and hence is different for different polymers,

In this repulsive load regime the Hertzian theory is a good approximation to study the effect of increasing load or pressure on the elastic modulus. The elastic modulus is seen to increase with mean contact pressure for all the polymers studied. To explain this we note that in the contact region, a large component of the pressure under the tip is hydrostatic. It is known that the elastic moduli of these polyolefins increases with hydrostatic pressure[20-23] The

increase in elastic modulus of the polymer with increasing pressure has been attributed to two effects:

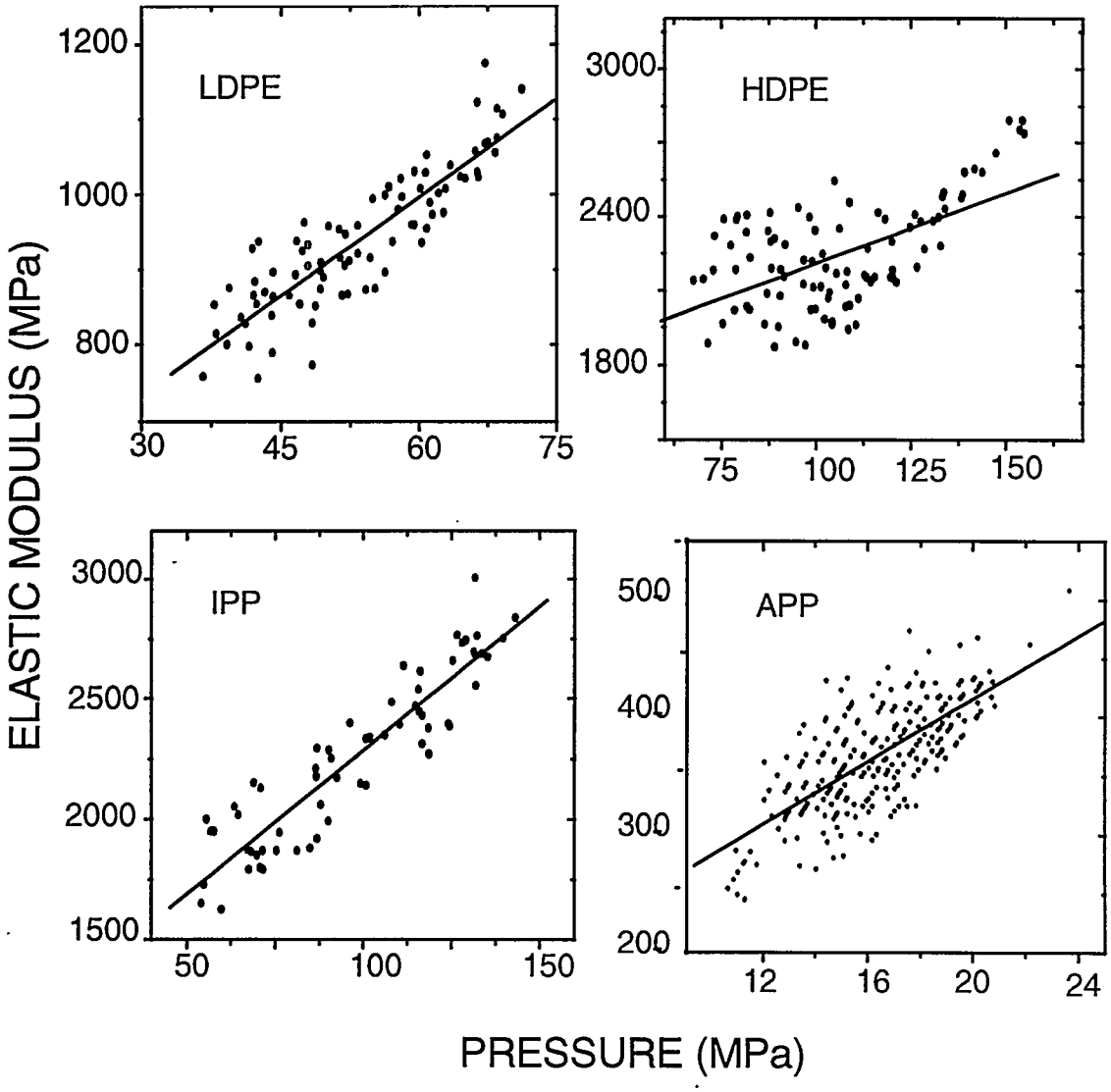

Figure 4. 13 Plots of elastic modulus vs contact Pressure plotted for LDPE, HDPE, IPP and APP.

a) An increase in the density of the polymer, which increases the interactions among polymer chains, thereby increasing the elastic modulus[23].

b) Changes in the relaxation dynamics of polymer chains which increase the elastic modulus[21]. The amorphous or disordered component of the polymer is more sensitive to these changes.

We find the relation of elastic modulus, (E) vs mean contact pressure (P) to agree with the expression observed in high pressure experiments[21.22], of the form,

$$E = E_0 + \beta P \qquad (9)$$

We have fit expressions of this form to the data and have obtained values for the

Polymer	E_0 (GPa)	β	Hardness (MPa)
LDPE	0.47	8.8	22
HDPE	1.6	5.7	60
IPP	1.09	11.9	125
APP	0.15	13.3	1.4

Table 4. 2. Average values of the extrapolated elastic modulus E_0, the constant β (obtained from line fits in Fig. 4.13, and hardness values $(\pm 25\%)$ measured on the polymers.

extrapolated elastic modulus at zero pressure, (E_0) and the constant of proportionality (β). These values are listed in Table 4. 2.

The constant β decreases with increasing density of the polymer. This is reasonable, since the effect of high pressure is to increase the density of the polymer[23] and thus a larger pressure effect is seen on a low density polymer like LDPE or IPP than on an already densely packed HDPE. The values of E_0 obtained from the curves fall into the range of elastic moduli expected on the

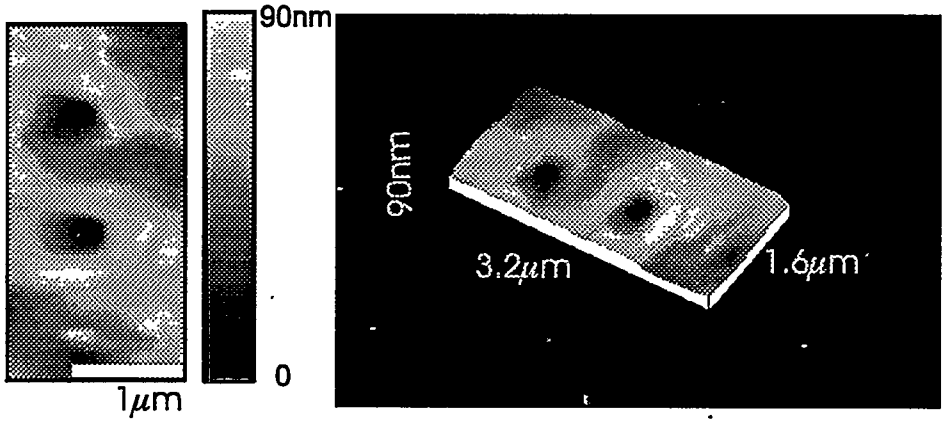

(a) (b)

Figure 4.14 Topographic images of indents formed on HDPE, after indenting with loads of 29 and 34 micronewtons. Microhardness values obtained from such measurements are listed in Table 4. 2.

polymers[24,25]. The expected trend of increasing elastic moduli with increasing

density and crystallinity is observed. It is known that HDPE has a higher elastic modulus than LDPE due to an increase in density and this is what we see. For the polypropylenes, an isotactic sample allows good packing of the chains which increases crystallinity substantially, this explains the higher values of elastic modulus of IPP as compared to APP.

4. 4. 2 Hardness: . The hardness values obtained by microindentation, Fig. 4.14 and defined as the load divided by the projected area of the indent are tabulated in Table(2). There is a considerable error bar on the hardness measurements, this is because the indent is not uniform and it is thus difficult to measure the area accurately. Moreover tip effects, i.e. the fact that we are imaging the indent with the same tip that was used for indentation results in imaging artifacts. The expected trend of increasing hardness with increasing crystallinity is observed and we can comment qualitatively on the relative yield strengths of the polymers. The hardness values compare well with literature values obtained by Vickers indentation[26,27] and no pressure effects could be observed.

4. 4. 3 Friction: In Figs. (4.15 and 4.16) we have plotted the frictional force vs load for the various polymers. The standard deviation is around 50nN. Since we have measured friction on all the polyolefins at the same speed and the same temperature, we do not expect the viscoelastic properties of the polymers to play a major role in determining the relative behavior of these very similar polyolefins. Any reasonable model for friction includes to first order four quantities,

1) The adhesion of the interface being sheared

2) The yield strength of the material

3) The elastic modulus of the material

4) The shear strength of the material

For LDPE, HDPE, IPP and APP it is known in the literature[8,10,28], and also from our own contact angle measurements that the critical surface tension, indicative of the surface energy or adhesion of the interface is similar. This is because these polyolefins are all composed of similar hydrophobic monomeric units of

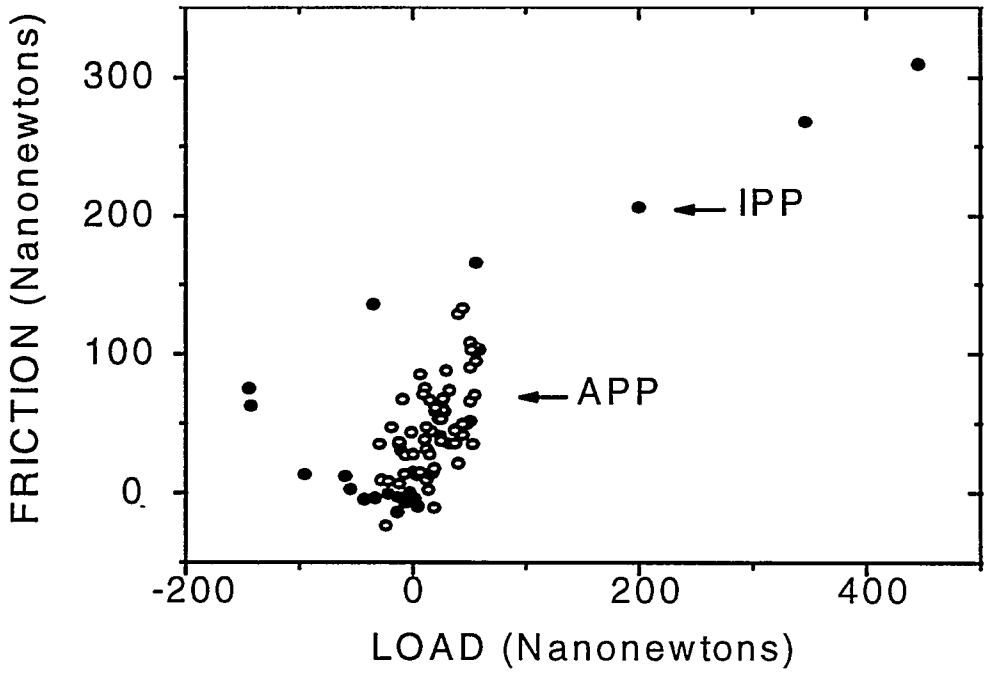

Figure 4.15 Friction vs Load curves for APP and IPP. The friction on APP is dominated by wear (plastic deformation), which yields a high friction coefficient.

carbon and hydrogen only. Thus we do not expect *adhesion* or *surface energy* of

the interface to influence the relative frictional behavior of LDPE, HDPE and IPP significantly.

The importance of the *yield strength* of the polymer in determining friction is seen by comparing friction Vs load curves for the chemically similar polypropylenes APP and IPP Fig. 4.15. APP is amorphous which results in a very low yield strength, as compared to IPP as can be seen in the low hardness value of APP as compared to IPP. We see a lot of jumps in the frictional force on APP, this is due to the fact that there is considerable wear of this sample even in the low load regime. A very high friction coefficient 0.75 is observed and this is due to wear of the sample. For IPP however we get uniform friction data and a much lower friction coefficient around 0.3. Because of sample wear it was not possible to measure the friction on APP reproducibly at high loads.

LDPE, HDPE and IPP have significantly higher yield strengths than APP (see hardness values). We could not resolve any wear of LDPE, HDPE and IPP in the range of loads over which friction was measured. It is true that we are using a tip with a large radius of curvature and are unable to resolve nanoscopic wear, however our friction data shows no jumps and is reproducible. Hence to a first approximation we are measuring frictional properties of these polyolefins in the *elastic regime* and the effect of *yield strength* on the frictional behavior of these polyolefins can be neglected. The *elastic modulus* and *shear strength* of LDPE, HDPE and IPP (or polymer deformation) control their relative frictional behavior in the load regime investigated. (0-2 micronewtons).

In the elastic regime, all models for friction assume that the frictional force

$$F = \tau A \qquad (10)$$

where τ is the shear strength of the material and A is the contact area.

There are many models which describe elastic contact of a single asperity (i.e. the tip) with a planar surface, we will invoke the JKR model (section 2.2.6.2). This we do because we see friction at negative loads that is predicted by the JKR model. Also we do get pull-off forces i.e. a finite force required to separate the tip and the surface, but they are not sharp (This is due to the large force constant or stiffness of the AFM tip). Moreover experiments done with the surface force apparatus (SFA) on polymers are in good agreement with the JKR model.[29]. Note that the contact pressure is considerably lower in the SFA where smooth surfaces are in contact with each other over large areas..

The JKR model expresses the contact area A between a single asperity and a surface as,

$$A = \left[\frac{3\pi^{3/2}R}{4E^*}.\left[W + 3\pi R\gamma + \sqrt{6\pi R\gamma W + (3\pi R\gamma)^2}\right]\right]^{2/3} \qquad (11)$$

Where E^* is the modified elastic modulus of the junction as defined above, γ is the surface energy per unit area (i.e. the work per unit area required to separate the surfaces from contact to infinity) , R is the radius of curvature of the tip and W is the load applied.

The JKR model suggests a finite contact area A_0 at zero load, which is given by,

$$A_0 = \pi \left(\frac{9\pi\gamma R^2}{2E^*} \right)^{2/3} \qquad (12)$$

The JKR model gives an expression for contact area, in our experiments we do not measure contact area but frictional force *(F)* which is a product of the contact area *(A)* and shear strength (τ). From equation (10) and (11) this is given by,

$$F = \tau A = \tau \left[\frac{3\pi^{3/2} R}{4E^*} \left(W + 3\pi R\gamma + \sqrt{6\pi R\gamma W + (3\pi R\gamma)^2} \right) \right]^{2/3} \qquad (13)$$

In Fig. 4.16 we have plotted the friction (*F*) Vs load (*W*) measured (in the elastic regime) on LDPE, HDPE and IPP. We have tried to fit equation (13) to the friction curves obtained experimentally, the curve fits are depicted by the dashed lines in Fig. 4.16. It can be seen from the Fig. that the frictional force *does not* exhibit the functional dependence on load as expected by equation (13) in the repulsive load regime. This does not mean that the JKR model is inapplicable, instead, the experimental data can be explained by noting that the shear strength of the polymer τ is not a constant, but increases linearly with pressure *P*. Many authors[9,22,30] have suggested an expression of the form,

$$\tau = \tau_0 + \alpha P \quad (14)$$

Thus the expression for frictional force in equation (13) must be modified in the repulsive load regime, to take into account the dependence of shear strength on the load or pressure (equation (14)). The modified expression for friction in this region is,

$$F = (\tau_0 + \alpha P)A = \tau_0 \left[\frac{3\pi^{3/2} R}{4E^*} \left(W + 3\pi R\gamma + \sqrt{6\pi R\gamma W + (3\pi R\gamma)^2} \right) \right]^{2/3} + \alpha W \qquad (15)$$

(Note: *PA=W*, e.g. the pressure multiplied by the contact area is the load, hence the second term that has a linear dependence on load)

And the frictional force at zero load, $F_0 = \pi \tau_0 \left(\frac{9\pi\gamma R^2}{2E^*} \right)^{2/3}$ (16)

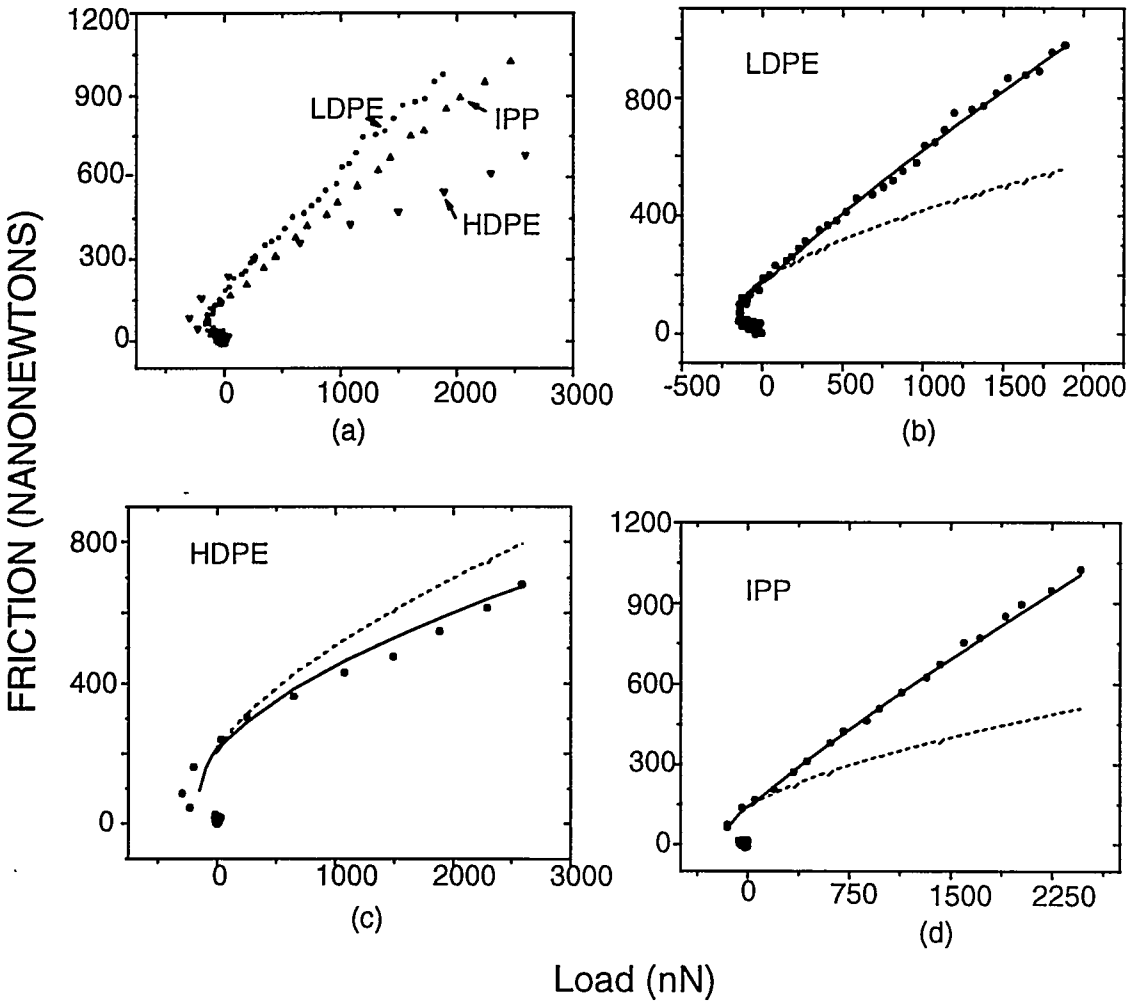

Figure 4. 16: Friction Vs Load Curves on LDPE, HDPE and IPP

This introduces another variable α, which is the pressure coefficient of the shear strength. This quantity is small and only becomes significant at high pressures, which is what we have under the AFM tip. The effect of α is to

introduce a linear behavior of the friction force Vs load in this high pressure regime where the second term in equation (15) becomes significant. The elastic modulus E^* (in equation (15)) also depends on pressure or load as measured above and a functional dependence of elastic modulus on load (equation (1) and (9)) must be introduced in equation (15) for an exact expression.

Thus the exact equation for friction (introducing the increase of elastic modulus with load), after taking into account pressure effects on the measurement is,

$$F = \tau_0 \left[\frac{3\pi^{3/2} R}{4(E_0^* + const * W^{1/3})} \left(W + 3\pi R\gamma + \sqrt{6\pi R\gamma W + (3\pi R\gamma)^2} \right) \right]^{2/3} + \alpha W \quad (17)$$

We have measured the dependence of elastic modulus on pressure, hence the unknowns in equation (17) are the shear strength at zero load τ_0 and the pressure coefficient of the shear strength α.

Equation (17) fits the experimental data very well, and we have obtained estimates for τ_0 and α. These values are listed in table (3) along with literature values for the same. The values seem to be of the right order of magnitude. Although there have been attempts to interpret the significance of τ_0 and α in microscopic terms using Eyring theory these parameters are best regarded as empirical constants[30]. The effect of high pressure on the shear strength of LDPE and IPP are similar. We could not observe any significant pressure effect on the shear strength of HDPE. To explain this we note that the density of both LDPE and IPP are lower than that of HDPE. The increase in density with increasing pressure follows the trend LDPE>IPP>HDPE[31] i.e. for the same

increase in pressure the increase in density is the smallest for HDPE (because it is already a

Polymer	τ_0 (Experiment)	τ_0 (Literature)	α (Experiment)	α (Literature)
IPP	9 MPa	5 MPa[9]	0.24	0.17[9]
HDPE	17MPa	(14-28) MPa[32] (2.5-14)MPa[9]	~0	(0.03-0.09)[32]
LDPE	6MPa	6 MPa [9]	0.3	0.14 [9]

Table 4.3. Values for τ_0, the shear strength of the polymer at zero load, and α for LDPE, HDPE and IPP. These values were obtained by fitting equation (17) to the experimental friction Vs Load curves. The fitting parameter γ =32mJ/m^2, was used for all the polymers. (This was a typical value seen from approach curves like those in Fig. 4. 11). The parameters used for the functional dependence of elastic modulus on pressure are those measured and listed in table (2). Literature values for τ_0 and α vary widely depending on strain rate and the type of experiment and it is difficult to compare numbers exactly, however the numbers obtained from the fit are of the right order of magnitude.

dense well packed polymer). This could be a reason why the value of α is the smallest for HDPE. However an exact interpretation of τ_0 and α needs a more detailed theoretical analysis and is not the focus of this paper. The small pressure effect of the shear strength in HDPE explains the low friction coefficient observed on the polymer.

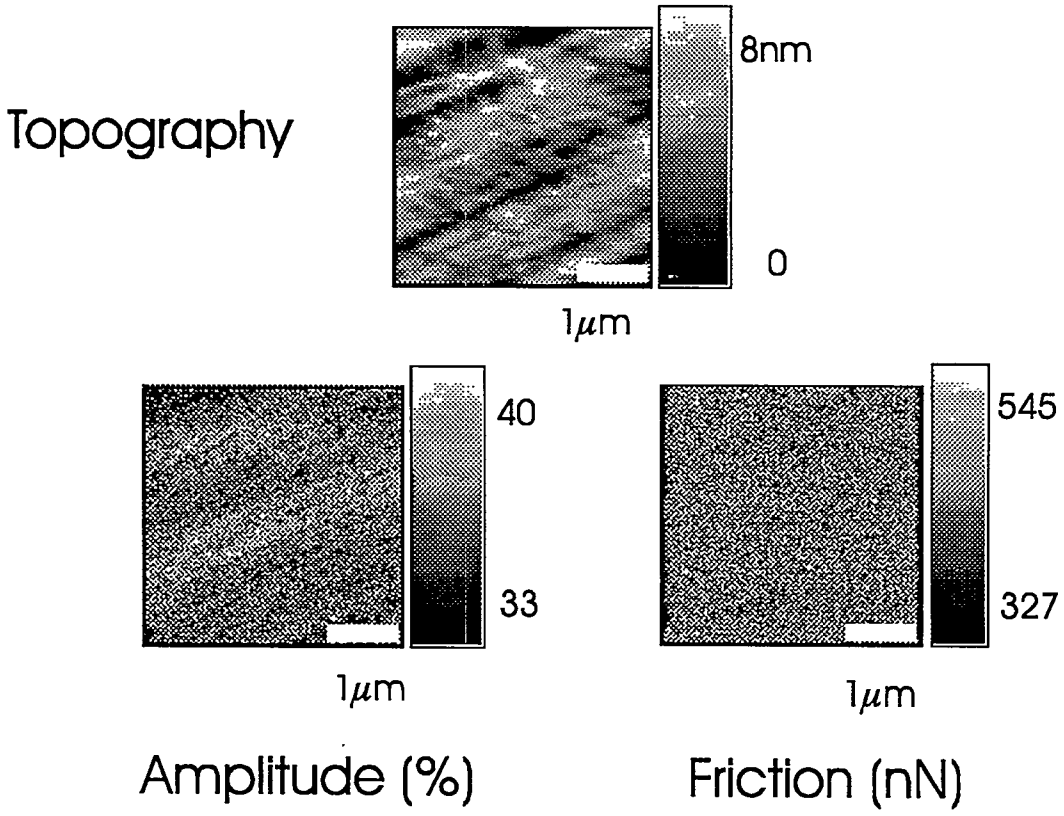

Figure 4. 17 Maps of topography, amplitude damping and friction obtained simultaneously on IPP at a load of 800nN.

4. 4. 3 Spatial variation of Elastic Modulus and Friction: In addition to measuring the elastic modulus and friction as a function of increasing load, we have spatially mapped out these quantities on the polymer surfaces. We obtain uniform maps (Fig. 4.17), and no significant spatial variation of these quantities is observed. This is because of the large radius of curvature of the CFM tip and hence the large contact area, which is larger than the characteristic size of the crystalline and amorphous domains. This results in an average value for these quantities over the domains. This is a limitation of the CFM and we would have to use sharper tips or AFM to map out these quantities with nanoscale spatial resolution, (at higher contact pressures) which has been successfully carried out in various other studies[30-32]

4. 4. 4. Correlation with surface vibrational spectra obtained by SFG. Zhang et al[33] have measured the SFG spectra of the same samples APP and IPP and LDPE and an Ultra High Molecular Weight PolyEthylene (UHMWPE). The SFG spectra reveal enhanced order at the surface in the more crystalline UHMWPE, HDPE and IPP as compared to APP and LDPE. In our SFM measurements we observe that the HDPE and IPP samples are considerably harder and have higher elastic moduli (Table 4. 2) than LDPE and APP which correlates well with the higher order seen on these surfaces. This implies that the increased packing or ordering at the surface is responsible for the higher modulus and hardness (or better mechanical properties).

4. 5 Conclusions: In this chapter, the effects of high pressure under the SFM tip were demonstrated. A new modification to SFM, using tips of large radii, to map spatially averaged properties, at low contact pressures and high surface sensitivities was implemented. Quantitative values were obtained for surface moduli, hardness and friction of LDPE, HDPE, IPP and APP. Finally trends observed in the mechanical properties were compared to SFG spectra. The correlation observed between SFM and SFG measurements prompted future studies wherein both techniques were used again on the same samples to study surface structural and mechanical properties, which will be described in the following chapters.

Chapter 4. References:

[1] R. Overney and E. Meyer, MRS Bulletin **18,** 5, 26 (1993)

[2] J. P. Aime, Z. Eikaakour, C. Odin, T. Bouhacina, D. Michel, J. Curely and A. Dautant, Journal of Applied Physics **76**, 2, 1754 (1994)

[3] C. M. Mate, IBM Journal of Research and Development **39,** 6, 617 (1995)

[4] S. J. O'Shea, M. E. Welland and J. B. Pethica, Chemical Physics Letters **223,** 336 (1994)

[5] M. Heuberger, G. Dietler and L. Schlapbach, Nanotechnology **5**, 12 (1994)

[6] H. Hertz, J. Reine Angew. Math. **92**, 156 (1881)

[7] D. P. Woodruff and T. A. Delchar, *Modern Techniques of Surface Science, 1st ed.* (Cambridge University Press, New York, 96, 1989)

[8] H. W. Fox and A. W. Zisman, J. Colloid Science **7**, 428 (1952)

.[9] B. J. Briscoe and D. Tabor, Journal of adhesion **9**, 145 (1978)

[10] S. Wu, *Polymer interface and adhesion* (Marcel Dekker, New York, 184, 1982)

[11] F. W. Billmeyer, *Textbook of Polymer Science, 3rd ed.* (Wiley-Interscience, New York, 242, 1984)

[12] L. Mandelkern and R. G. Alamo In *Physical Properties of Polymer Handbook,* Mark, J.E., Ed.; (American Institute of Physics, New York, 123, 1996)

[13] J. M. G. Cowie, *Polymers: Chemistry and Physics of Modern Materials* (Intext Educational Publishers, New York, 1973, ch. 10)

[14] D. Rugar, H. J. Mamin and P. Guethner, Applied Physics Letters **55**, 25, 2588 (1989)

[15] M. Kutz ed, *Mechanical engineers' handbook 2nd ed.* (Wiley, New York, 1998)

[16] M. B. Bever ed., *Encyclopedia of Materials Science and Engineering* (Pergammon Press, Oxford, 1986)

[17] S. Sheiko, M. Moller, E. M. Reuvekamp and H. W. Zandbergen, Phys.Rev. B **48**, 5675 (1993).

[18] M. Salmeron, MRS Bulletin **18**, 5, 20-25 (1993).

[19] J. B. Pethica and W.C. Oliver, Physica Scripta T **19A**, 61-66 (1987)

[20] K.D. Pae, J. A. Sauer In *Engineering Solids under Pressure,* .Pugh, H. D., Ed.; (The Institution of Mechanical Engineers: London, 1971; p 69-74)

[21] S. V. Radcliffe, In *Deformation and Fracture of Polymers*, H. H. Kausch, J. A. Hassell and R. I Jaffee, Eds.; (Plenum Press: New York, 1973; p 198).

[22] L. C. Towle, J. Appl .Phy. **43**, 4 ,1611 (1973)

[23] J. Sayre, S. Swanson and R. Boyd, Journal of Polymer Science, Polymer Physics edition **16**, 1739 (1978)

[24] R. Popli and L. Mandelkern, Journal of Polymer Science, Polymer Physics **25**, 441 (1987)

[25] R. P. Quirk and M. A. Alsamarraie, In *Polymer Handbook,* 3rd ed.; J. Bandrup, and H. Immergut, Eds.; Wiley: NewYork, 1989; Ch. 5, p 23, 31.

[26] J. M. Salazar and F. J. Balta Calleja, Journal of Materials Science **18**, 1077 (1983)

[27] V. Lorenzo, J. M. Perena, and J. G. Fatou, Journal of Materials science letters **8**, 1455 (1989)

[28] C. M. Pooley and D. Tabor, Proc. R. Soc. Lond. A **329**, 251 (1972)

[29] V. S. Mangipudi, E. Huang, and M. Tirrell, Macromol. Symp. **102**, 131 (1996)

[30] D. Briggs, D. Rance, In *Comprehensive polymer science,*1st ed.; C. Booth, and C. Price, Eds.; (Pergammon Press, 1989; Vol. 2, p 726-728)

[31] B. G. Bogdanov and M. Michailov, In *Handbook of Polyolefins* C. Vasile, and R. Seymour Eds. (Marcel Dekker: New York, 1993; p 298-299).

[32] B. J. Briscoe and D. Tabor Wear **34**, 29 (1975)

[33] D. Zhang, Y. R. Shen and G. A. Somorjai, Chemical Physics Letters **281**, 394 (1997)

5. Modification of surface chemical and mechanical properties of Low Density Polyethylene (LDPE) by the presence of bulk additives. A combined SFG and SFM study

5. 1 Introduction: Bulk additives[1] are added to polymers during processing to preserve, enhance and / or alter various surface and bulk properties of the polymers. Some examples of additives are: *Antioxidants* (e.g. sterically hindered phenols and aromatic amines), which assure protection against thermal and oxidative degradation during processing and / or environmental exposure under working conditions; *Antistatic agents*, used to reduce static electricity; *Photostabilizers*, which are chemical compounds which inhibit light induced degradation (e.g. hydoxybenzophenones); *Lubricants* (alcohols, esters); *Plasticizers*; *Crosslinking agents* etc. Some of these additives are molecules which have low surface energy which segregate to the polymer surface. The purpose of this study[2] was to use a combination of the extremely surface sensitive techniques namely SFG and SFM to study the changes in surface properties, (namely the chemistry of the surface and the modulus and the friction) caused by the presence of these additives.

5. 2 Experiments:

5. 2. 1 Sample Preparation: Pure low density polyethylene was purchased in the form of pellets from Aldrich. (Catalog No. 42,802-7). The polymer was melted between two Pyrex glass plates under a load of 10 kgs and cooled slowly. The

polymer was then peeled off. In this way smooth polymer surfaces are obtained as the polymer in contact with the glass surface takes the shape of the surface. The commercial LDPE used was in the form of a commercial film ~ 50 microns in thickness, obtained from Union Carbide (GRSN-7047 NT7). The molecular weight, crystallinity and chemical structure of the bulk of the two polymers are similar. The density is 0.92g/c.c., and the percentage crystallinity is ~ 25%. The commercial film is known to contain additives like those mentioned in the preceding section. The exact chemical nature of the additives however was not known as it was considered proprietary.

5. 2. 2. SFG: The SFG set up has been described in detail in Chapter 3.

5. 2. 3. SFM: The SFM used is described in chapter 4. Stiffness and friction were measured as a function of load as described in Sections 4.3.4, 4.3.6 and 4.4.1.

5. 2. 4. Raman Spectroscopy: To establish a comparison with other spectroscopic techniques, low density polyethylene (LDPE) and commercial low density polyethylene (CLDPE) were first characterized by Raman spectroscopy in the frequency region of 2700 cm^{-1} to 3100 cm^{-1}. This region is the frequency regime for the vibrational modes of C-H bonds, which form the backbone of polyethylene. The Raman spectra were obtained on a Labram Raman spectrometer.

5. 3 Results and Discussion:

5.3.1 Raman spectroscopy: The Raman spectra are identical for these two polymers and consist of peaks at 2849 cm^{-1} and 2883 cm^{-1} which correspond to symmetric and asymmetric (C-H) vibrational modes, respectively (Fig. 5.1).

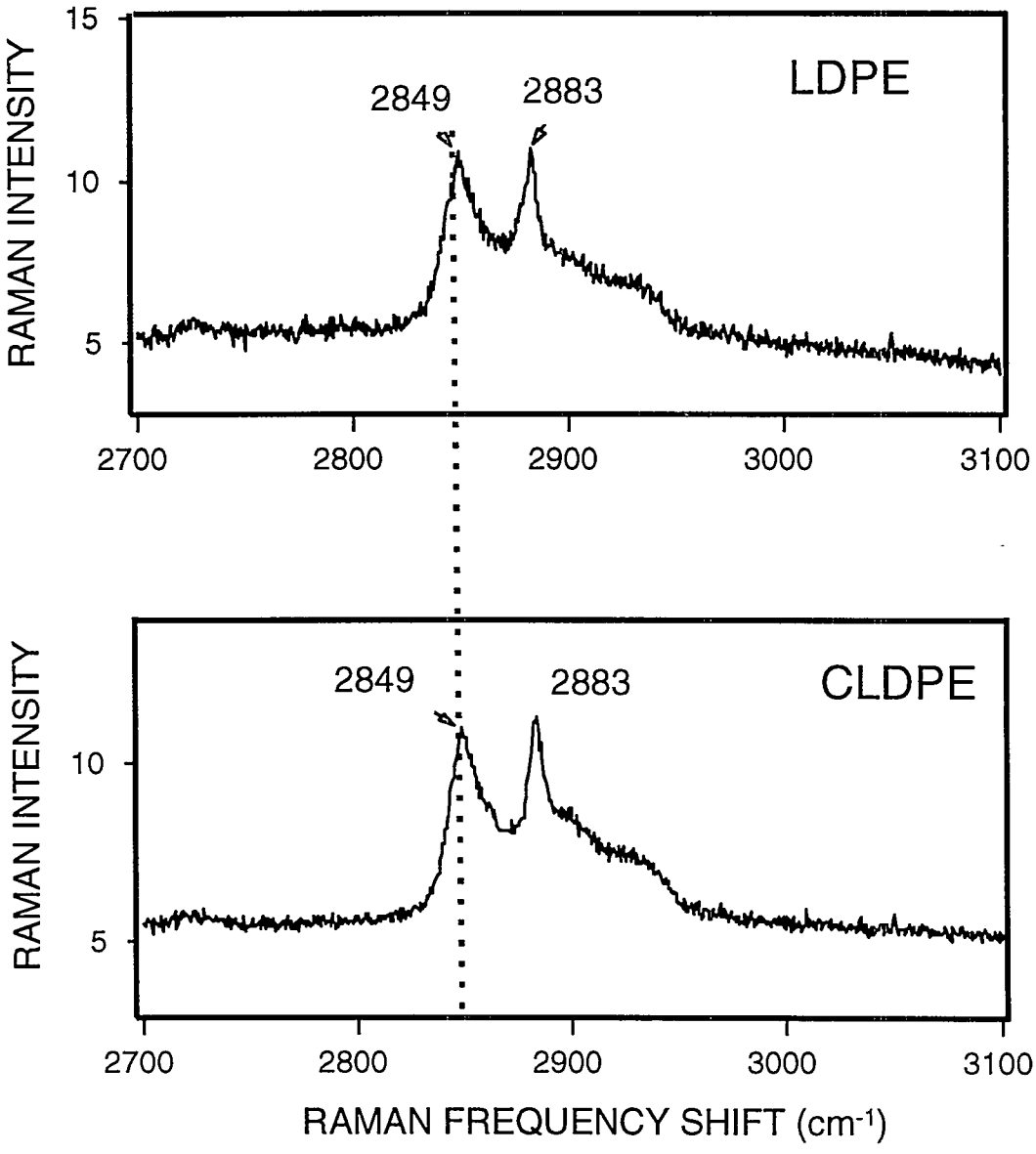

Figure 5.1 Raman spectra of LDPE and CLDPE.

These Raman spectra are consistent with the published results for polyethylene and indicate that we have typical polyethylene samples.[3] It also indicates that the bulk structure of the two samples LDPE and CLDPE are similar.

5. 3. 2 SFG: The SFG surface vibrational spectra of LDPE and CLDPE are displayed in Fig. 5.2. In contrast to the identical Raman spectra of the two polymers, the SF spectra of these two polymers are clearly very different. For LDPE (Fig. 5.2a), the band at 2851cm^{-1} correlates well with the CH_2 symmetric stretch and the band at 2926cm^{-1} can be assigned to the asymmetric stretch, which is similar to the Raman spectrum of LDPE. However for CLDPE, the surface vibrational spectrum (Fig. 5.2 b) is different from that of LDPE and is also different from its Raman spectrum. The most striking feature is the disappearance of the typical CH_2 vibrational peaks (present in the Raman spectrum) and the dominance of a peak at 2822cm^{-1} which is characteristic of the C-H symmetric stretch of methoxy groups (-OCH_3). These groups are attributed to antioxidants or stabilizers that are added to commercial polyethylene. These additives act as radical scavengers and do contain chromophores like the methoxy group.[4] Comparing SFG and Raman spectra, we can infer that the surface chemistry of the polymers is different for LDPE and CLDPE, which was readily differentiated by surface-specific SFG. Our data indicate that the surface chemistry of LDPE is same as bulk polyethylene while the surface of CLDPE is fully covered by additives which totally smear out the characteristic peaks of polyethylene which is present in its bulk as indicated by the Raman spectrum.

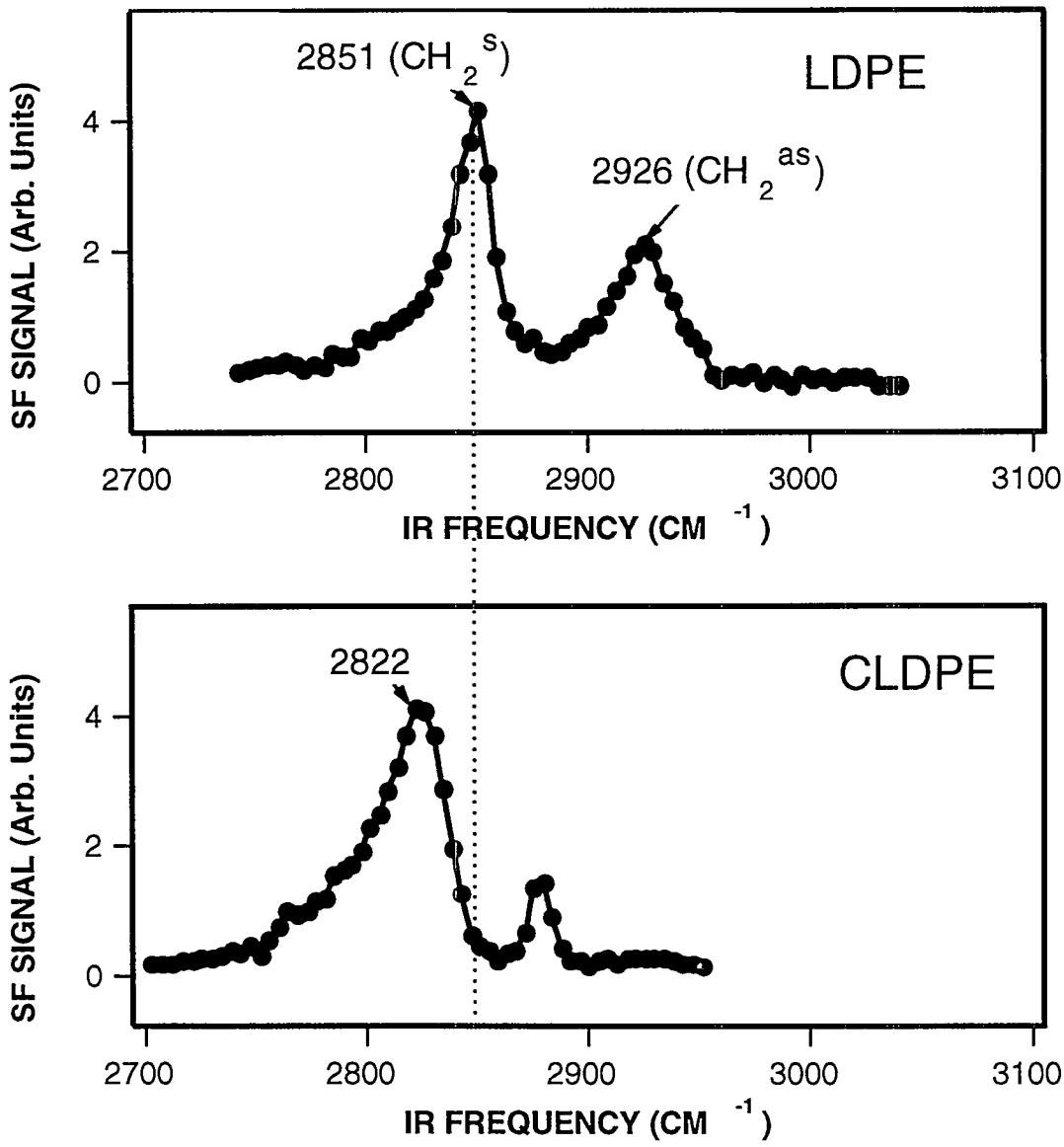

Figure 5.2 SFG spectra of LDPE and CLDPE.

5. 3. 3 Stiffness: Fig. 5. 3. (b) shows a plot of the stiffness S, of the two polymers Vs Load. For LDPE there is an attractive force between the tip and the surface, on approach, which results in negative loads, i.e. the tip is pulled towards the surface. Because of the high force constant of the cantilever

(235N/m) we do not see a jump into contact, but a gradual attraction of the cantilever towards the surface. This results in two different values of stiffness at some negative loads, one when the tip is being pulled toward the surface and the other when the tip is being pushed away from the surface. In the positive load regime the stiffness of both polymers increases with load, as expected. The exact relationship between the stiffness and the load depends on the nature of the contact between the tip and the surface. In the present case we have measured the shape of the tip, by scanning a surface of strontium titanate and found it to be approximately spherical. Hence we can apply Hertzian[5] contact mechanics in the repulsive load regime, and expect a relation of the form, $S \approx 1.8 W^{1/3} R^{1/3} E^{*2/3}$, where W is the load, R is the radius of curvature of the tip and E^* is the modified elastic modulus of the junction. For a contact between a high elastic modulus material (tungsten tip) and a low elastic modulus material (the polymer), E^* can be approximated as, $E^* \approx \frac{E}{(1-\nu^2)}$. Here E is the elastic modulus and ν is the Poisson ratio of the polymer. Any difference in the stiffness measured on different surfaces, at the same load with a tip of the same radius of curvature, is indicative of a different elastic modulus of the surface region being probed.

The stiffness Vs load curves may be distorted by piezoelectric creep and nonlinearities. We have measured the response of the piezoelectric scanner, (i.e. the motion of the scanner in the z-direction Vs voltage) by interferometry. This is done by impinging the fiber optic carrying light directly on a reflective

sample, which is then moved in the z-direction. The interference signal shows minimal non-linearities for small voltages applied to the tube. In our present experiment the stiffness Vs load curves were obtained by applying similar small voltages to the piezoelectric tube and thus we do not expect any significant distortions of the curves due to non-linearities of the piezoelectric scanner. As can be seen the stiffness of the commercial sample is much lower at loads below 1 micronewton. This is because of the different surface chemistry on CLDPE as seen by SFG i.e. the presence of the additives on the surface of the commercial sample. Since the CLDPE surface has a low stiffness indicative of a low elastic modulus in this load regime, we can infer that the additive layer on the surface has a lower elastic modulus than the bulk polymer. At loads above 1 micronewton the effect of the additives is not seen and the two surfaces have the same elastic properties.

5. 3. 4 Friction: Friction vs load curves measured on LDPE and CLDPE are plotted in figure 5. 4 (a) We do see friction at negative loads on the pure LDPE while we cannot resolve any such behavior on the commercial sample. This implies that the adhesion or the surface energy of the surface of the commercial sample is negligible. Now it is known that additives migrate from the bulk polymer to the surface. The driving force for this migration is the lower surface energy of the additives as compared to the pure polymer, hence it is reasonable that we see no significant adhesion (i.e. a low surface energy) on the

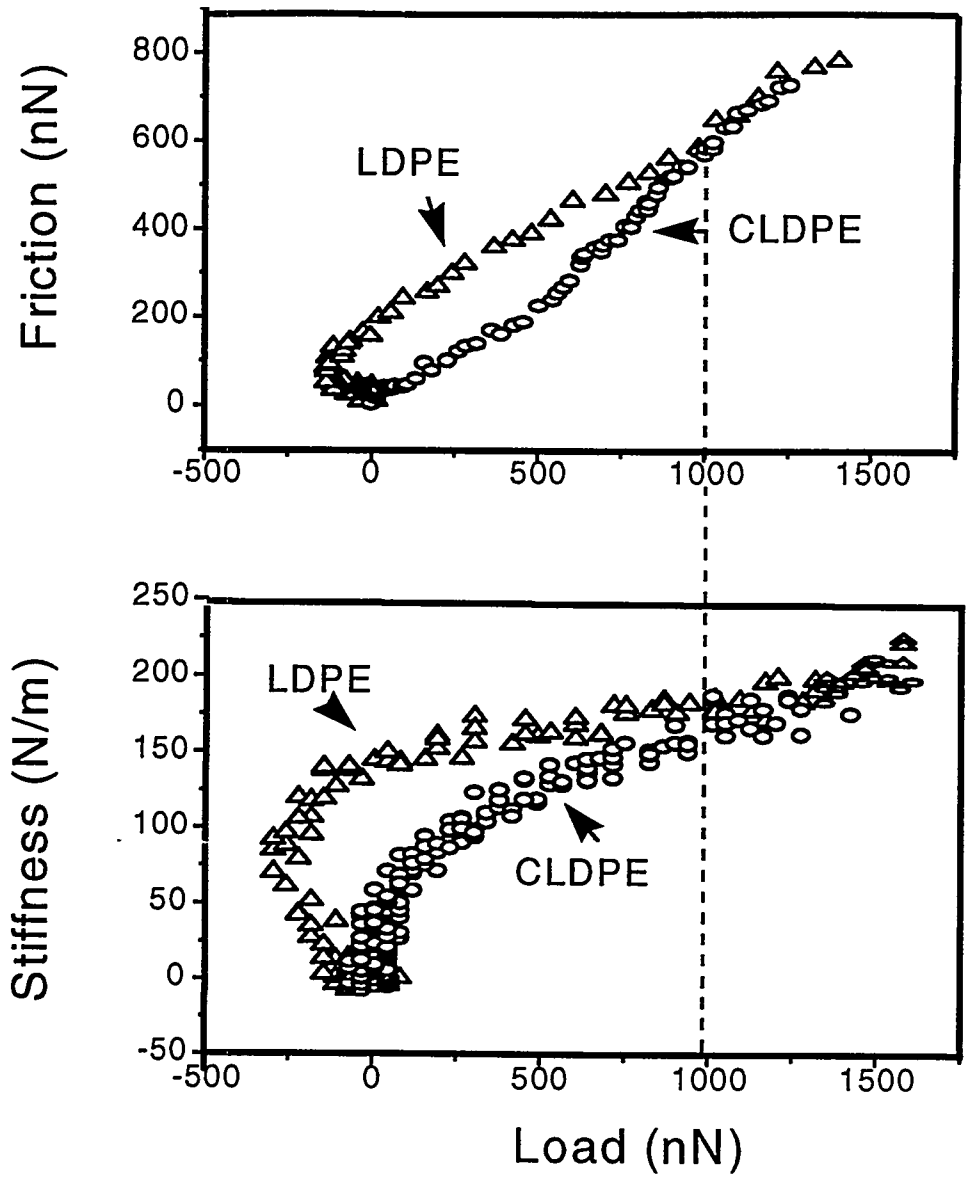

Fig 5.3.a shows the frictional force measured on the polymers Vs Load.

b. Stiffness Vs Load measured on LDPE and CLDPE

sample. To explain the nature of the friction Vs load curves we must recall that the frictional force (F_{Total}) on polymers consists of two components, an adhesive component (F_{ad}) and a deformation component (F_{def}). In fact several authors[6] have proposed a relation , $F_{Total} = F_{ad} + F_{def}$

The frictional force for CLDPE (Fig. 5.4) is lower than LDPE at loads below 1 micronewton. This can be explained by the low surface energy of the additive layer, which decreases the contact area between the tip and the surface[5]. This results in a lower adhesive component of the friction on CLDPE as compared to LDPE, thereby decreasing the frictional force measured on CLDPE.

However, at loads below 1 micronewton the slope of the friction Vs load curves (or the friction coefficient) of CLDPE is higher than that of LDPE. This can be explained by the deformation component of the friction. As measured, the elastic modulus of CLDPE is lower than that of LDPE in this load regime. Thus as the load is increased, the elastic deformation or the contact area between the tip and the surface increases more rapidly for CLDPE than for LDPE.[5] This increases the deformation component of the friction for CLDPE more rapidly than that for LDPE, and hence the slope of the friction Vs load curve (i.e. the friction coefficient) is greater for CLDPE as compared to LDPE. Although we have not resolved any wear on CLDPE during our measurements, inelastic deformations of the weaker additive layer cannot be ruled out. Any inelastic deformations of CLDPE would also contribute to an increase the slope of the friction Vs load curve (the friction coefficient).

Thus it is important to differentiate between the adhesive and deformation component of friction, and a polymer exhibiting a lower friction need not show a lower friction coefficient.

Above 1 micronewton the two curves merge together, indicating that the same sub surface structure of the two polymers controls the frictional properties in this load regime. It should be noted that this is the same load above which no effect of the additives could be seen on the stiffness of the polymer surface. We have measured the radius of the tip accurately as 1 micron, thus using Hertzian contact mechanics, the mean contact pressure at which the additive layer no longer influences the measurement can be estimated as 60MPa. Also the elastic penetration depth till which the additives influence the elastic response and friction of the commercial sample is estimated as 8nm. Thus we must have a very thin additive layer covering the surface, this is consistent with the fact that the additives were not detected in Raman spectroscopy but were observed in the SFG spectrum. Since the effect of the additives is not seen above penetration depths of 8nm, we can assume that at these depths we are deforming mostly the bulk polymer, and thus the additive layer on the surface must be less than 8nm in thickness. This provides an upper limit on the surface sensitivity of SFG on polymer surfaces.

5. 4 Conclusions: In this chapter we have seen how a combination of SFG and SFM provides valuable information about the chemical and mechanical properties of surfaces. We have observed that It is possible to completely modify the surface properties of a polymer by adding small molecules (low surface energy) while processing. In this way the bulk properties of the polymer can be preserved while the surface properties may be modified. We have demonstrated

that different spatial regions of the polymer surface are responsible for the mechanical properties measured in different load regimes. This is why the presence of a small quantity of additives drastically altered the surface structure of the polymer and hence its mechanical properties only at penetration depths below around 8nm. Finally we have obtained an upper limit on the surface sensitivity of SFG on polymers.

In the proceeding chapters we will further exploit the combination of SFG and SFM.

Chapter 5. References:

[1] C. Vasile, *Additives for Polyolefins: General Outlook* in Handbook of Polyolefins, edited by C. Vasile and R. Seymour (Marcel Dekker, New York, 1983)

[2] D. H. Gracias, D. Zhang, Y. R. Shen and G. A. Somorjai, Tribology Letters **4**, 231 (1998)

[3] P. A. Bentley and P. J. Hendra, Spectrochimica Acta Part A **51**, 2125 (1995)

[4] N. B. Colthup and L. H. Daly, *Introduction to Infrared and Raman Spectroscopy* (Academic Press Inc.: New York, 1994).

[5] K. L. Johnson, *Contact Mechanics* (Cambridge University Press,1985).

[6] F. P. Bowden and D. Tabor, *The friction and lubrication of solids* (Oxford, Clarendon Press, 1964) v2, ch 14.

6. Fabrication of a High Vacuum SFM to measure temperature dependent changes through the glass transition of polypropylene surfaces.

6. 1 Introduction: In the previous chapters, the viability of SFM as a probe to study mechanical changes occurring at the surface of a polymer has been demonstrated.

Now, a dramatic change is known to occur in polymers as they undergo the glass transition[1]. The glass transition temperature depends on the type of polymer, the values for most polymers lie in the range (-150 ^{0}C to 200 ^{0}C). The *bulk* mechanical modulus of the polymer is known to increase by orders of magnitude below its glass transition. In order to study the changes in the *surface* mechanical properties, it was necessary to build a variable temperature SFM. The polymer of focus was polypropylene. The glass transition of polypropylene[2] occurs in the temperature range of 0 ^{0}C to -20 ^{0}C. To avoid cooling the entire SFM, (while cooling the sample) it is necessary to use an SFM which is designed in such a way to minimize conduction of heat from the cold region of the sample to the rest of the instrument. It was thus necessary to use a high vacuum instrument. A high vacuum instrument also precludes the possibility of water vapor or other gases from condensing on the cold sample. In this chapter the design and fabrication of the high vacuum SFM will be described.

6. 2 Overview of Instrument: Shown in Fig. 6.1 is the schematic diagram of the instrument. The instrument was built in one year at a cost of around $ 50000.

6. 2. 1 Vacuum characteristics: The SFM head is housed in a glass bell jar, which sits on a metal base (feedthrough collar) which contains various ports required for vacuum operation. The vacuum seal between the bell jar and the metal base was made with a viton O-ring and grease. The chamber is pumped using a turbo-molecular pump, which is backed by a mechanical rotary pump. During scanning (actual imaging with the SFM) these pumps are turned off and the pressure is held by sorption pumps filled with molecular sieve and immersed

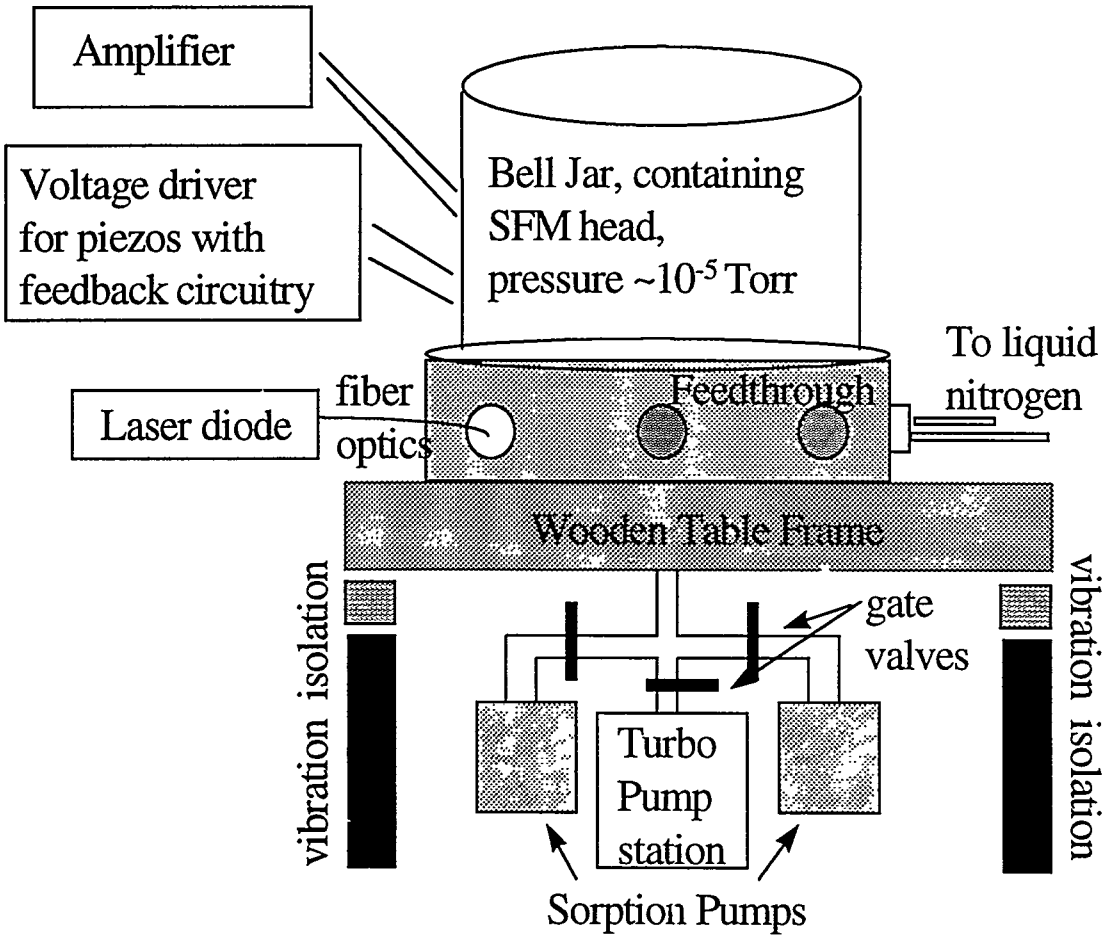

Figure 6. 1 A schematic diagram of the high vacuum SFM

in liquid nitrogen. Sorption pumps are quiet as compared to the much more noisy turbo and mechanical pumps and thus facilitate stable operation. The typical pressures achieved by this pumping scheme is ~10^{-5} Torr. Since typical kinetic mean free paths of molecules[3] are 10^{-5} cms at 760 Torr, we can reduce conduction through the gas phase drastically, by increasing the mean free path of the molecules to ~100 cms at 10^{-5} Torr, which is several times the dimension of the chamber. Also at such pressures, lower than the vapor pressure of water, condensation is precluded. The pressure is measured by a thermocouple gauge in the range of 760 Torr to 20 milli Torr and an ionization gauge in the pressure range < 10^{-4} Torr. These gauges are attached to feedthrough ports on the metal base.

6. 2. 2 Mechanical Vibration Isolation: Every object has a mechanical vibrational frequency (resonance frequency). The resonance frequency depends on the dimensions and elastic properties of the object. The greater the mass of the object the lower is its resonance frequency. The amplitude of oscillation of the body vs. frequency is shown in Fig. 6. 2. As can be seen from the Fig. the amplitude of oscillation of the object is greatly damped above its resonance frequency. To reduce the effect of building vibrations (typically in the range of 2-20 Hz) the entire SFM was seated on a wooden frame which was floated using vibration isolation legs which have very low resonance frequencies. The wooden frame was used because wood (because of its fibrous structure) damps oscillations more effectively than steel or aluminum. Also the SFM was seated

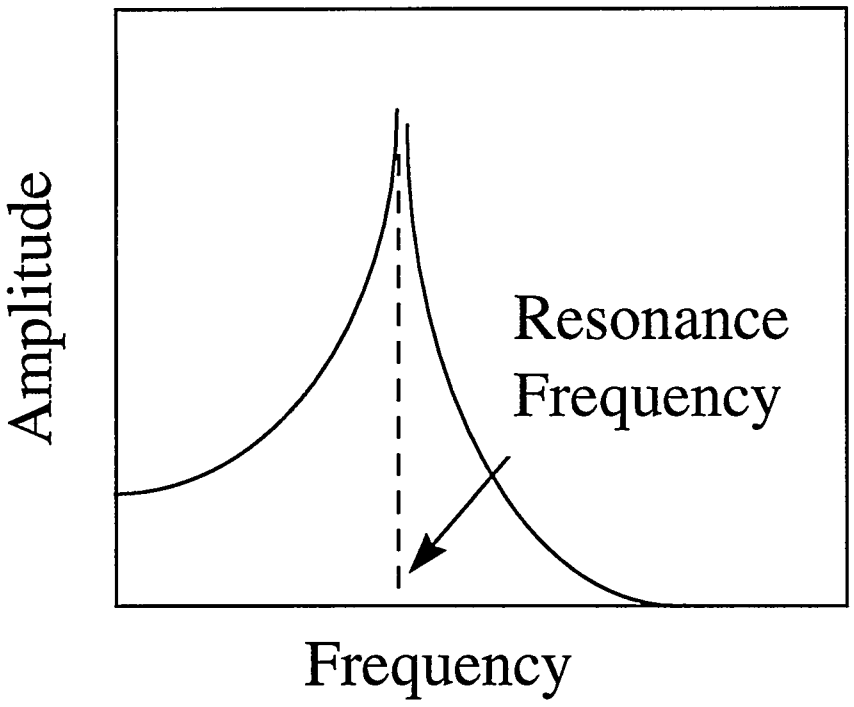

Figure 6. 2 A typical frequency response of a mechanical oscillation.

asymmetrically on the table top to damp symmetric oscillation modes of the table top. The second stage of mechanical vibrational isolation was affected by suspending the plate on which the SFM head inside the bell jar rested by three weak springs, which were chosen to have extensions of around 1.5 inches. This plate was weighted down. Thus by increasing the mass and decreasing the strength of the springs, low resonance frequencies could be enforced on the instrument. The springs were wrapped with loose viton tubing to damp the low frequency oscillations of the springs. These springs can be seen in Fig. 6.3. and are labeled (b) in Fig. 6.4

6. 2. 3 The SFM head: The SFM head is based on the walker style STM of *Frohn et al* [4] and is shown in Fig. 6.3 and Fig. 6.4.

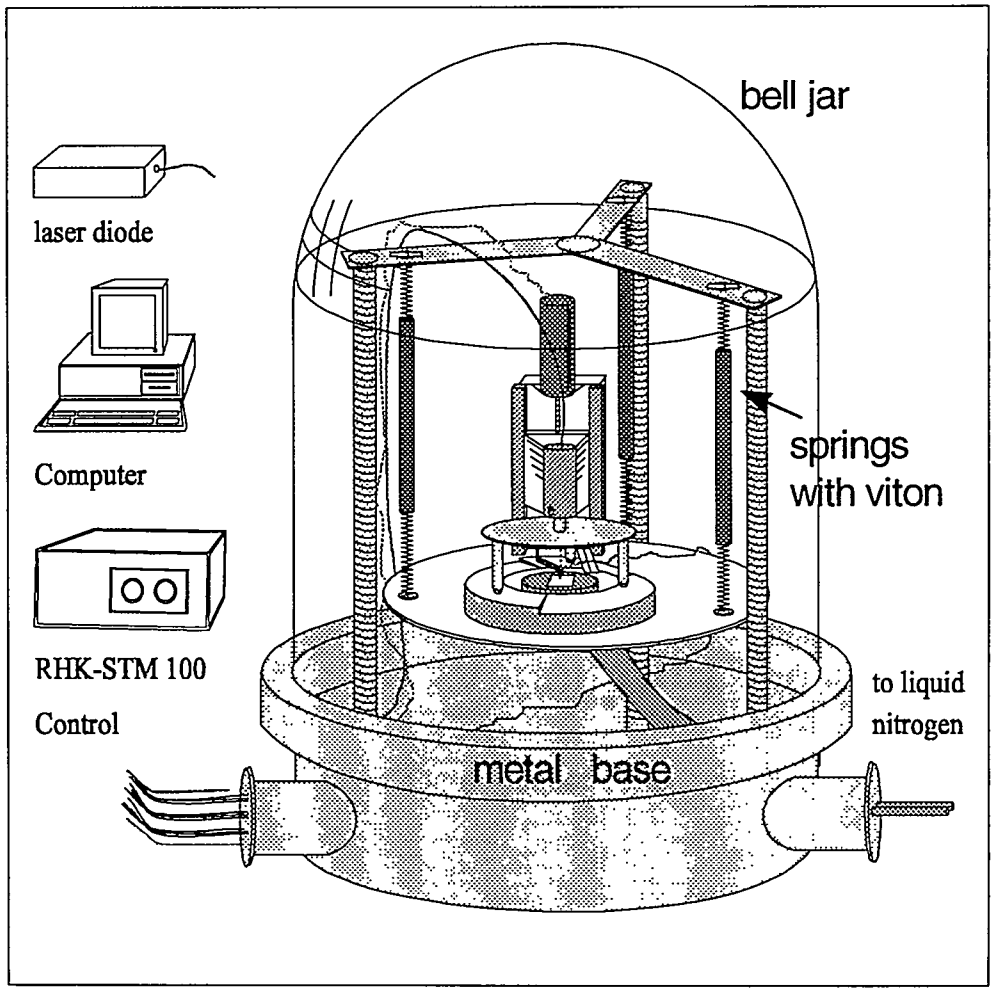

Figure 6.3 A schematic diagram of the SFM in more detail.

6. 2. 3. 1 Ramps: The head sits on ramps ((a) in Fig. 6.4) which are used for the approach and retraction of the tip with respect to the sample. The ramps have a tilt angle of ~2.8 degrees, and have a three fold symmetry. When the head is rotated clockwise with respect to the sample, the head slides down the ramps and approach is facilitated. The ramps were polished extremely well, because even small cracks or asperities can disrupt motion of the head.

6. 2. 3. 2. Piezoelectric Legs: The head consists of a light metal disc to which

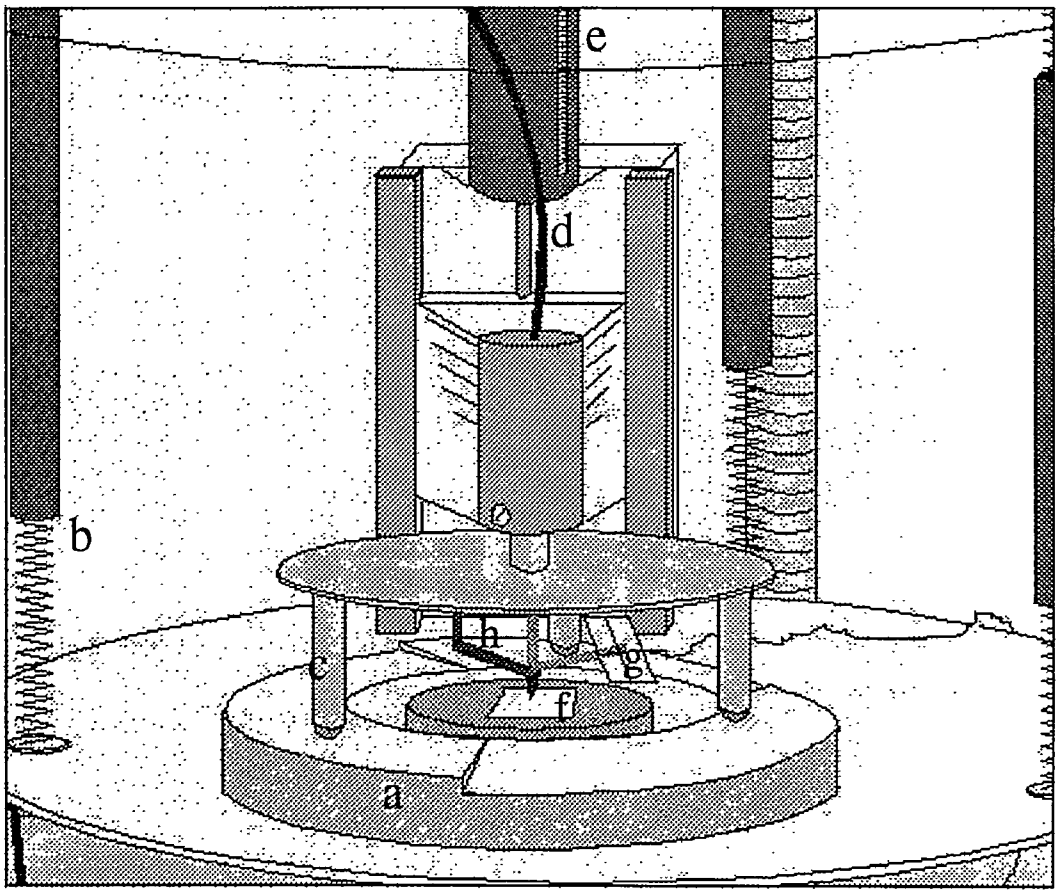

Figure 6. 4. A schematic diagram of the SFM head showing the various components (a) ramps (b) springs (c) Piezoelectric legs (d) Fiber optic (e) single axis micrometer translation stage (f) sample (g) photodiode (h) cantilever

three piezoelectric legs are attached. The piezoelectric legs used are in the shape of hollow cylinders 0.5 inches in length and 0.125 inches in diameter as shown in Fig. 6.4. The tubes were sectored into four regions, which were

electrically insulated from each other. Voltages sent to these regions facilitate motion in the positive X and Y directions and negative X and Y directions. The

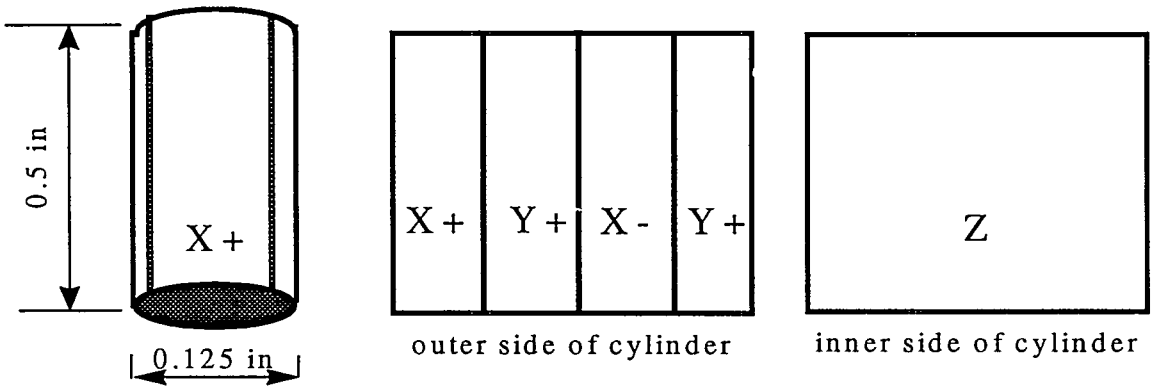

Figure 6.5 Schematic of each piezoelectric tube scanner

inner side of the piezo is used to send voltages for z motion. For rotation of the head a separate switch box needed to be built, whose circuit is shown in Fig. 6.5. In the Fig., 1,2 and 3 are the three piezoelectric sectored legs, and the +/- denote the various sectors as shown in Fig. 6.4. The switch used consists of five stages and six throws (six positions). Switch 1 is used for all scanning. Switch 1-4 are used for moving the head in the X and Y direction. Switch 5, and 6 are used for rotating the head in the clockwise and counterclockwise directions. By using these switches, the head can be moved macroscopically over millimeters over the ramps in all directions. This is done by using saw tooth voltages as inputs, and thereby jerking the head in various directions. Since only one input is used for X+ and one for X-, the scan voltages are summed with the offset voltages. The z voltage necessary for vertical motion is applied to the inner tube

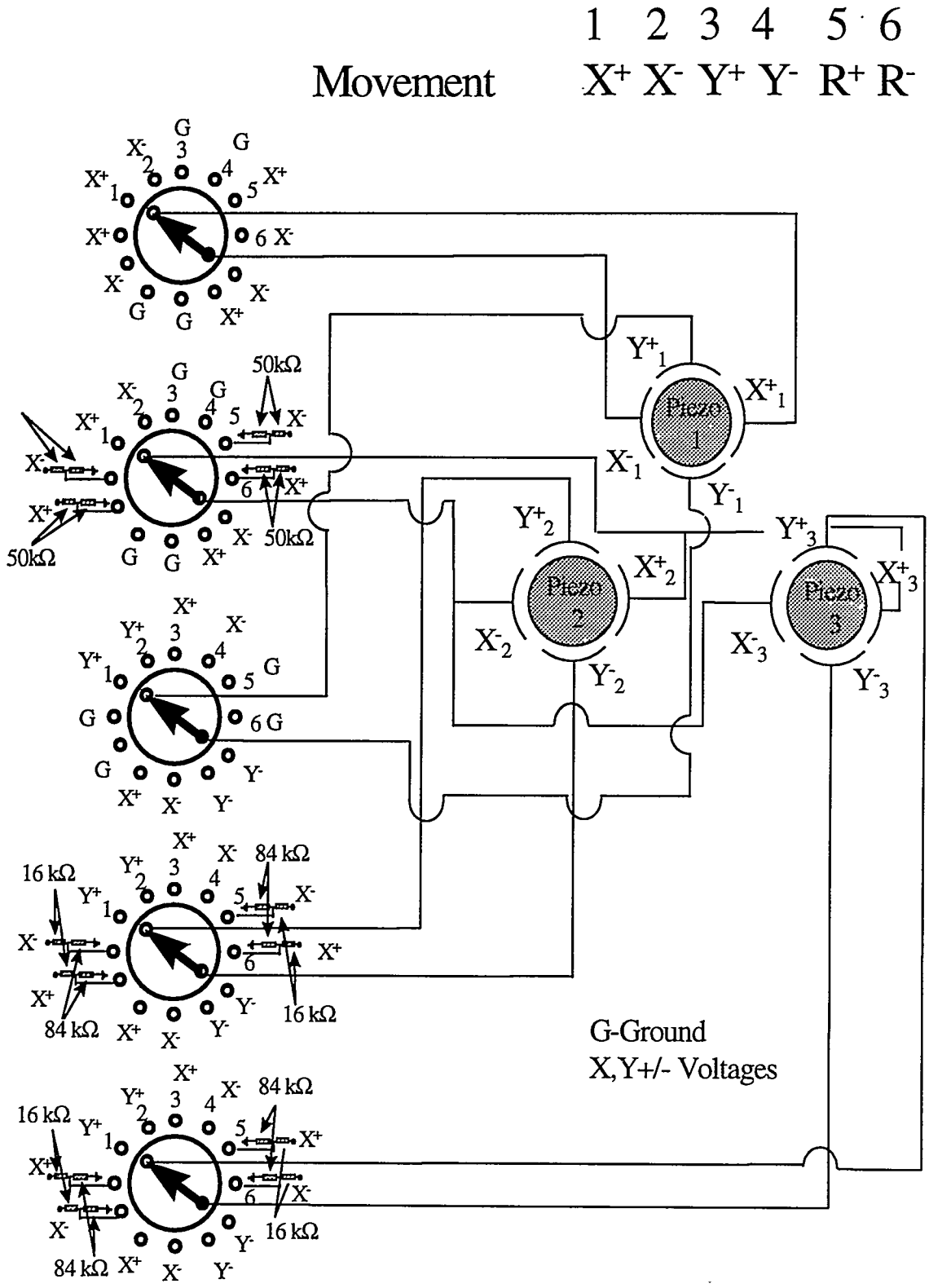

Figure 6.6 Schematic diagram of switching circuitry.

of the piezo legs.

6. 2. 3. 3 Optical Detection: A solid state diode laser from SDL Optics, Inc., Canada (milliwatt, CW laser, 670nm) was coupled to a single mode optical

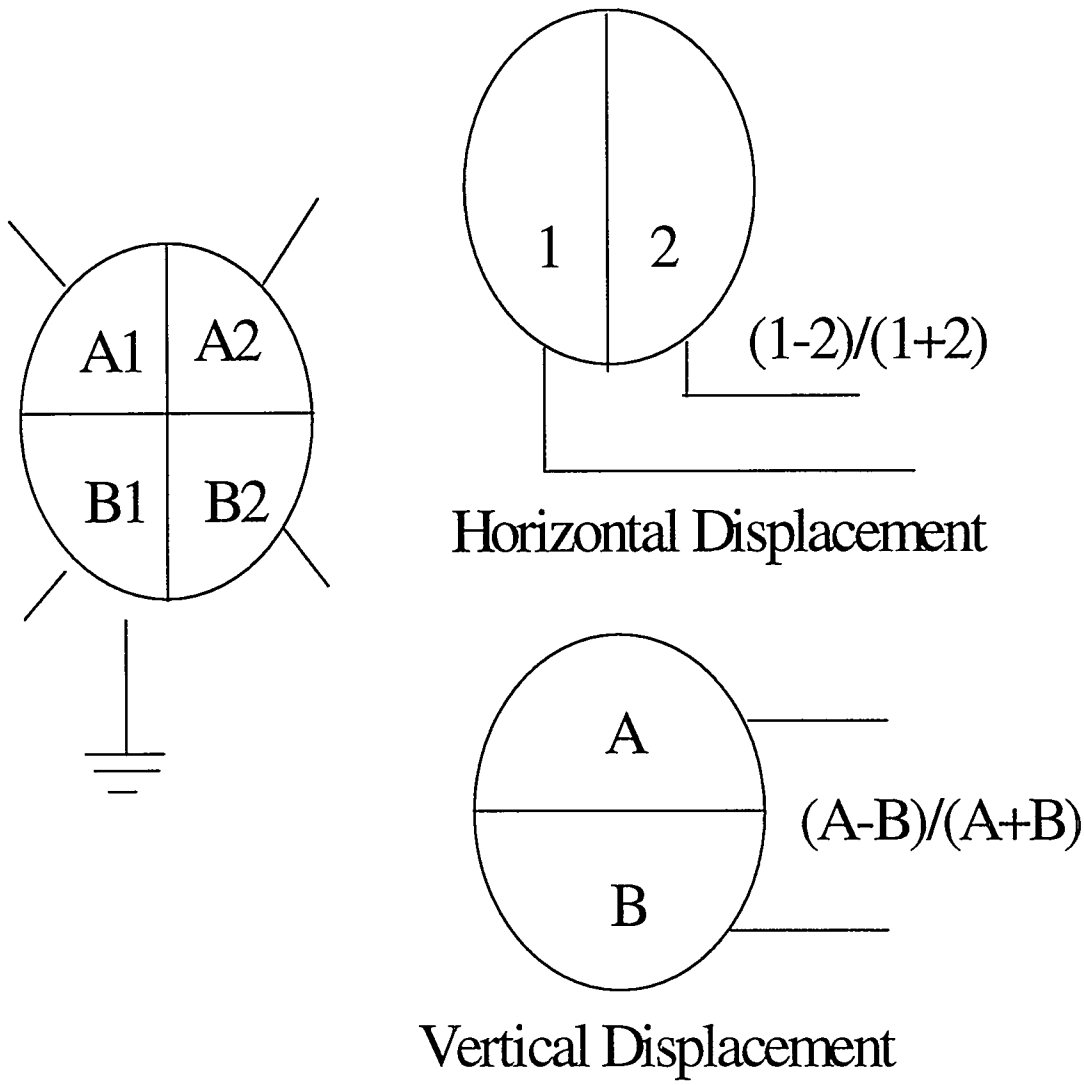

Figrure 6.7 Schematic diagram of photodiode configuration showing signals for vertical and horizontal displacement of the light spot on the diode

fiber

using standard optical fiber coupling tools. This is because it is not convenient and advisable to put a diode laser in a vacuum chamber. The optical fiber was then sent through a vacuum flange which had a single hole bored through it. The hole was sealed with high vacuum Torr seal. The optical fiber was then coupled to a cylindrical lens (SLW 180-29-NC-63) with a refractive index of 0.3393 @ 630nm, from NSG America Inc) which was held rigidly by a lens holder on the head of the SFM. This is done to focus the laser spot on the the SFM cantilever. The position sensitive photodiode (Pin Spot 4D, S4DG) used was purchased from United Detector Technology. It consists of four quadrants. The photodiode was glued with electrically insulating glue to a metal holder which slid on and off the head of the SFM. The wires from the photodiode were configured in a way as shown in Fig. 6.6 such that signals from different quadrants were added and subtracted in such a way that "vertical" and "horizontal" movement of the laser spot could be detected. A two stage amplification system was used. This meant putting a preamplifier chip in the vacuum chamber.

6. 2. 3. 4 Heating/ Cooling scheme: The requirements of both heating and cooling, as well as extremely stable temperature operation, made the design of the heating/ cooling scheme quite involved. The temperature stability has to be better than 0.1 ^{0}C, to avoid thermal fluctuations in the surface of the polymer due to temperature fluctuations. Since a thermoelectric can heat as well as cool depending on the direction of voltage application, it was the first choice.

However it was not possible to get stable operation in the cooling mode. The cooling was achieved by passing liquid nitrogen through a copper block. Two copper braids were connected between this copper block and another small copper piece placed under the thermoelectric module. The thermoelectric was used in the heating mode against the cooling of the liquid Nitrogen. By using a thermistor and a closed loop feedback operation extremely stable cooling was achieved between room temperature and -70 ^{0}C. Using the same thermoelectric chip in the heating mode enabled heating of the sample between room temperature and around 110 ^{0}C. The solder on the thermoelectric chip melts and 120 ^{0}C and the chip would have to be replaced by a high temperature chip, if the need to heat the sample beyond this temperature arises.

6. 2. 3. 5 Miscellaneous: A single axis micron resolution translation stage ((e) in Fig. 6.4) was used to lift the entire head off and on the ramps. The stage was motorized which facilitated control from outside the vacuum chamber. The AFM 100 from RHK technology was used as the sum and difference amplifier, to calculate lateral and vertical signals. The RHK model 100 STM electronics was used as the voltage source for driving the piezo electric tubes.

6. 3 Images: To calibrate the SFM images of various scales and sizes were taken in the contact mode, using the feedback circuitry of the RHK electronics. In Fig. 6.8, a commercial gold diffraction grating was imaged to calibrate the.

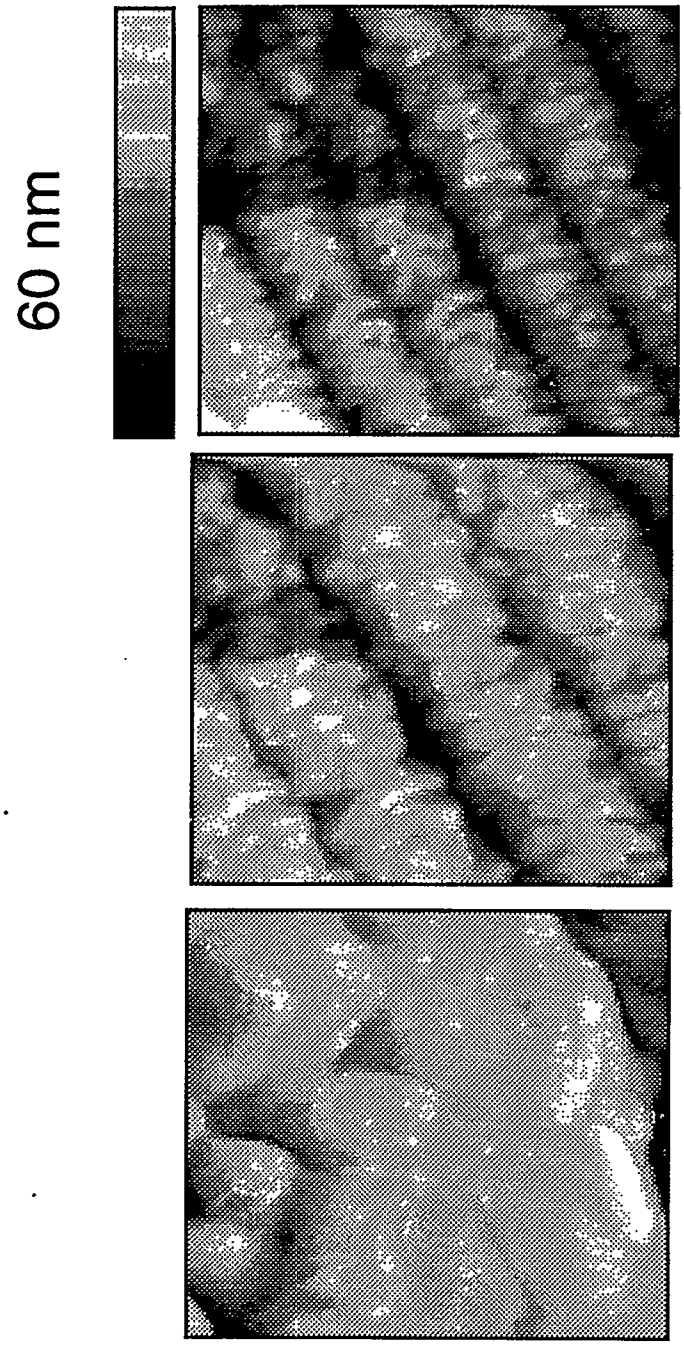

Figure 6.8 Topographic image of a gold diffraction grating at different length scales, showing the spacing of 200nm and gold flakes on one of the grating rows.

instrument, on the sub micron scale. The grating spacing is 200nm, and was used to calibrate the X and Y piezos on this length scale. Accurate height calibration was made by imaging steps on a Silicon grating which are 26 nm high and shown in Fig. 6.9. On the smaller length scale, the surface of NaCl was

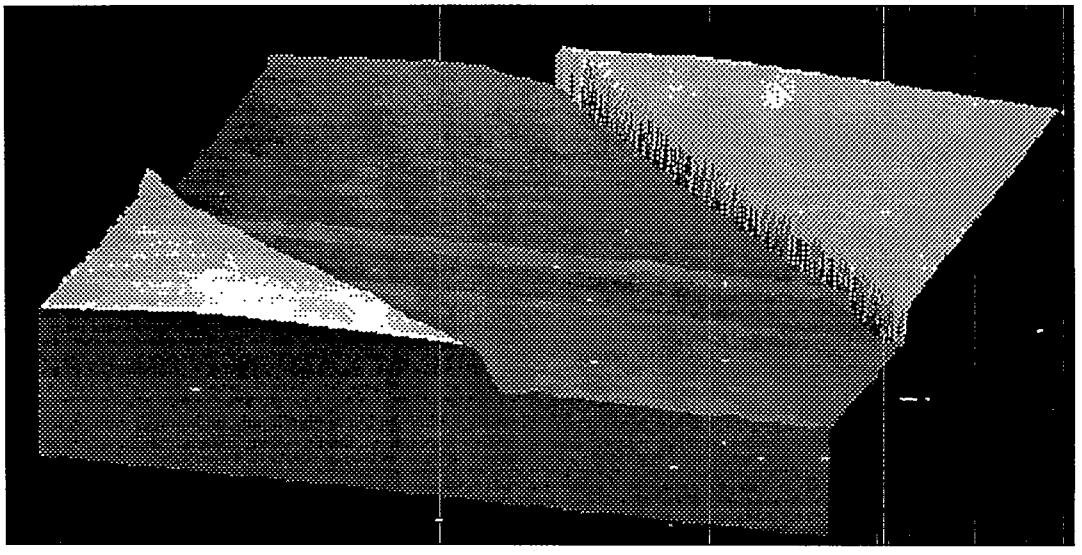

Silicon Grating: Height 26 nm, Width 300nm

Figure 6.9: Topographic image of a Silicon grating showing large flat terraces and steps of height 26 nm

imaged as shown in Fig. 6.10, which shows steps of different sizes and fingers. In Fig. 6.11 a single step on the LiF (100) crystal is shown which is calibrated to be 0.2 nm as per literature results[5] and in Fig. 6.12, a lattice resolved image of the mica surface is shown whose spacing was assigned to 0.53 nm[6].

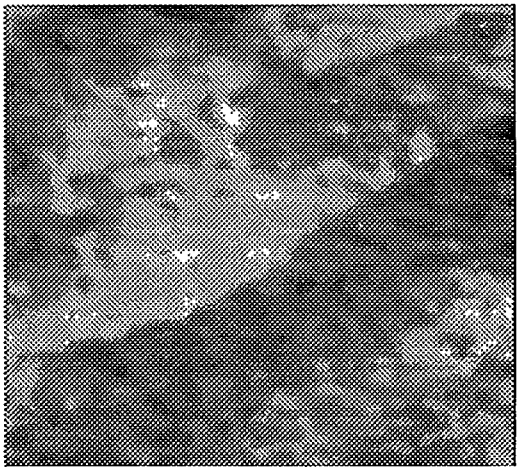

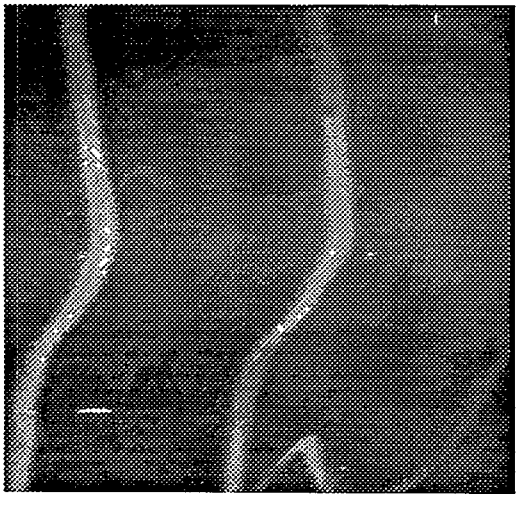

Figure 6. 10 Topographic images of NaCl showing steps and fingers.

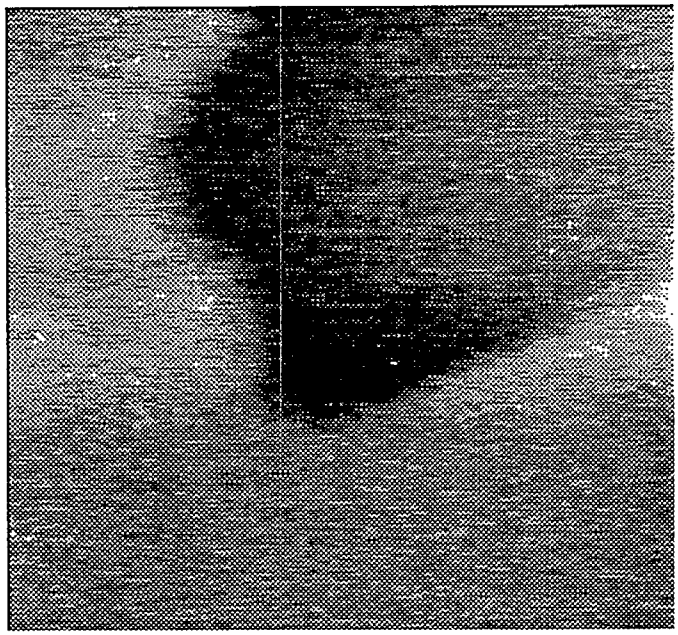

Figure 6.11 A topographic image of LiF showing a single step of height ~0.2 nm and large terraces of area of hundreds of square nanometers.

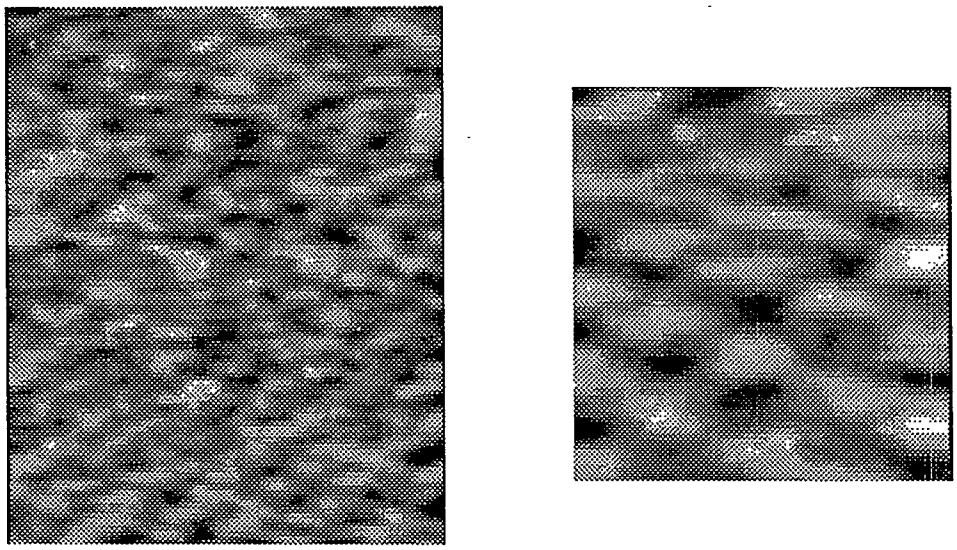

Figure 6.12 Topographic image showing the lattice resolution of mica.

6.4 Conclusions: In this chapter, the successful fabrication of a high vacuum, variable temperature SFM was described. In the following chapter a detailed description of how this instrument was used to measure temperature dependent mechanical properties of polypropylene will be described.

Chapter 6. References:

[1] M. G. Cowie, *Polymers: Chemistry and Physics of Modern Materials* (Intext Educational, New York, 1973)

[2] B. Bogdanov, M. Michailov: Properties of Polyolefins in *Handbook of Polyolefins* ed. C. Vasile, R. Seymour (Marcel Dekker, New York, 1993) page 314.

[3] P. W. Atkins, *Physical Chemistry,* (Oxford University Press, Oxford, 1990) page 732

[4] J. Frohn, J. F. Wolf, K. Besocke and M. Teske, Rev. Sci. Instrum. **60**, 1200 (1989)

[5] E. Meyer and H. Heinzelman in *Scanning Tunneling Microscopy* eds. R. Wiesendanger and H.-J. Guntherodt, (Springer-Verlag, Berlin, 1992)

[6] F. Lin and D. J. Meier, Langmuir **10**, 1660 (1994)

7. Study of the Glass transition of Polypropylene surfaces by Sum-Frequency Vibrational Spectroscopy and Scanning Force Microscopy.

7.1 Introduction: The mechanical properties of polymers such as the elastic modulus are drastically altered as it undergoes a transition from a rubbery material to a glass[1]. This transition is called the glass transition (T_g). Only the amorphous or disordered regions in the polymer undergo this transition. The crystalline areas in the polymer remain unchanged.

The change in the structure of polymers in the bulk[2-4] as they undergo the T_g has been studied using various structurally sensitive spectroscopic techniques like NMR. The line width in these experiments undergoes an abrupt narrowing at the T_g temperature. In various other experiments it has been seen that the coefficient of thermal expansion, refractive index and the heat capacity change rapidly with temperature in the T_g region. Dynamic mechanical analysis studies have shown that the modulus of the glassy polymer decreases by several orders of magnitude as the polymer is heated above the T_g temperature. This remarkable reduction of the modulus is due to the initiation of micro-Brownian motion of the molecular chains from the frozen state with increasing temperature.

It is generally agreed that in the glassy region, thermal energy is insufficient to surmount the potential barriers for translational and rotational motions of segments of the polymer molecules. The chain segments are frozen in fixed positions. The glass transition resembles a second order phase

Name of Polymer	Structure	T_g Temp.	T_m Temp.
Polyethylene	$-[CH_2-CH_2]_n-$	-120 ^{0}C	140 ^{0}C
Polypropylene	$-[C(H)(CH_3)-CH_2]_n-$	-10 ^{0}C	180 ^{0}C
Polyisobutylene	$-[C(CH_3)(CH_3)-CH_2]_n-$	-70 ^{0}C	130 ^{0}C
Polystyrene	$-[C(H)(C_6H_5)-CH_2]_n-$	100 ^{0}C	240 ^{0}C
Polymethylmethacrylate	$-[C(CH_3)(COOCH_3)-CH_2]_n-$	45 ^{0}C	160 ^{0}C
Polydimethylsiloxane	$-[Si(CH_3)(CH_3)-O]_n-$	-123 ^{0}C	-40 ^{0}C
Polytetrafluoroethylene	$-[CF_2-CF_2]_n$	126 ^{0}C	327 ^{0}C
Polyvinylchloride	$-[C(H)(Cl)-CH_2]_n$	87 ^{0}C	227 ^{0}C
Polyvinyledenechloride	$-[CCl_2-CH_2]_n$	-17 ^{0}C	200 ^{0}C

Table 7.1 A list of the glass transition temperatures and melting temperatures for some common polymers.

transition, unlike the melting transition which is a first order transition with an enthalpy of fusion. However the glass transition is not a true thermodynamic transition, infact it is sometimes referred to as a "kinetic transition" , in that even the same method for the detection of T_g may yield different results depending on the time scale. If the experiments are performed over short time scales the apparent T_g is raised. This means that at extremely small time scales all the amorphous polymers behave as glasses, whereas at extremely long time scales, all these same polymers behave as viscous rubbers.

The bulk T_g temperature of different polymers is listed in Table 7.1. As can be seen the temperatures at which the T_g occurs depends on the chemical structure, flexibility of the molecular chains (low T_g temperature for polyethylene), steric hindrance, bulkiness of the side groups (higher T_g temperature for polystyrene as compared to polyethylene), and symmetry (lower T_g temperature for polysiobutylene as compared to polypropylene).

The chain freezing dynamics and various relaxation phenomenon occurring in the bulk has been extensively studied and is still a major research field.

However recently some studies have been directed at observing the changes occurring at the surface[5-9] of the polymer during the T_g. X-ray Photo Electron Spectroscopy (XPS), Secondary Ion Mass Spectrometry (SIMS) and Neutron Reflectivity have observed an enhancement of chain ends at the polymer surface. Considerable interest has been generated with the suggestion that surfaces of polymers can be different from the bulk not only due to enthalpic, but also entropic forces[10]. Entropic forces which result in a higher concentration of molecular chain ends at the surface lead to various phenomena, including the depression of the glass transition temperature (T_g) observed in low-molecular-weight polystyrene[8-10]. Scanning Force Microscopy has been used to measure the friction vs scanning speed on polymer surfaces and thereby determining a T_g temperature, which in several cases is depressed compared to the bulk value[9].

In this chapter, the first measurement of vibrational spectra of a polymer surface as a function of temperature across T_g using sum-frequency generation (SFG) spectroscopy[11] is reported. In addition to getting chemical information of groups present at the polymer surface we can monitor directly molecular structural changes taking place at the surface during the glass transition by the relative peak intensity changes, thereby demonstrating the viability of SFG as a new probe to study the glass transition on polymer surfaces.

Since the modulus of the polymer changes by orders of magnitude during the glass transition, we have measured the elastic modulus of the polymer surfaces using scanning force microscopy[12] (SFM). The friction vs load curves were also measured as a function of temperature. However since the friction curves contain both information about the contact area and the material properties they are more difficult to interpret.

By studying the polymer surfaces with SFG and SFM, we can correlate changes observed in the molecular surface structure to changes observed in the elastic modulus. This hopefully provides a deeper insight into the surface structural changes through the glass transition. Moreover by measuring the T_g temperature by two independent techniques we can understand the techniques better as well as get a more complete picture of the changes occurring at the surface.

The polymers chosen for the study were Atactic Polypropylene (APP) and Isotactic Polypropylene (IPP). This is because the polymers represent chemically simple and widely used polymer systems. The T_g temperature is ~ -10

^0C[13], this temperature being not very far away from room temperature is relatively easy to achieve experimentally in both SFG and SFM measurements. Lastly, APP and IPP can be obtained in high purity and they have been studied extensively studied in the bulk.

Isotactic Polypropylene (>60 % Crystalline)

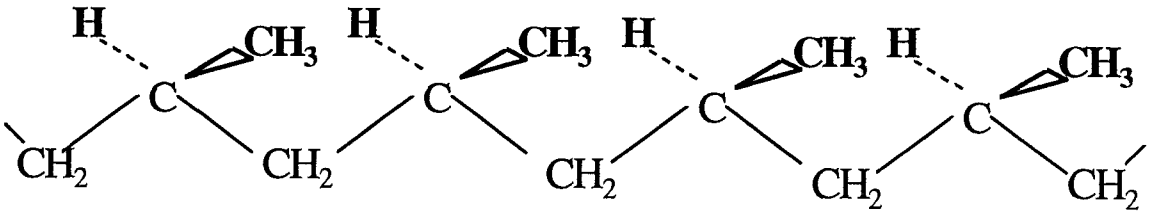

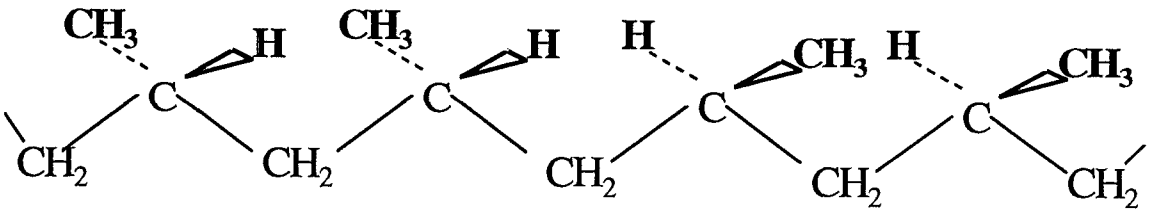

Atactic Polypropylene (<5% Crystalline)

Figure 7.1 Chemical Structure of Isotactic and Atactic Polypropylene. The methyl groups are regularly arranged i.e. on the same side of the polymer chain backbone in IPP whereas they are randomly arranged in APP.

7. 2. Experiments:

7. 2. 1. Samples: A schematic diagram of the chemical structure of APP and IPP is shown in Fig. 7.1. Depending on the stereoregularity of attachments of the monomer unit propylene $(H_3C)(H)C=CH_2$, there can be isotactic, syndiotactic and atactic polypropylene. IPP has a regular arrangement of the CH_3 groups, as can be seen in Fig. 7.1 in which all the methyl groups are on the same side of the backbone. APP has a random arrangement of methyl groups around the polymer backbone.

Because of the high stereoregularity in IPP, better packing is facilitated which results in a high degree of crystallization (>60 %) as compared to the poorly packed highly amorphous APP. APP (viscosity = 23 poise) and IPP (M_w = 250 K, density = 0.90 gm/ c.c.) were purchased from Aldrich Inc. To increase the tactic purity of the sample, i.e. to increase the atactic content in APP and decrease the atactic content in IPP, the purification scheme of *Boerma et al* [14] was used. For APP, it involves an extraction with boiling ether in which the amorphous component readily dissolves. The ether extract is then precipitated with acetone. The ether extract which does not precipitate contains low molecular weight hydrocarbons and this portion was not investigated any further. The precipitate represents the pure atactic portion of the polymer, which was used in the further study of APP.

For IPP, the polymer was extracted in boiling ether, however in this case the dissolved or clear portion of the ether extract was discarded and the

undissolved portion was filtered off. This part was then extracted with acetone, isopropyl alcohol and n-heptane. The filtered solid represents the highly crystalline IPP used in this study. Proton and ^{13}C Nuclear Magnetic Resonance (NMR) spectra of the polymers dissolved in deuterated 1,2-dichlorobenzene at 100 ^{o}C, was used to verify the tactic purity of the samples. By comparing the spectra with published spectra[15] the samples were determined to have a tactic purity of ~100%. It was also observed that reproducibility of the measurements with SFM (which is a spatially local technique) was greatly increased after tactic purification of the polymer samples.

It was determined, by Differential Scanning Calorimetry, that the percentage crystallinity of APP was < 5% and that of IPP was > 60%. The polymer films were prepared by casting dilute solutions of the polymer in o-xylene onto quartz plates. We heated the films to 140 ^{0}C for 6-8 hours and cooled at around 5 ^{o}C / min. In order to reduce the possibility of oxidation some samples were heated at 100^{o} C in vacuum for around 4-5 days and cooled in the same way. No discernible difference was observed between the samples. The sample thickness was on the order of 100 microns.

7. 2. 2: SFG: The SFG set up is described in chapter 3. Since temperature dependent measurements needed to be performed, all experiments were performed in vacuum at pressures below 10^{-5} Torr. All spectra were obtained with the sum-frequency output, visible output and infrared output s-,s- and p-polarized, respectively.

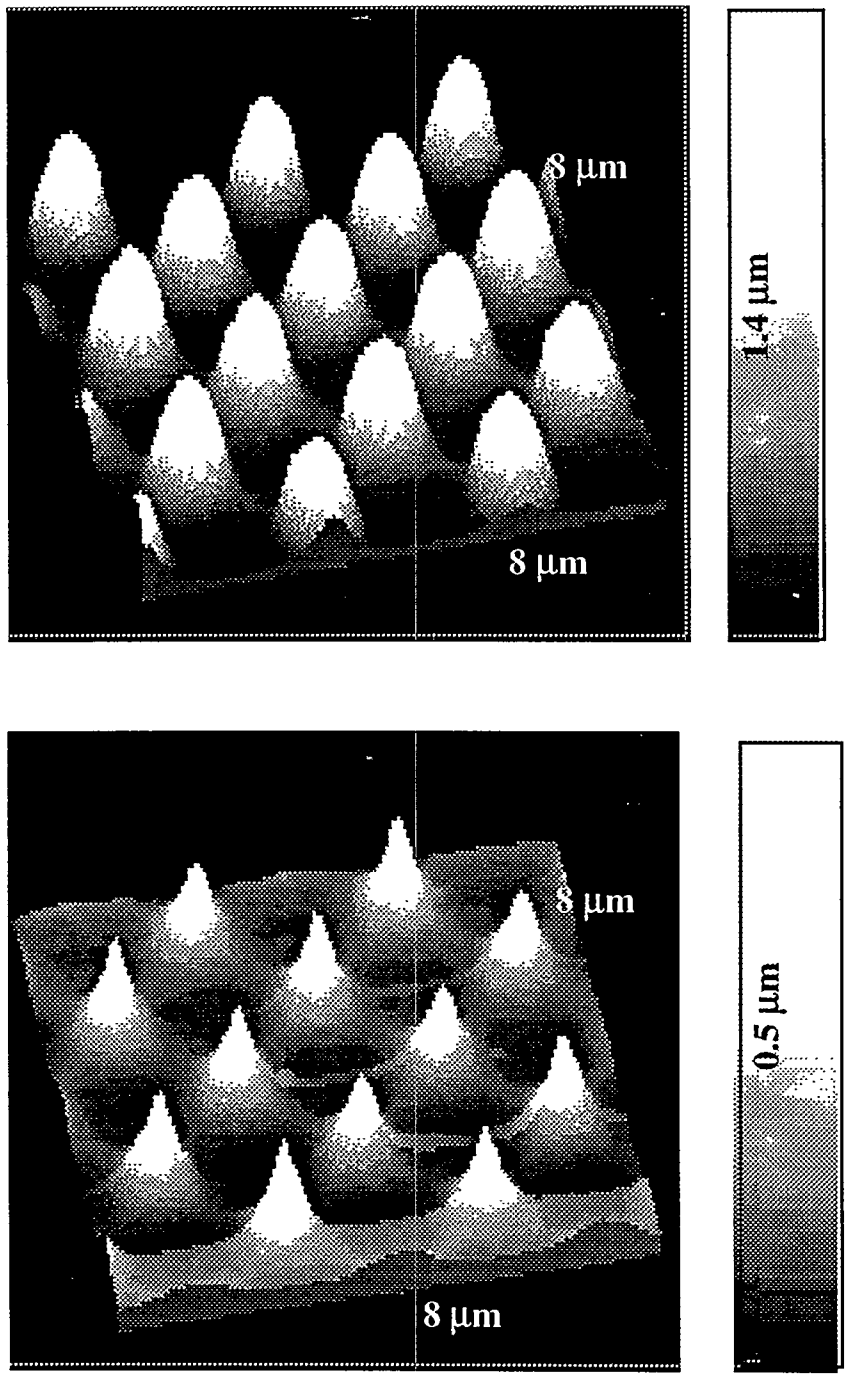

Figure 7. 2 Topographic images of a 3-d Si grating[16] which has features that are sharper than the SFM tip. As can be seen the image scanned with a blunt tip (above) is bigger than that scanned with a sharp tip (below).

7. 2. 3. SFM: The temperature dependent measurements were performed in vacuum at pressures of ~10^{-5} Torr using the SFM described in chapter 6. The cantilevers of our SFM used in the experiment were commercial, micofabricated, silicon cantilevers from NT-MDT[16]. The cantilever and the tip are coated with a thin film (20nm) of W_2C (Tungsten Carbide). This hard and inert coating reduces the possibility of damage done to the tip during the measurement. Tips of different radii of curvature in the range of 20 nm - 1000 nm were used. Before any measurement, the radius of curvature of the tip was determined by imaging, in contact mode, structures which are sharper than the tip. Fig. 7.2 shows topographic images of the same 3-d structures[16], with two different tips of radii of 1000 nm and 100 nm respectively . As can be seen, the radius of the tip is convoluted into the image and the structure imaged with the larger tip appears much larger than the one imaged with the smaller tip. From such images the radius of the tip was determined.

7. 2. 4. SFM measurements: We have used SFM, with tips of a variety of radii of curvature (20nm to 1000nm), to measure the elastic modulus of the polypropylene surface as a function of temperature. In chapter 4, the fundamental differences between using tips of different radii of curvature was delineated. It was concluded that in the regime of elastic contact mechanics, sharper tips apply greater average pressure, making a smaller contact area with the surface and penetrating a larger distance into the surface. Thus by using

tips of different radii in this study, it is possible to vary the contact pressure, contact area and the penetration depth in the experiment.

7. 2. 5. Modulus measurements: SFM can be used to measure the interaction

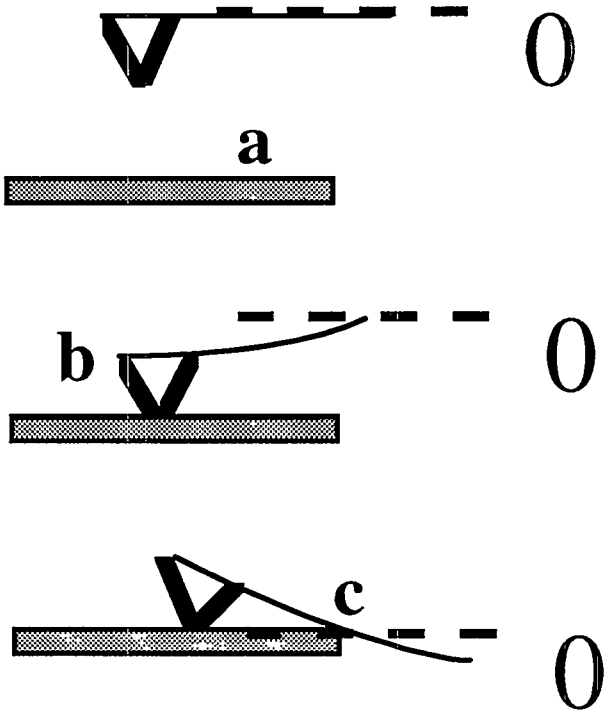

Figure 7. 3 Schematic diagram of the acquisition of a force curve.

forces between the tip and the local surface. Fig. 7.3 displays the schematic diagram of the acquisition of a force curve. Initially the cantilever / tip is far away from the surface and this is denoted by a. The tip is then pushed towards

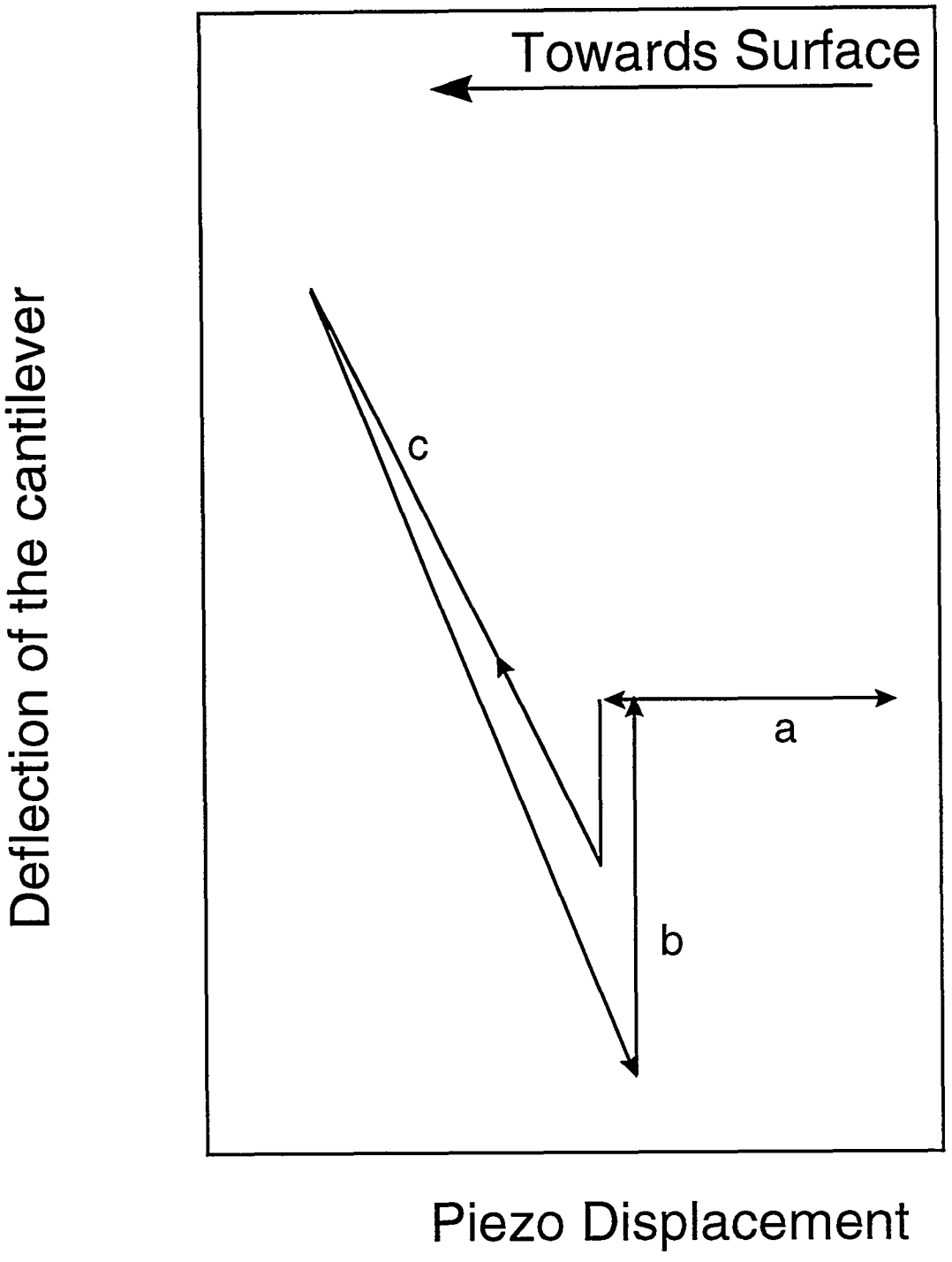

Figure 7. 4 Schematic diagram of an approach and retract curve (direction of arrows) and the three main parts of the curve a, b and c.

the surface, at some distance away from the surface the tip feels the attractive force of the surface and gets attracted towards it, part b of Fig. 7.3. If the tip is pushed further into the surface it is repelled by it, this is because the surface has a finite rigidity characterized by an elastic modulus. In this way the tip can be brought into and out of the surface to generate approach and retract curves. The deflection of the cantilever can then be plotted vs the distance through which the cantilever is moved. The latter is the voltage applied to the piezoelectric used to move the tip up and down. The curve then generated is depicted in Fig. 7.4 which consists of three main regions illuminated by the schematics. In region a, the tip is far away from the surface with little or no interaction between the two, hence the tip is not deflected. In region b, the tip feels an attractive force towards the surface. If the gradient of this force is larger than the force constant of the tip, the tip will become unstable and snap into contact with the surface.

The stability criterion can be derived as follows, In Fig. 7.5 we can see that the cantilever can be modeled as a spring of energy $\frac{1}{2}kz^2$, where k is the spring constant of the cantilever and z is the displacement of the cantilever from its equilibrium condition. The surface has some potential energy which can be denoted as $V(z)$, which may look like the diagram shown in Fig. 7.5

Then the total energy of the cantilever/ tip -surface system can be represented as,

$$U = \frac{1}{2}kz^2 + V(z),$$

the stability criterion, is then that the curvature of the potential function of

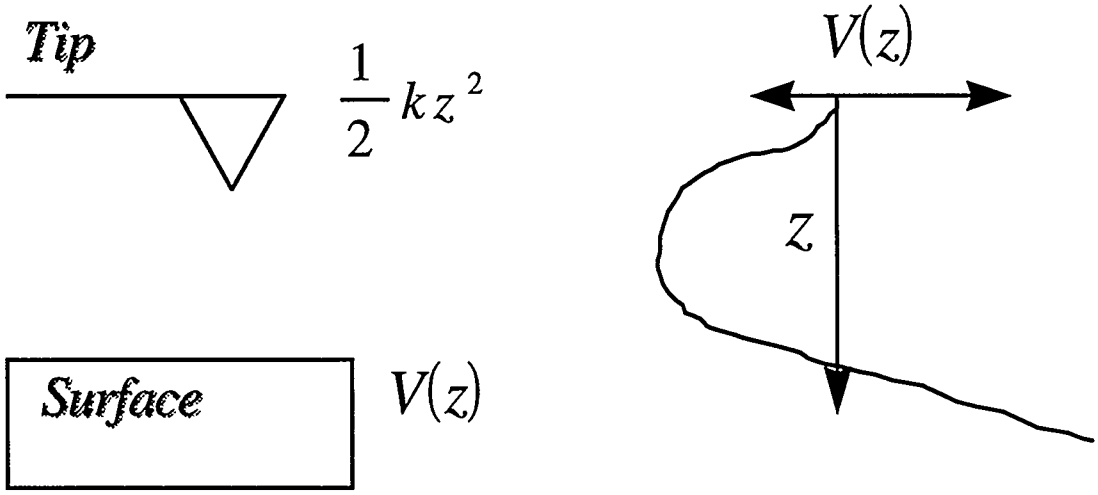

Figure 7. 5 A schematic diagram of the tip and surface energy and a typical potential energy diagram of a surface as a function of distance z.

distance lies at a minima, or

$\frac{\partial^2 U}{\partial z^2} \geq 0 \Rightarrow k - k' \geq 0$, where

$k' = \frac{\partial F(z)}{\partial z}$, which is an effective force constant of the surface potential.

Hence it can be seen that if the spring constant of the cantilever is smaller than that of the surface potential then the system becomes unstable this is why the cantilever snaps into the surface and part b of the force curve is a sharp line. If we use cantilevers with high force constants, which is the case in Chapter 4, the

system remains stable and we can map out the true attractive part of the surface potential as shown in Fig. 7.6. and Fig. 4.11 part a.

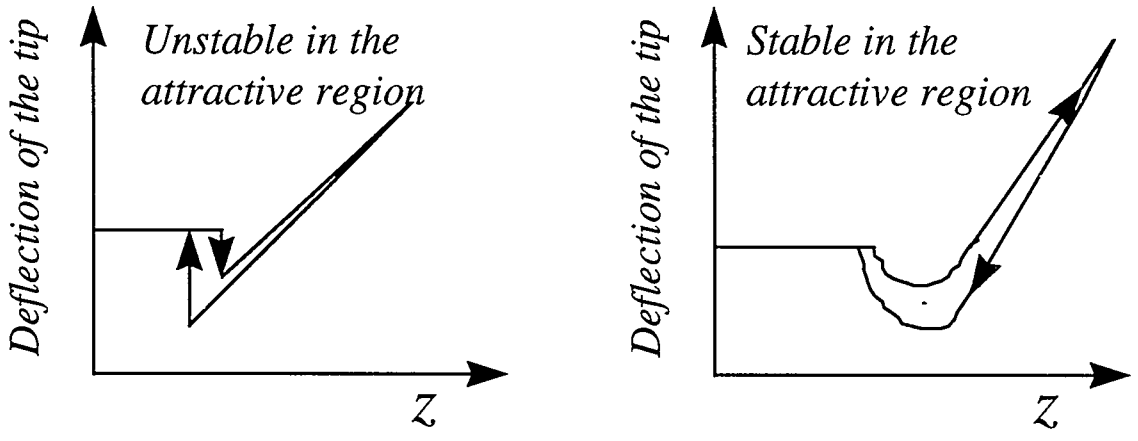

$$k - k' > 0 \Rightarrow Stable$$
$$k - k' < 0 \Rightarrow Unstable$$

Figure 7. 6 Criteria and force curves for stable and unstable operation of the cantilever in Part B of figure 7.4 i.e. the attractive region.

Returning to Fig. 7.4, in region c, the tip interacts with the repulsive part of the potential of the surface. In the curve the abscissa (the numbers plotted on the y-axis) correspond to the distance through which the cantilever deflects. Let us call this variable y, the force exerted by the tip can be represented by $W = ky$. However this load will cause an elastic deformation of the softer sample which

can be calculated using Hertzian contact mechanics outlined in Chapter 2. The penetration depth of the tip into the sample under the load W, is given by,

$$\delta = \left(\frac{9W^2}{16RE^{*2}}\right)^{1/3} = \left(\frac{9(ky)^2}{16RE^{*2}}\right)^{1/3}$$

where R is the radius of curvature of the tip and E^{*} is the modified elastic modulus of the sample.

Hence the total distance moved by the piezo is equal to $\delta + y$. On the x axis we have plotted the voltage which is proportional to this distance, and the slope of line c can be represented by,

$$Slope \propto \frac{\partial y}{\partial x} = const \frac{\partial y}{\partial x},$$

However from the above description

$$ay = bx - \delta = bx - \left(\frac{9(ky)^2}{16RE^{*2}}\right)^{1/3}$$

where a and b are constants.

Hence it can be seen that the slope of line c (in fig. 7.4) can be obtained. We can conclude that if the slope of the part c is high it means that there is very little deformation of the sample or δ is small. This means that the elastic modulus of the sample is high. Alternatively if the slope of line c for the same load is small it means that the elastic penetration depth δ is large and the elastic modulus of the sample is small. Hence by monitoring the slope of part c of the approach curve we can get a qualitative idea of the elastic modulus changes of the

sample. It must be noted that for a given cantilever force constant k, tip radius R, this system is sensitive to a range of elastic moduli.

This can be seen in the following example, Suppose the cantilever moves by 0.99 nm, the piezo by 1 nm, the slope is then 0.99. In this case the elastic deformation is 0.01 nm, let the elastic modulus of this polymer be E. If the elastic modulus of the polymer then increases by a factor of 10, the deformation will decrease to 0.005 nm, hence the cantilever will move by 0.995 nm and the slope will be 0.995 which is not a big change and may not be detected.

The system is most sensitive when the elastic deformation of the sample and the deflection of the tip are of the same order, e.g. 5 nm and 5 nm. If then the elastic modulus of the sample increases by a factor of 10, the deformation will decrease to 1.1 and the slope will then change from 0.5 to 0.89. In our experiments using different tip radii and force constants of the cantilever, we were sensitive to elastic modulus changes in the region of 0.1 GPa to 10 GPa. This combination has been chosen because the elastic modulus measured on APP was found to be 0.15 GPa and that of IPP to be 1 GPa at room temperature. (see chapter 4). Hence we will be most sensitive to changes in the elastic modulus of APP / IPP in this region if the modulus of these polymers increases till around 10 GPa. The changes of slope with elastic modulus is a non-linear function and the changes in the slope of the curve should not be construed as changes in the exact changes in the elastic modulus. However an increase in slope means an increase in the elastic modulus of the sample and vice-versa.

Returning to Fig. 7.4, if the tip is now retracted away from the surface, it breaks elastic contact in part c of the curve and an opposite behavior is observed to sample approach. Often a hysteresis is observed in the curve and is related to the creep in the piezoelectric ceramic, and dissipative losses such as wear in the sample. The pull-off force, or the force required to break contact between the two surfaces represents the adhesion of the surfaces. The pull-off force is predicted to increase linearly with the radius of curvature of the tip as can be seen in the JKR model (Chapter 2). Hence by measuring force curves we can learn about elastic deformations (elastic modulus) represented by part c of Fig. 7.4, plastic deformations (wear) represented by the hysteresis between approach and retract curves in Fig. 7.4 and adhesion between the tip and the surface (part b in Fig. 7.4).

7. 2. 6. Friction: Friction vs Load curves were measured on IPP and APP at different temperatures and the method used to generate these curves is described in Section 4.4.3

7. 2. 7. Cooling characteristics: To allow a comparison between measurements performed with SFG and SFM, the same cooling scheme was used in both measurements. This is because of the kinetic effects on the glass transition of polymers as described above. The polymer samples were cooled in steps and involved a stabilization time at each temperature of around 30 minutes.

7. 3 Results and Discussion:

7. 3. 1 SFG spectroscopic measurements above and below the T_g temperature: Shown in Fig. 7.7 and Fig. 7.8 are typical SFG spectra for APP

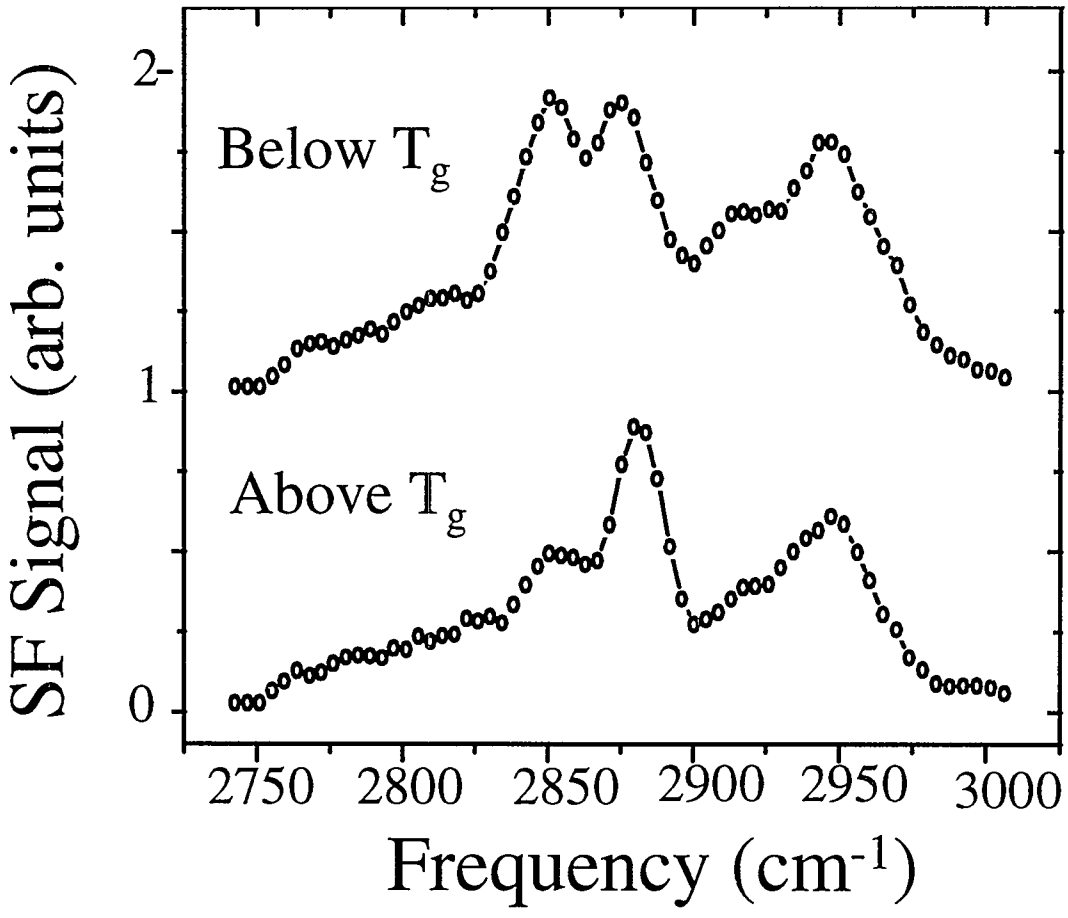

Figure 7.7 SFG spectra of APP above and below the glass transition.

and IPP respectively, in the C-H vibrational stretch region above and below the T_g. They were taken with the samples in a vacuum of 10^{-5} Torr.

The spectra at room temperature (above T_g) are similar to the previously published spectra[17] for APP and IPP in air at room temperature. For both APP

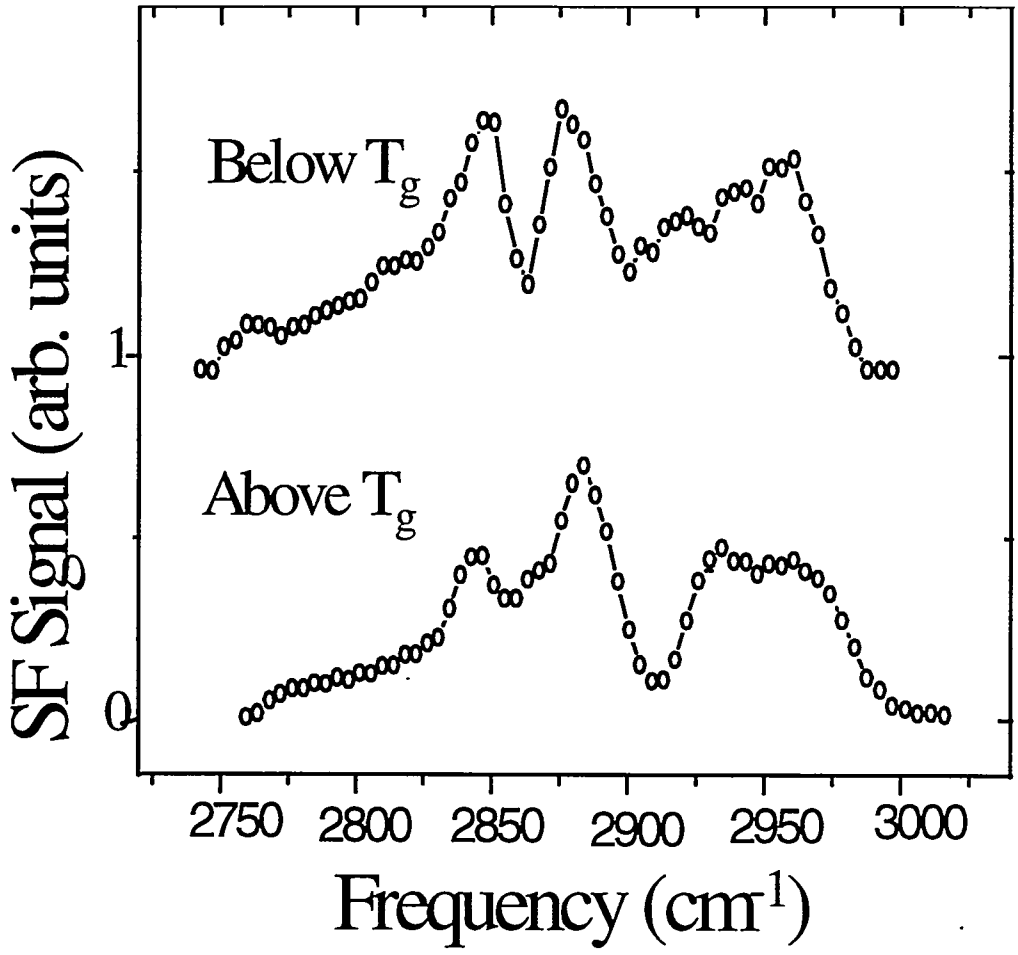

Figure 7.8 SFG spectra of IPP above and below the glass transition.

and IPP, the peaks at 2845 cm^{-1} and 2880 cm^{-1} can be assigned to the symmetric stretch of methylene (CH_2) and methyl (CH_3) groups, respectively. For APP, the broad peak centered at 2940 cm^{-1} is due to the Fermi resonance between the CH_3 symmetric stretch and bending overtone modes. The

antisymmetric CH_2 stretch at 2920 cm^{-1} appears as a shoulder on the broad peak. For IPP, the peaks at 2920 and 2950 cm^{-1} can be assigned to the antisymmetric stretch of the CH_2 and CH_3 groups, respectively. The ratio of the methylene peak at 2845 cm^{-1} to the methyl peak at 2880 cm^{-1} is higher for IPP than APP. Below T_g, the spectra for both APP and IPP show the same four peaks observed at room temperature, but the peak intensity at 2845 cm^{-1} (symmetric CH_2 stretch) has increased significantly, while those of the other three peaks have hardly changed.

The observed spectral change across the T_g indicates that the CH_2 groups become better polar-oriented below the T_g, while the CH_3 groups have their orientation hardly changed. In polypropylene the CH_2 groups form the backbone of the polymer chain, and the CH_3 groups are the side (pendant) groups. Our observation therefore suggests that below the T_g, the polymer chains become more ordered with the CH_2 groups pointing out of the surface. Above the T_g, the chains are more disordered and the CH_2 groups more randomly oriented. At all temperatures, the CH_3 groups being more hydrophobic, orient preferentially away from the surface.

7. 3. 2 SFG measurements as a function of temperature: SFG spectra for APP and IPP taken at different temperature upon cooling from room temperature are shown in Figs. 7.9 and 7.10 respectively. As can be seen from the figures the main change occurring in the spectra is the intensity of the symmetric CH_2 peak at 2845 cm^{-1}. The symmetric CH_3 and the antisymmetric CH_2 and CH_3

peaks remain unaffected. We can deduce from each spectrum the strengths of individual modes[18]. We plot in Fig. 7.11 the ratio of the symmetric stretch

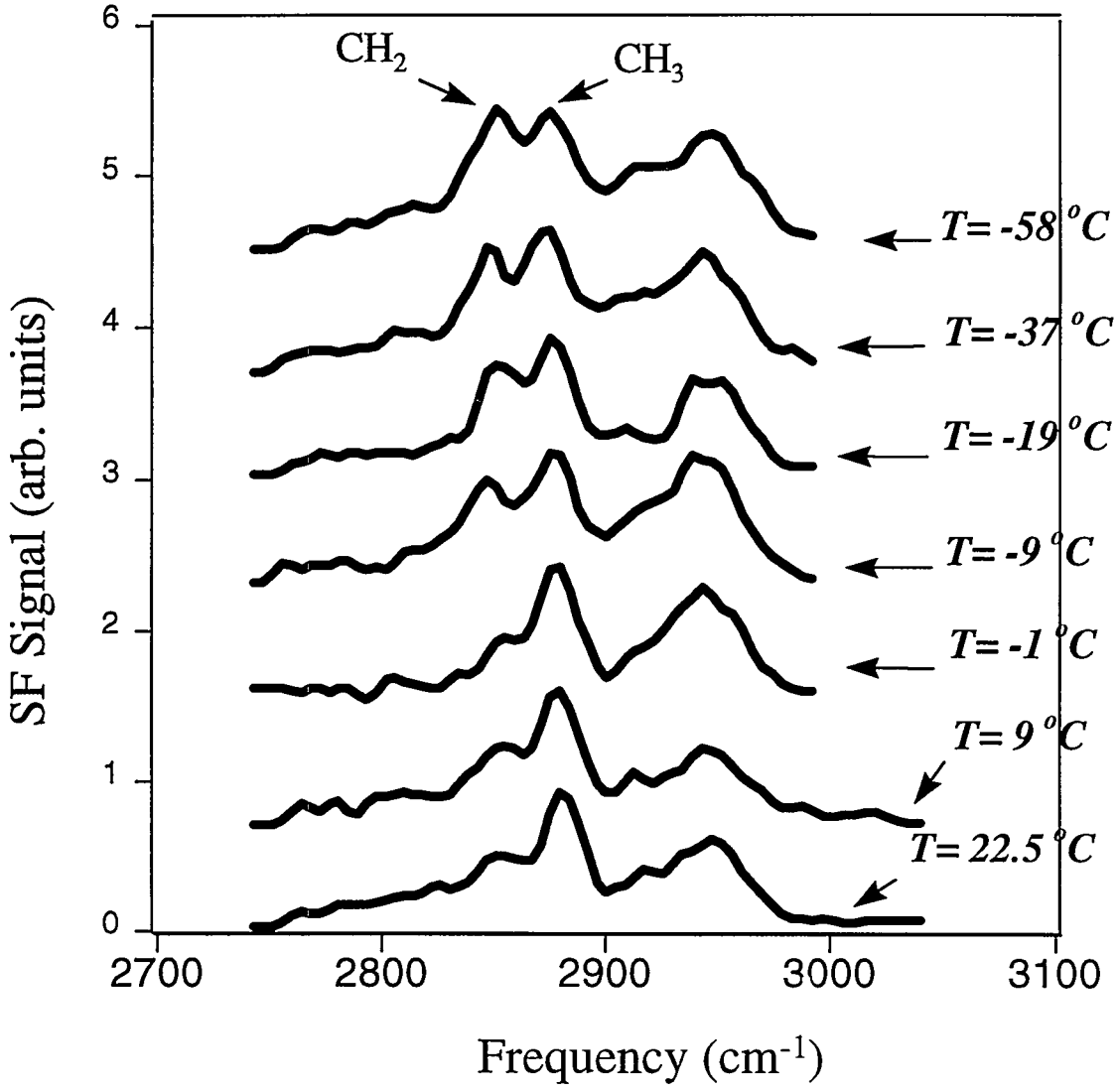

Figure 7. 9 SFG spectra of the APP surface between 22.5 °C and -58 °C.

modes of CH_2 and CH_3 as a function of temperature to qualitatively describe how the surface structure changes with temperature. The data show that the ratio has

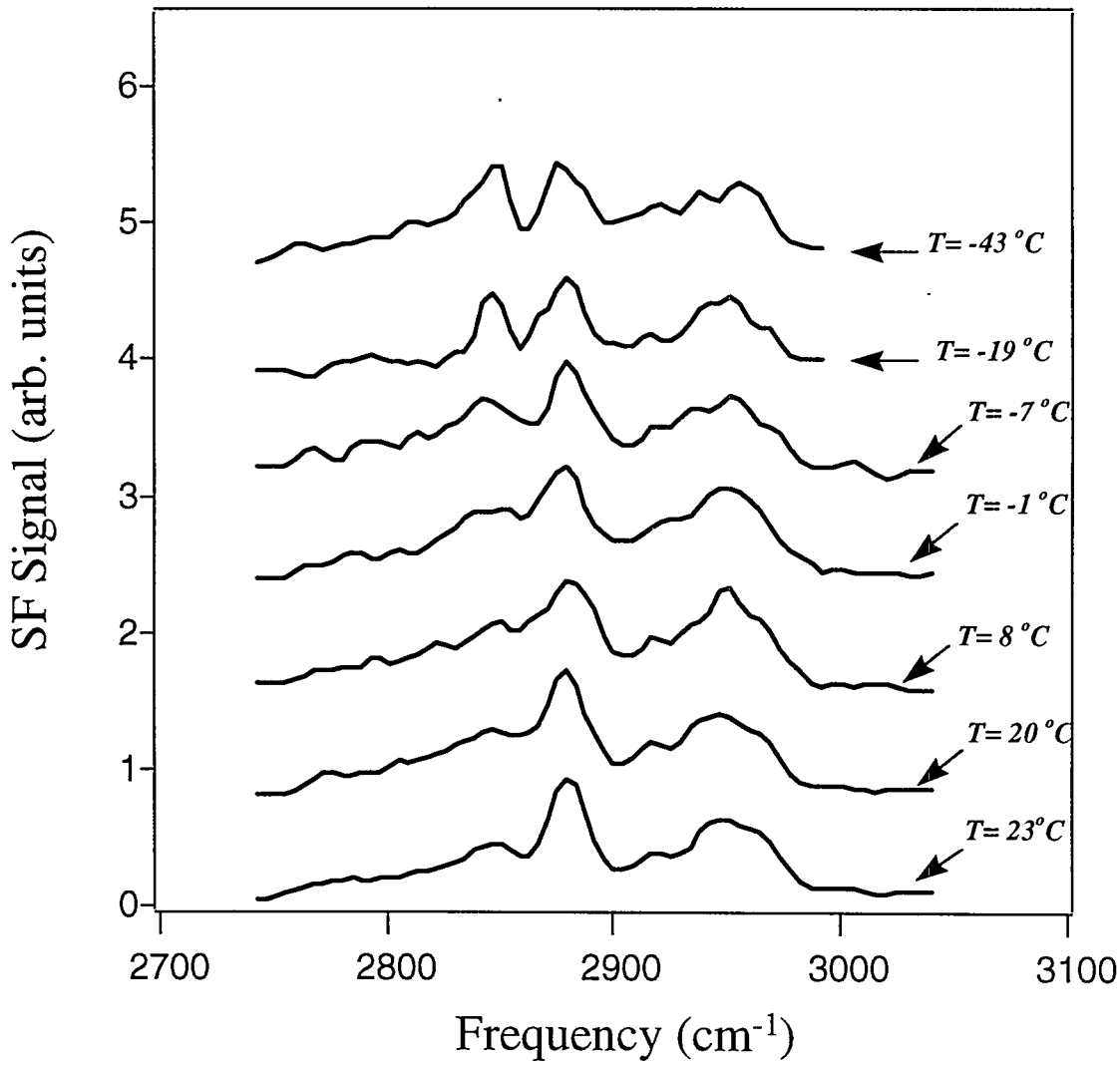

Figure 7. 10 SFG spectra of the IPP surface between 23 ^{0}C and -43 ^{0}C.

a sharp increase in the temperature range between 0 and -20 °C, more prominent for APP than IPP. Since the bulk glass transition of polypropylene is

known to occur in this temperature region, the observed spectral change can be directly correlated to the glass transition. Obviously, in this case, there is little

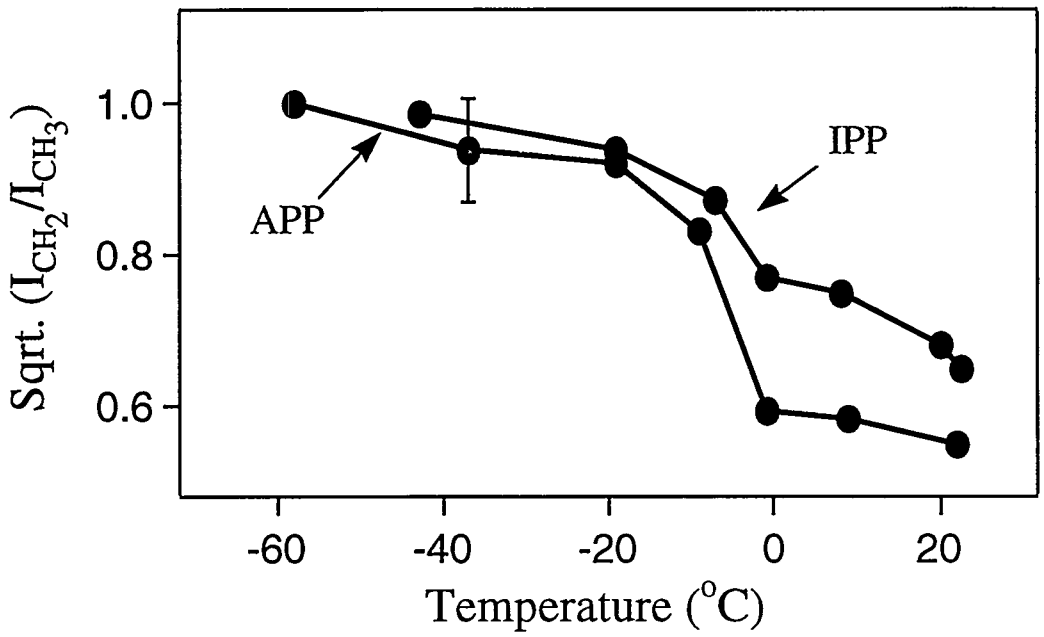

Figure 7.11 The relative strengths of the CH_2 and CH_3 modes as a function of temperature.

difference between the T_g temperature of the bulk and that of the surface.

The more prominent spectral change for APP as compared to IPP shown in Fig. 7.11 confirms that the changes are associated with the glass transition of the polymer. IPP is a semicrystalline polymer whereas APP is amorphous. It is known that the glass transition involves only the amorphous component of the polymer. Since the amorphous content is larger in APP (>95%) than in IPP (<40%) we should expect a more pronounced change in APP and this is what we

have observed. Hence the SFG spectra as a function of temperature suggest a more dramatic ordering of the backbone or the CH_2 groups on the surface during the glass transition.

7. 3. 3. SFM measurements with sharp tips: Force curves were measured at different temperatures on APP and IPP using conventional tips of radii of curvature of 50-100nm. Around room temperature it was found that there was considerable plastic deformation of APP under the high pressure of the tip. Shown in Fig. 7.12 and Fig. 7.13 are force curves taken at room temperature. The curves are bumpy and in Fig. 7.13 there is large hysteresis in the repulsive contact region between approach and retraction, which is indicative of plastic deformation of the sample. This is even though a small load has been applied (small part c of the force curve)

In several cases jumps were observed during pull-off. This was followed by a large increase in the pull-off force in subsequent curves. As mentioned earlier the pull-off force varies linearly with the radius of the curvature of the tip. We have also confirmed the more or less linear relationship of the pull-off force by using tips of different radii in our measurements. If then while using the same tip at the same temperature, there is an abrupt increase in the pull-off force, which in some cases was almost greater by a factor or two or more, this indicates a large abrupt increase in the radius of the tip. This can be explained by the fact that the tip probably has picked up a piece of the polymer surface on retraction. This was seen often in our measurements with sharp tips,

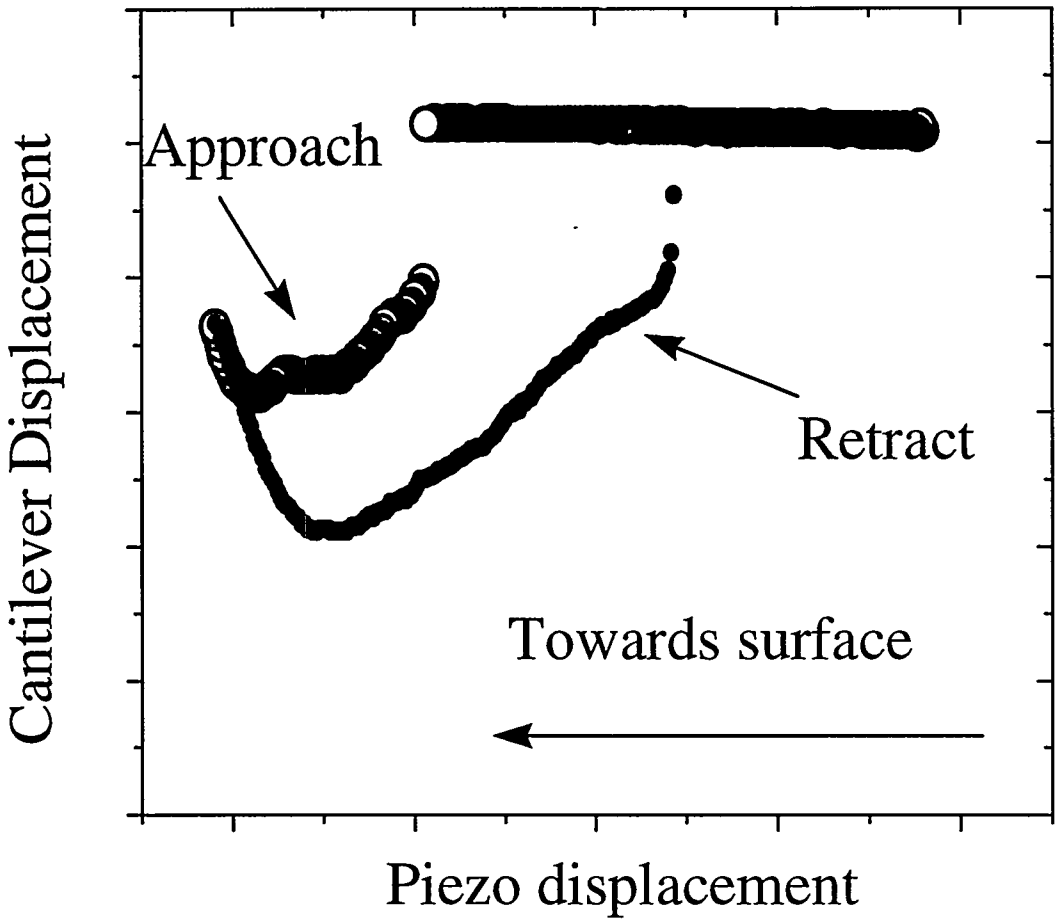

Figure 7.12 A force curve obtained with a 50 nm tip, force constant ~0.2 N/m showing large hysteresis in the attractive region on retraction even though very small loads have been applied.

and care must be taken to include this increase in the radius in any analysis of the data, since a change in the radius of the tip changes the contact properties of the tip and the surface. The plastic deformation of the polymer decreased at

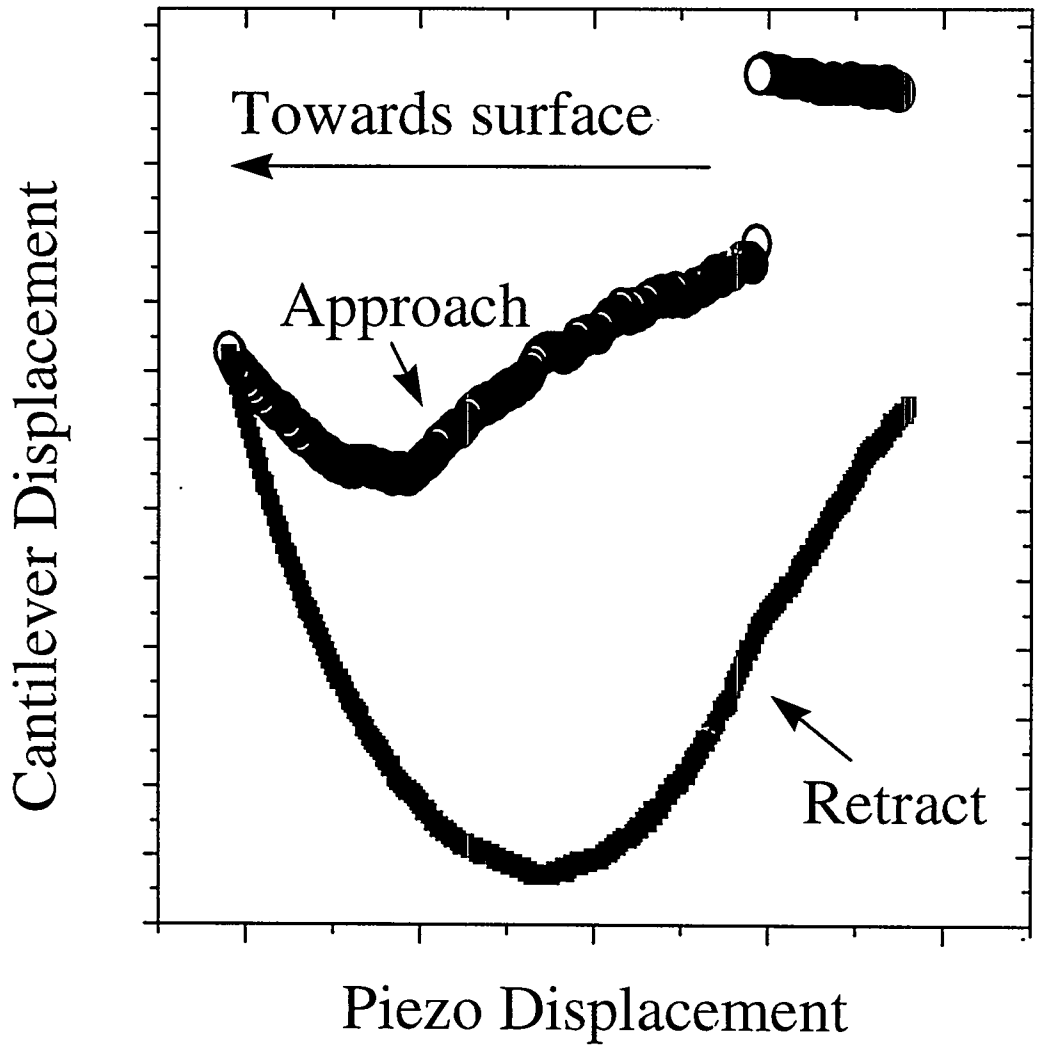

Figure 7.13 A force curve obtained with a 50 nm tip, force constant ~0.2 N/m showing large hysteresis in the attractive region and the repulsive region, which implies plastic deformation of the sample.

lower temperature and the curves became well behaved at these temperatures.

At each temperature, ~50-100 pull-off curves were measured on APP. Other than changes in the pull-off force due to changes in the radius of curvature of the tip, no significant changes in adhesion were measured on the polymer surface during the glass transition. Since the polymer consists of chemically similar CH_2 and CH_3 groups we expect that even though there may be a change in the orientation of these moieties on the surface, the effect of a change in surface energy is expected to be minimal and this may be an explanation for our not observing any significant change.

The main difference we observed in the curves as a function of temperature on the polymers was the slope of the curve (part c). We monitored the **initial slope** of the approach curve in the repulsive regime (part c of figure 7.4) on and used it as a signature of modulus changes in this temperature regime. Shown in Fig. 7.14 are the representative changes observed for APP during one such temperature run. The bars drawn in the figure represent the average standard deviation of the measurements. It can be seen that the slope of the approach curve or the modulus of the sample increases dramatically as the temperature is decreased. This is expected as the modulus of the polymer increases due to freezing of the chain motion. However the largest increase occurs at a temperature between 0 to 20 ^{0}C. This is higher by around 20 degrees compared to the SFG measurements and the bulk T_g temperature. This shift has been attributed to the high pressure under the SFM tip, as has been described in Chapter 4. The T_g temperature of polymers is known to increase

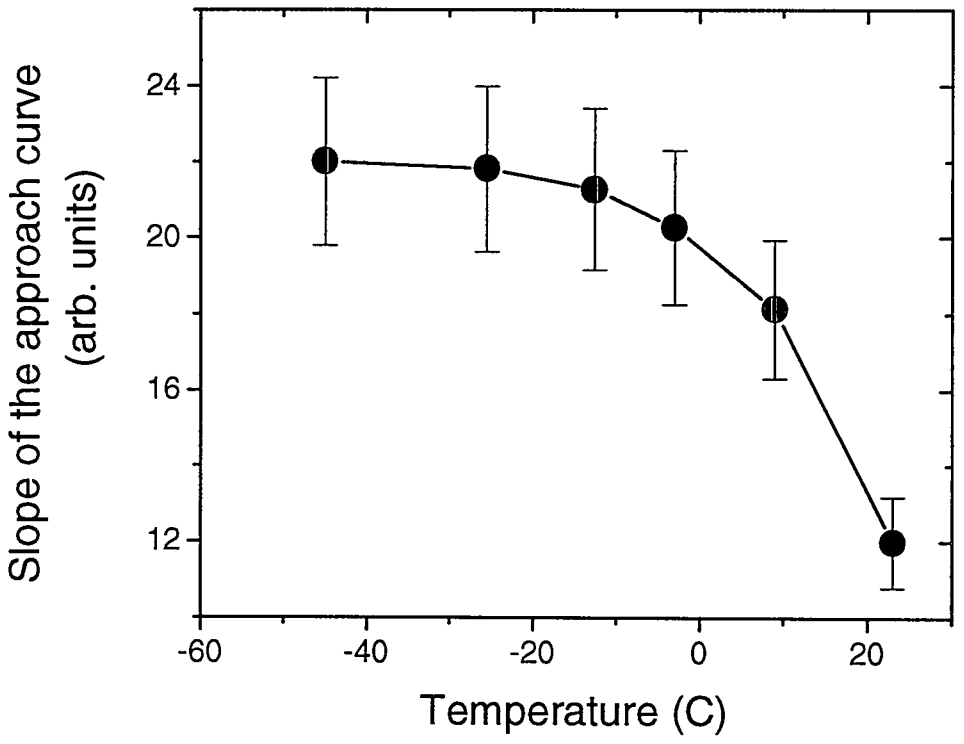

Figure 7.14 A plot of the initial slope of the approach curve vs temperature obtained on a temperature run on the surface of APP.

with increasing hydrostatic pressure[19]. The shifts of various relaxations observed in some polymers have been reported to be of the order 5-30 ^{0}C / 1000 atm. In our measurements the exact shift in the temperature varied in different runs and seemed to depend on the local structure of the polymer as expected. No such change could be conclusively detected in IPP, this is because the transition is not sharp in IPP and it is difficult to detect the exact temperature at which it occurs because of the statistical nature of the measurement.

Friction vs load Curves on APP revealed considerable plastic deformation at room temperature, however at lower temperatures the friction Vs load curves were well behaved and seemed to show characteristics of JKR contact (chapter 2 and 4) as shown in Fig. 7. 15. In this case the friction curves were characterized by a coefficient which was obtained by fitting a straight line to the

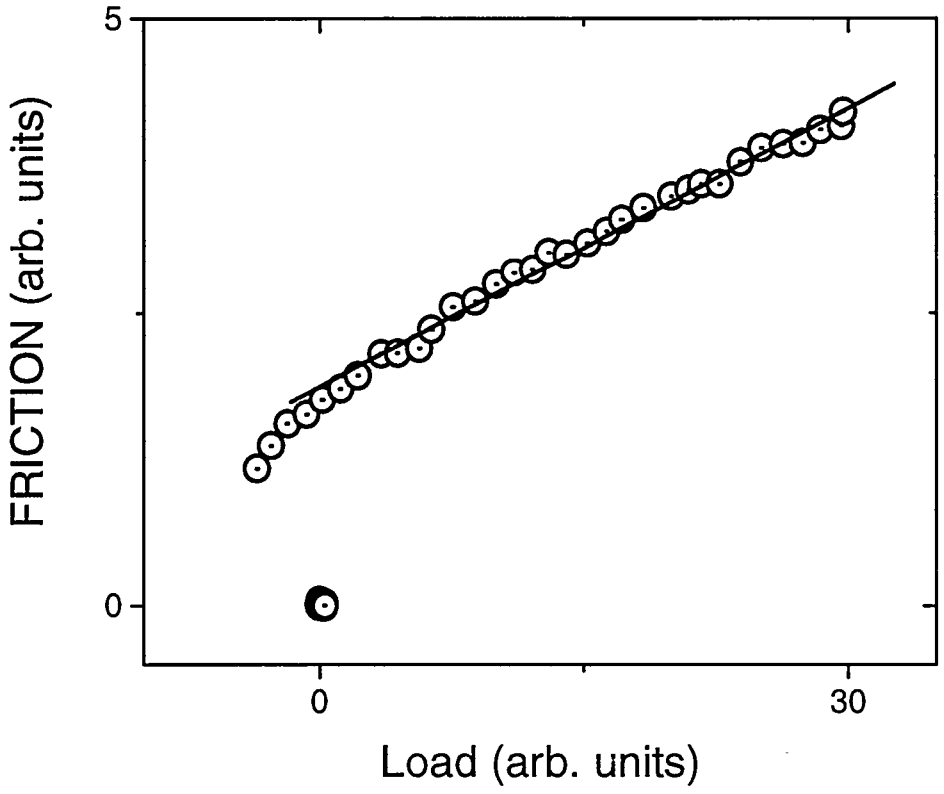

Figure 7.15 A well behaved friction vs load curve obtained on APP at low temperatures showing characteristics of JKR contact like friction at negative loads.

friction data at positive loads as shown in Figure 7.15. If we then plot this friction coefficients as a function of temperature we get Fig. 7.16. The friction

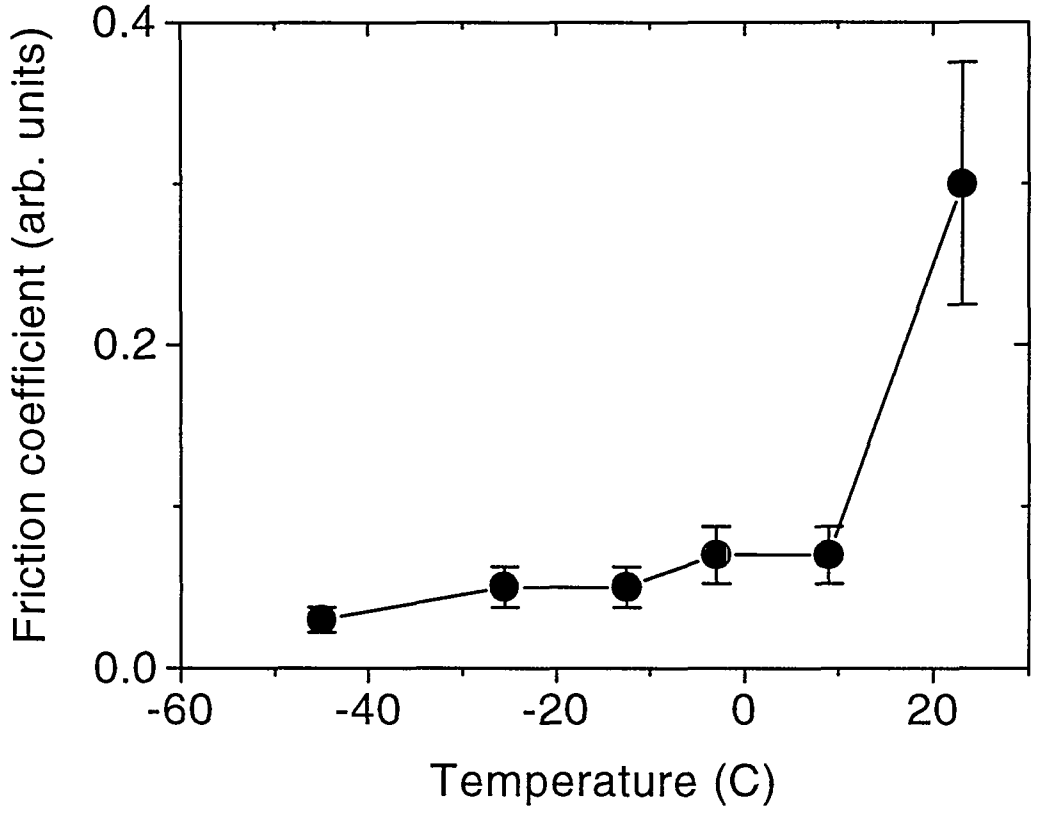

Figure 7. 16 Friction coefficients obtained by fitting a line to the positive part of the friction vs load curves (Fig. 7.15) plotted as a function of temperature.

coefficients decrease with decreasing temperature. This can be attributed to two effects:

1) Plastic deformation: At room temperature we have observed wear during friction. Wear is known to increase the friction coefficient on IPP[20], which is

what we could be seeing. At lower temperatures the wear during friction decreases drastically and this could explain the low friction coefficients measured in this temperature regime.

2) As discussed in Chapter 4., friction is assumed to be proportional to the contact area, as in the frictional force $F = \tau A$, where τ is the shear strength of the material and A is the contact area. Contact mechanics predicts that the contact area is approximately proportional to $E^{-2/3}$ where E is the elastic modulus of the material. Now τ and E are both expected to change during the glass transition. Since E is known to increase by orders of magnitude as seen in our measurements too, this could account for a low friction coefficients below the glass transition due to a decrease in contact area.

If the sharp decrease in friction coefficient just below room temperature can be inferred as a signature of the glass transition, then this occurs at a temperature which is shifted by around 20 ^{0}C towards higher temperature. This is further evidence for the high pressure under the SFM tip as discussed above.

7. 3. 4. SFM with Blunt tips: As discussed in the previous section, we have observed a shift in the glass transition of APP towards higher temperatures under the high pressure of the SFM tip. This together with previous work reported in chapter 4 prompted us to use tips with a large radius of curvature (1 micron). These tips are similar chemically to the sharper tips, the only difference being the large radius of curvature of the tips. We also believe we have single

asperity contact between the tip and the surface while using these tips. The reasons for this are listed below,

1) The pull-off force (discussed earlier) with the same surface scaled almost linearly with the radius of curvature of the tip. i.e. the pull-off force or adhesive force for a tip of radius of 1 micron was roughly twenty times that of a tip with a radius of curvature of 0.05 micron. This is a sign of single asperity contact.

2) The friction vs load curves were non-linear, and appeared to be JKR like. The JKR theory occurs in single asperity contact. In multiple asperity contact, in general linear friction vs load curves are expected[21].

Force curves were measured again on Si, IPP and APP. Si was used as a blank sample and no change was observed. This precludes a single layer of contaminant or water condensate on the surface in the vacuum chamber that may skew the entire results. Also we wished to check that there were no changes in the components of the instrument as a function of temperature. The main change observed again was in the slope of the curves on IPP and APP. Plotted in Figure 7. 17 are the representative changes on these samples. The reproducibility of the measurements was higher with blunt tips as opposed to sharp tips. This is because of the larger area of contact of the tip in each contact with the surface, thereby averaging over a larger distance during each measurement. As can be seen the changes are most dramatic in APP. This is because of the large amorphous content of the polymer. Also in our measurements we are most sensitive to changes in the modulus in the range of

0.1 GPa to 10 GPa. In IPP the changes are less dramatic due to its high degree of crystallinity. It should be noted that the modulus is related in a highly non

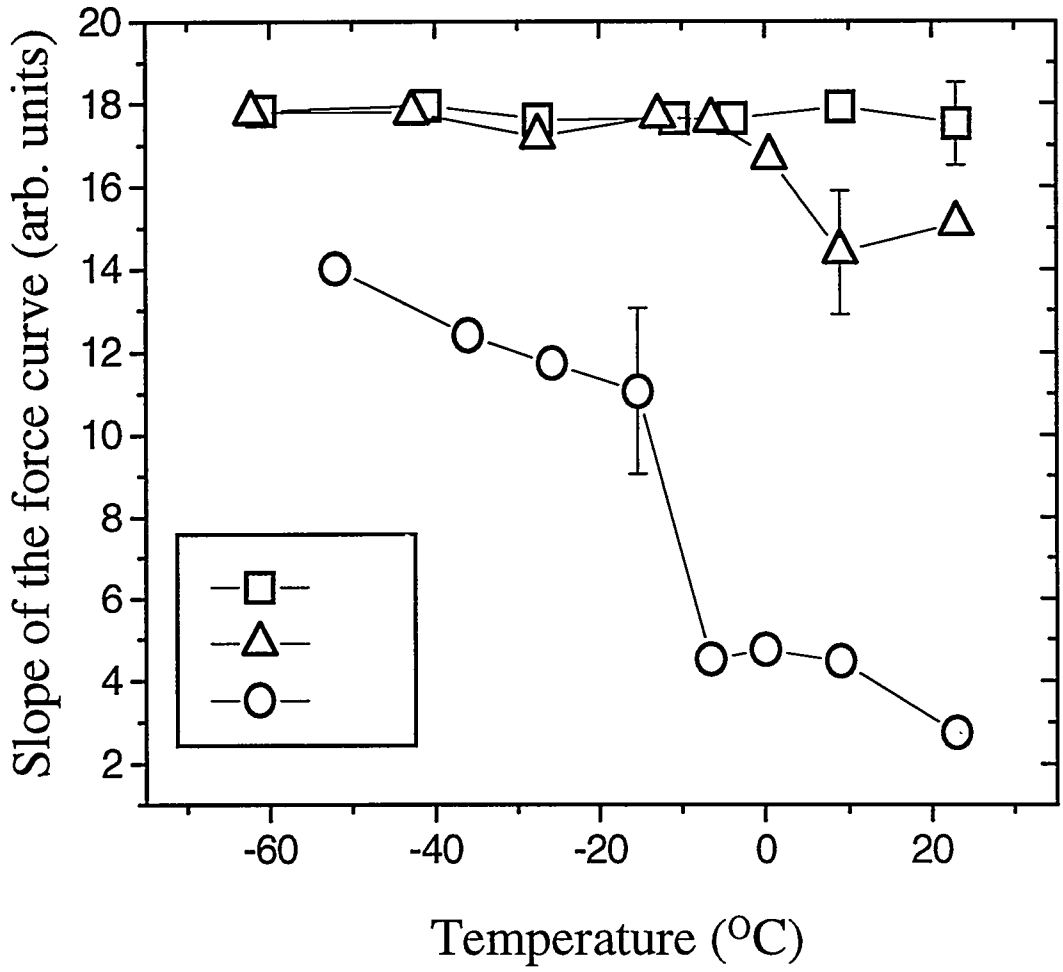

Figure 7. 17 A plot of the slope of the interaction curve (part c) vs temperature (^{0}C) for Si, IPP and APP.

linear manner to the slope of the interaction force curve. However the higher the slope the higher is the modulus. It can be seen that the major changes in the

slope occurs in the temperature region between 0 and -20 ^{0}C. This correlates well with the SFG results. In our measurements with blunt SFG tips (1 micron) and the loads we typically applied (1-10 nN) we could not detect any shift in the T_g temperature. In the SFG results we observed an enhanced ordering of the backbone of the polymer below the T_g, with the CH_2 groups pointing outward. Such an ordering of the surface could be responsible for the higher modulus measured on these surfaces with SFM.

7. 3. 5. Difference between bulk and surface T_g: Lastly in both SFG and SFM experiments we observe that there is no significant difference (> 20 ^{0}C) between the bulk and surface T_g temperature.

This could be because of the high molecular weight of the samples used e.g. for IPP 250 K.

For amorphous polymers in the bulk[10], the depression in T_g with molecular weight for the bulk and the surface as a function of N the number of statsitical segments of length a in a chain are,

$$\Delta T_g = \frac{C}{N} \quad \text{for the bulk}$$

and

$$\Delta T_g = \frac{C}{N^{1/2}}\left(\frac{a}{d}\right) \text{ for the surface,}$$

where C is a constant, and d is the distance of the surface layer. Hence it can be seen that as N increases, the difference between the bulk and the surface T_g decreases. For example for polystyrene, C=1.1 x 10^3, Mol wt. of a monomer

=104, hence for a molecular weight similar to that used for IPP in our case i.e. 250 x10^3 , N ~ 2404, the difference between the surface and bulk for $a \sim d$ is then expected to be $\Delta T_g = \frac{C}{N^{1/2}}\left(\frac{a}{d}\right)$ i.e. = 22 K.

For PP with a lower monomer Mol. Wt. of 42 (higher N) we expect this change to be even smaller.

The entanglement molecular weight of polypropylene is low ~ 4 K[22]. Above this molecular weight the chains get entangled with each other, accompanied by a large rise in viscosity of the polymer. These entanglements could resist the migration of end groups to the polymer surface.

It should also be noted that the thickness of our films (100 -500 microns) precludes thin film confinement effects i.e. the polymer chains are confined between the substrate and the vacuum or air above it. This is because the thickness of the film is larger than the end to end distance of the polymer chain. In the future it would be insightful to repeat the same kinds of experiments with low molecular weight thin films of polymers to directly measure any shifts in the T_g of the polymers due to surface effects.

7. 4. Conclusions: In this chapter a unique, new way of determining the glass transition of a polymer surface was demonstrated with SFG and SFM. The results correlate well in both independent experiments. The enhanced ordering of the chains could provide a molecular level understanding for the macroscopic increase of the mechanical modulus of the polymer. Finally it is importance to work with blunt tips while doing measurements on a surface where spatial

resolution in the plane is of secondary importance. In this way reproducible measurements may be performed at low pressures.

Chapter 7. References:

[1] M.G. Cowie, *Polymers: Chemistry and Physics of Mordern Materials* (Intext Educational, New York, 1973).

[2] T. Murayama, *Dynamic Mechanical Analysis of Polymeric Materials* (Elsevier Scientific, Amsertdam, 1978)

[3] J. D. Ferry, *Viscoelastic Properties of Polymers* (John Wiley, New York, 1970).

[4] S. Matsuoka, *Relaxation Phenomena in Polymers* (Carl Hanser Verlag, New York, 1992).

[5]G. B. DeMaggio, W.E. Frieze, D. W. Gidley, Ming Zhu, H. A. Hristov and A. F. Yee, Phys. Rev. Lett. **78**, 1524 (1997).

[6] J. L. Keddie, R.A.L.Jones and R.A. Cory, Europhys. Lett. **21**, 59 (1994).

[7] B. Frank, A.P. Gast, T.P. Russell, H.R. Brown and C. Hawker, Macromolecules **29**, 6531 (1996).

[8] G.F. Meyers, B. M. DeKoven, and J.T. Seitz, Langmuir **8,** 2330 (1992).

[9] T. Kajiyama, K. Tanaka, and A. Takahara, Macromolecules **30**, 280 (1997).

[10] A. Mayes, Macromolecules **27**, 3114, (1994).

[11] Y.R. Shen, Nature **337**, 519 (1988).

[12] G. Binnig, C.F. Quate, and C. Gerber, Phys. Rev. Lett. **56,** 930 (1986).

[13] B. Bogdanov, M.Michailov: Properties of Polyolefins in *Handbook of Polyolefins* ed. C.Vasile, R. Seymour (Marcel Dekker, New York, 1993) page 314.

[14] J. van Schooten, H. van Hoorn and J. Boerma, Polymer **2,** 161 (1961).

[15] F. A. Bovey, *High Resolution NMR of Macromolecules* (Academic Press, New York, 1972)

[16] NT-MDT Co., Moscow, Russia.

[17] D. Zhang, Y.R. Shen and G. A. Somorjai, Chemical Physics Letters **281**, 394 (1997).

[18] C. D. Bain, P. B. Davies, T. Hui Ong, R. N. Ward and M. A. Brown, Langmuir **7**, 1563 (1991)

[19] E. Jones Parry and D. Tabor, Polymer **14**, 615 (1973)

[20] D. H. Gracias and G. A. Somorjai, Macromolecules **31**, 1269 (1998)

[21] Greenwood and Williamson (1966)

[22] L. J. Fetters, D. J. Lohse and R. H. Colby in *Physical Properties of Polymers Handbook* ed. J. E. Mark (AIP, N.Y. 1996)

8. Surface Studies of Polymer Blends by Sum Frequency Vibrational Spectroscopy, Atomic Force Microscopy and Contact Angle Goniometry.

8.1 Introduction: Polymer blends are widely used as a means of tailoring the bulk and the surface properties of polymeric materials for various industrial and biomedical applications[1-2]. They are of fundamental importance in relation to interfacial phenomena of macromolecular systems and of technological interest associated with wetting, adhesion and tribology. A unique feature of these systems is that the surface composition and structure, and consequently the surface properties of the material are often different from that of the bulk. This is due to a surface enrichment of the component that will minimize the total surface energy of the system[3]. The challenging problem however is to characterize the surface composition and structure of such polymer blends, so as to obtain the true surface structure-property relationship, and a molecular understanding of the interfacial behavior of such macromolecular mixtures.

In this study a combination of three techniques was used to gain a detailed understanding of the surfaces of a two component polymer blend as a function of bulk concentration of the blend. A conventional technique, " Contact angle Goniometry" was used to measure the contact angle or the surface tension of the blend surfaces. In addition a combination of new techniques SFG and SFM was used to measure the surface chemical composition and the topography of the blend surfaces.

Polyurethane capped with SME

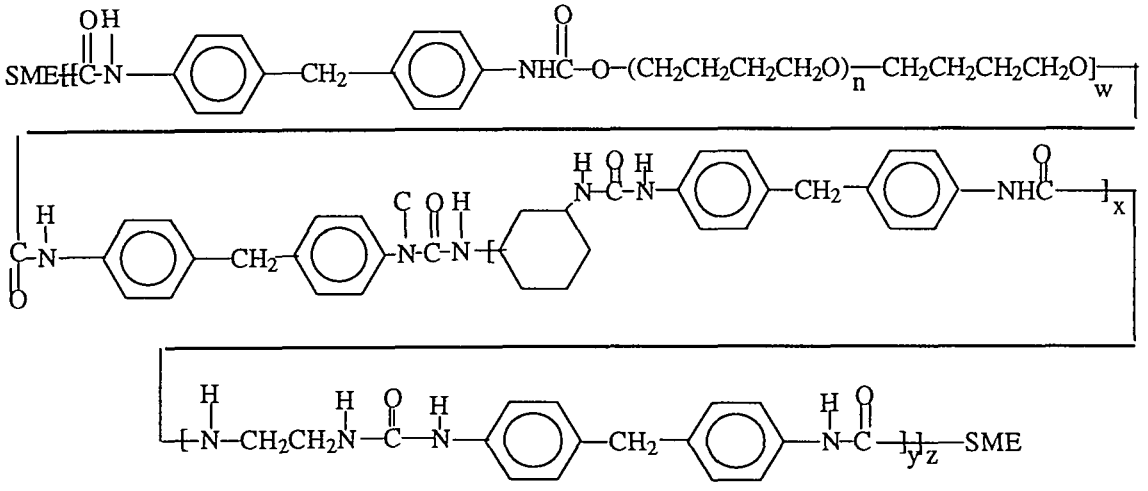

SME = Surface Modifying End group

SME in BS is PDMS i.e.

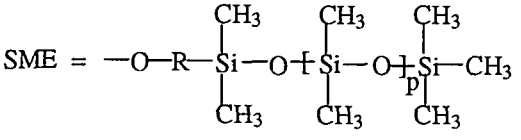

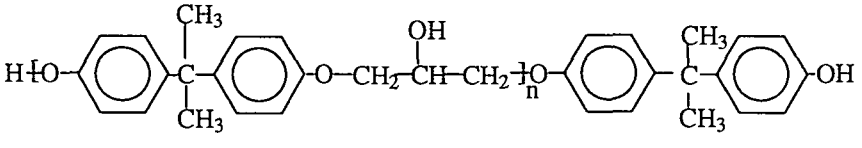

Base Polymer (BP)

Figure 8.1: Structure of the component Biospan-S (BS) i.e. a polyurethane capped with PolyDimethyl Siloxane as a Surface Modifying End group, and the component BP (phenoxy). The two components are mixed to form the blend.

The polymer blend chosen in our study is composed of two thermodynamically compatible components which are miscible in the bulk, Biospan-S (BS) and the phenoxy base polymer (BP). The molecular structures of BS and BP are shown in Fig. 8.1. BS is a polyurethane capped with poly(dimethylsiloxane) (PDMS) end groups. As seen from its chemical structure, BS contains both more hydrophobic (PDMS), and more hydrophilic (ether and urethane segments) components. Such blends of phenoxy with several different block or segmented copolymers can produce extrudable and moldable compounds which soften at (a glass transition) temperature that can be varied via the composition of the blend. The dramatic difference in stress relaxation rate above and below glass transition give these blends shape-memory properties. Such blends, with a glass transition between room temperature and the body temperature e.g. 35°C are thus ideal candidates for various biopolymer applications such as intravenous catheter tubings, which will soften after insertion into the veins. Since the surfaces of these blends are in contact with blood after insertion, the surface properties are of great interest in preventing complications related to thrombosis and embolization caused when blood contacts a foreign surface. From a previous study[4], it was found that the more hydrophobic PDMS tails dominate at the pure BS polymer surface, yielding a water contact angle of 94°. Such a siliconization of surfaces is known to extend blood clotting time and reduce blood platelet adsorption and thrombosis in vivo. However the other component, pure BP, is more hydrophilic and has a water contact angle of 74. We are interested in probing the different surface properties

(surface chemical composition, surface structure and surface free energy) while varying the blending ratio, and studying the correlation among them.

8. 2. Experimental.

8. 2. 1. Samples: The BS polymer (MW = 65000) was synthesized by The Polymer Technology Group, Inc., of Berkeley, California[5]. The homopolymer of BP (MW = 16000) was purchased from Union Carbide. Polymer films of different blend composition were prepared by casting the polymer blends from their N, N-Dimethylacetamide (~1% wt of the polymer) solutions onto flat quartz substrates. Then the films were dried in air at 65 °C for 24 hours. The film thickness was measured by an Alpha-Step 50V Surface Profiler after it was cooled to room temperature. The thickness of these films was in the range of 100 micron.

8. 2. 2 SFG: The SFG set up is described in Chapter 3. In this work, we present only results with the polarization combination of ssp (for s-polarized SF output, s-polarized visible input, and p-polarized infrared input).

8. 2. 3 Scanning Force Microscopy: The SFM used for imaging was a commercial Park Scientific M5 instrument. All imaging and friction measurements were done in the contact mode with Park Scientific silicon contact ultralevers of force constant ~ 0.1 N/m and loads between 10 and 20 nN.

8. 2. 4 Contact Angle Goniometry: A Rame-Hart NRL Contact Angle Goniometer was employed to measure the contact angle of liquids with known

surface tension on polymer films, using the sessile drop technique[6]. The liquids used in this study are water (72.8 dyne/cm) and methylene iodide (50.8 dyne/cm). The contact angle was measured directly using the movable protractor scale of the goniometer. The geometric-mean method[7] was used to deduce the surface free energy of the polymer films from the contact angles of two different liquids, water and methylene iodide.

8. 3 Results and Discussion:

8. 3. 1 SFG spectra of pure components: Figure 8. 2 shows SFG spectra of pure BS and pure BP in air at 300 K in the C-H stretching region. In the BP spectrum, a pronounced peak at 2875 cm^{-1} was observed and assigned to the symmetric stretch of the methyl group. The other two weak features at 2926 and 2943 cm^{-1} are attributed to the antisymmetric stretch and the Fermi resonance band of the CH_2 groups, respectively. In the latter analysis, the symmetric stretch of CH_3 at 2875 cm^{-1} is taken as the characteristic band for BP. The contact angle of pure BP is 74°, indicating that it is a polymer of high surface energy. The SFG spectrum of BS is very different from that of BP. Three prominent peaks are present. According to a previous study[4], we can assign the peaks at 2919 and 2963 cm^{-1} to the symmetric (r^+) and antisymmetric (r^-) stretches of the CH_3 groups of PDMS, respectively, and the one at 2854 cm^{-1} to the symmetric stretch of the CH_2 groups of biospan. The strong PDMS modes in the SFG spectrum suggest that the BS surface is well populated by PDMS,

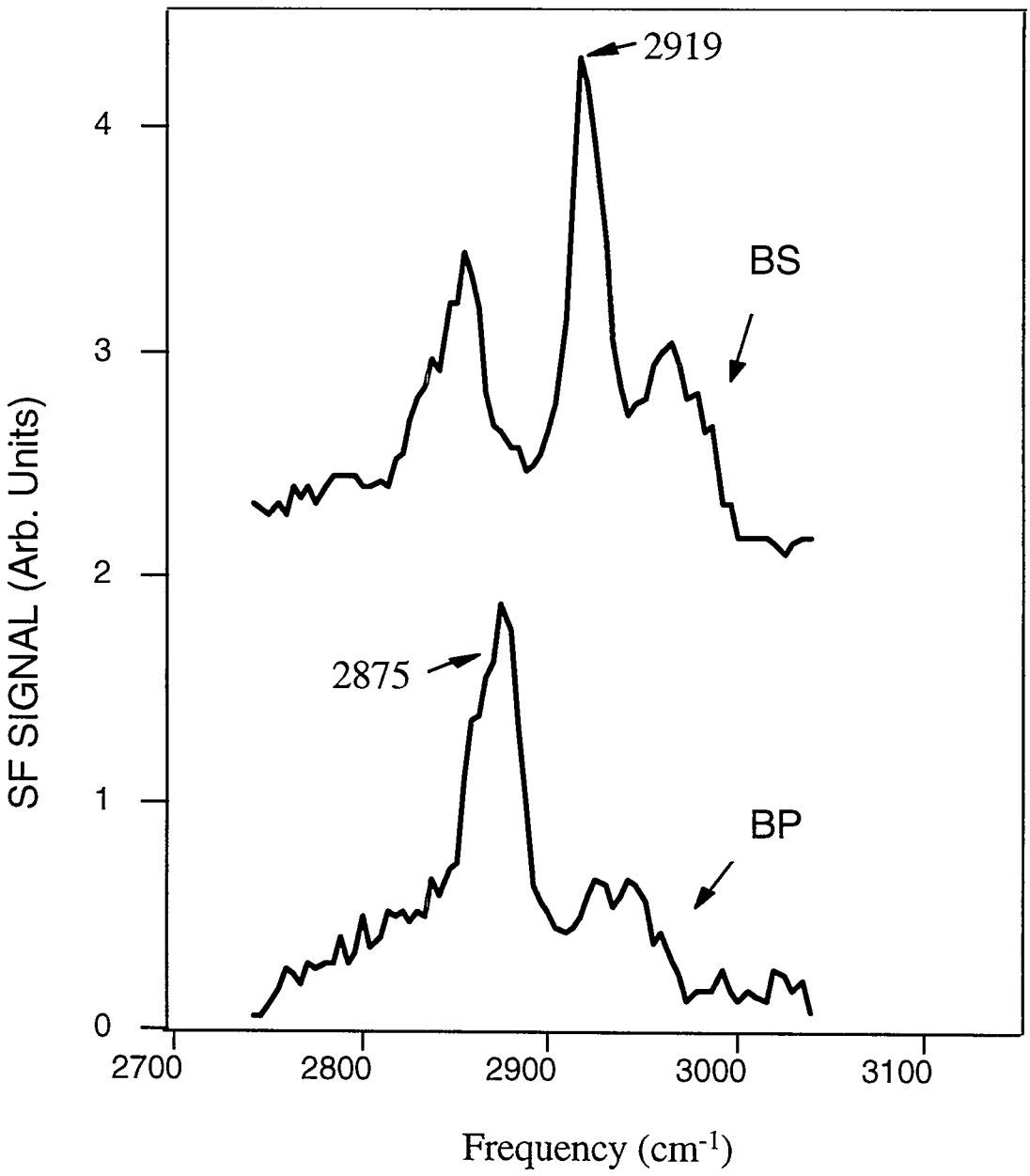

Figure 8.2 SFG spectra of pure BS and BP, the peaks at 2919 cm^{-1} and 2875 cm^{-1} will be used as signature peaks for the two components BS and BP respectively.

yielding a hydrophobic surface with a water contact angle of 94°.

8. 3. 2 SFG spectra of the blend as a function of bulk concentration of the components: The SFG spectrum of BP changed significantly when BS was added to BP. Figure 8.3 shows the SFG spectra of BS/BP blends of various blending ratios. The key features of the observed spectral changes with increasing BS bulk concentration are the weakening of the prominent methyl resonance of BP at 2875 cm^{-1}, and the strengthening of the prominent 2919 cm^{-1} band for the CH_3 groups of BS. These changes clearly show an enrichment of the BS component at the polymer blend surfaces. Because BS is more hydrophobic, it tends to segregate at the polymer surface to lower the surface energy. From these SFG spectra we can measure the square roots of intensity ratios of the 2875 cm^{-1} peak versus the 2919 cm^{-1} peak. The former is the characteristic peak of BP and the latter is that of BS. Since the square root of the SFG intensity of a peak is proportional to the number of chromophores at the surface[8] contributing to the peak, the intensity ratio can be used as a measure of the relative surface concentration of the two components assuming that there is no orientational change. Thus the SFG results presented in Fig. 8.3 can be used to quantify the relative BP content at the polymer blend surface. These results are plotted in Fig. 8.4, along with contact angle results which will be discussed in the next section. As we can see, the concentration of BS on the surface increases dramatically with an increase in the BS bulk concentration and seems to saturate the surface at concentrations as low as 1.7 wt. %.

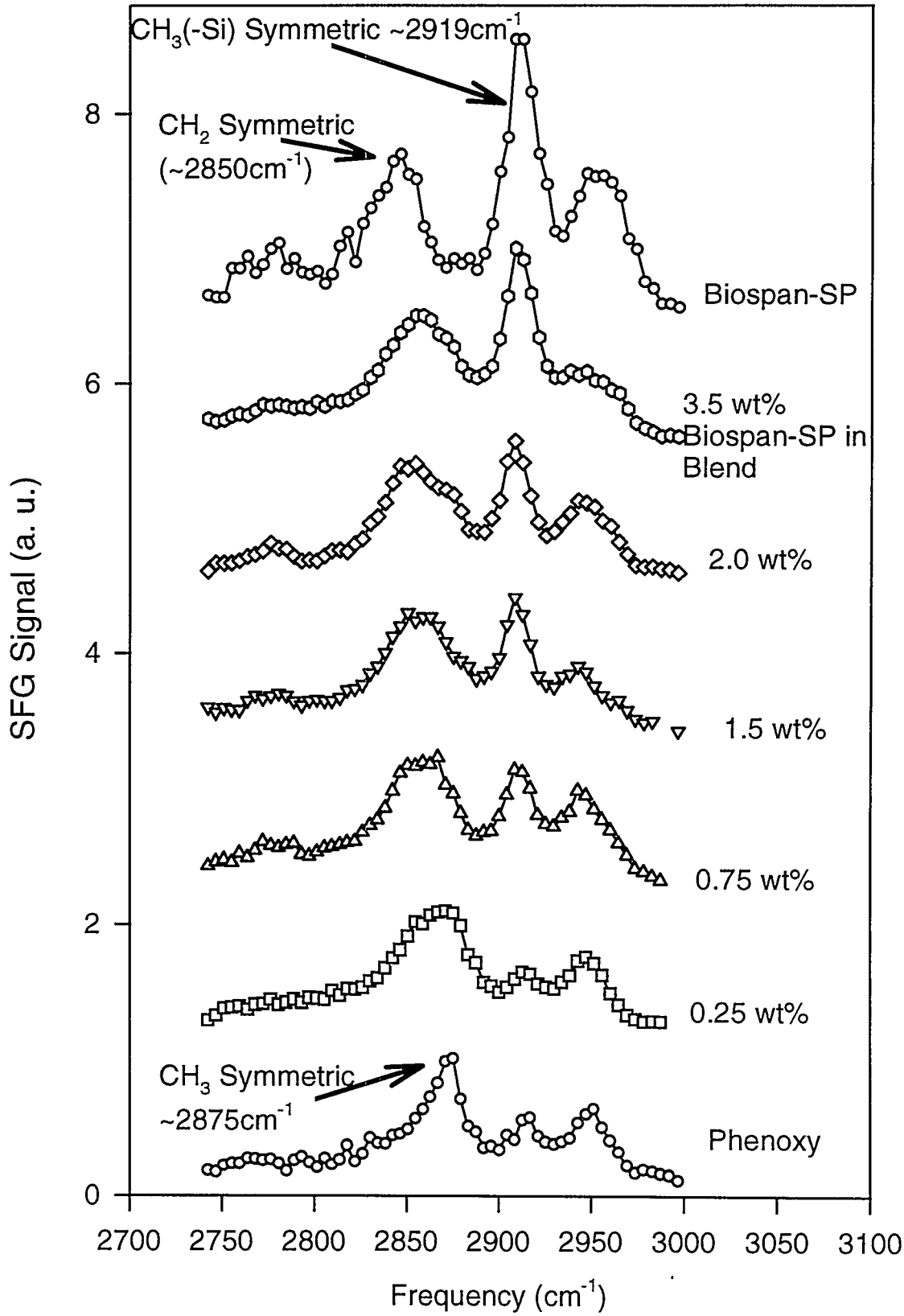

Figure 8.3 SFG spectra of the blends as a function of concentration.

8. 3. 3 Contact angle measurements: To obtain the surface free energies of polymer blends, we have performed contact angle measurements of water and methylene iodide on the polymer blend surfaces. The following 'geometric mean equations'[7],were then used to calculate the solid surface tension for each sample from contact angles.

$$(1 + \cos q_w)\, g_w = 2[(g_w^d\, g_s^d)^{1/2} + (g_w^p\, g_s^p)^{1/2}] \qquad (1)$$

$$(1 + \cos q_m)\, g_m = 2[(g_m^d\, g_s^d)^{1/2} + (g_m^p\, g_s^p)^{1/2}] \qquad (2)$$

where q_w and q_m are the contact angles of water and methylene iodide on the sample respectively, g_w, g_m, and g_s are the surface tension of water, methylene iodide, and the sample, respectively, and the superscripts d and p denote the dispersive (nonpolar) and polar components of the surface tensions. By measuring q_w and q_m, and inserting known values[7] for g_w^p, g_w^d, g_m^p and g_m^d, the solution of the two equations yields g_s^p and g_s^d. The solid surface tension or surface energy is given by $(g_s^d + g_s^p)$.

Fig. 8.4 presents the results on surface tension for the polymer blend surfaces as functions of BS bulk concentration. The surface tension of pure BP and BS are 44.9 and 22.2 dynes/cm, respectively. When the BS bulk concentration is lower than 0.17 wt%, the surface tension of the BS/BP blend is very close to that of pure BP and when the BS concentration is higher than 1.7 wt%, it approaches that of pure BS. In the intermediate region of 0.17 -1.7 wt% of BS, the surface tension of the blend decreases almost linearly with increasing BS concentration.

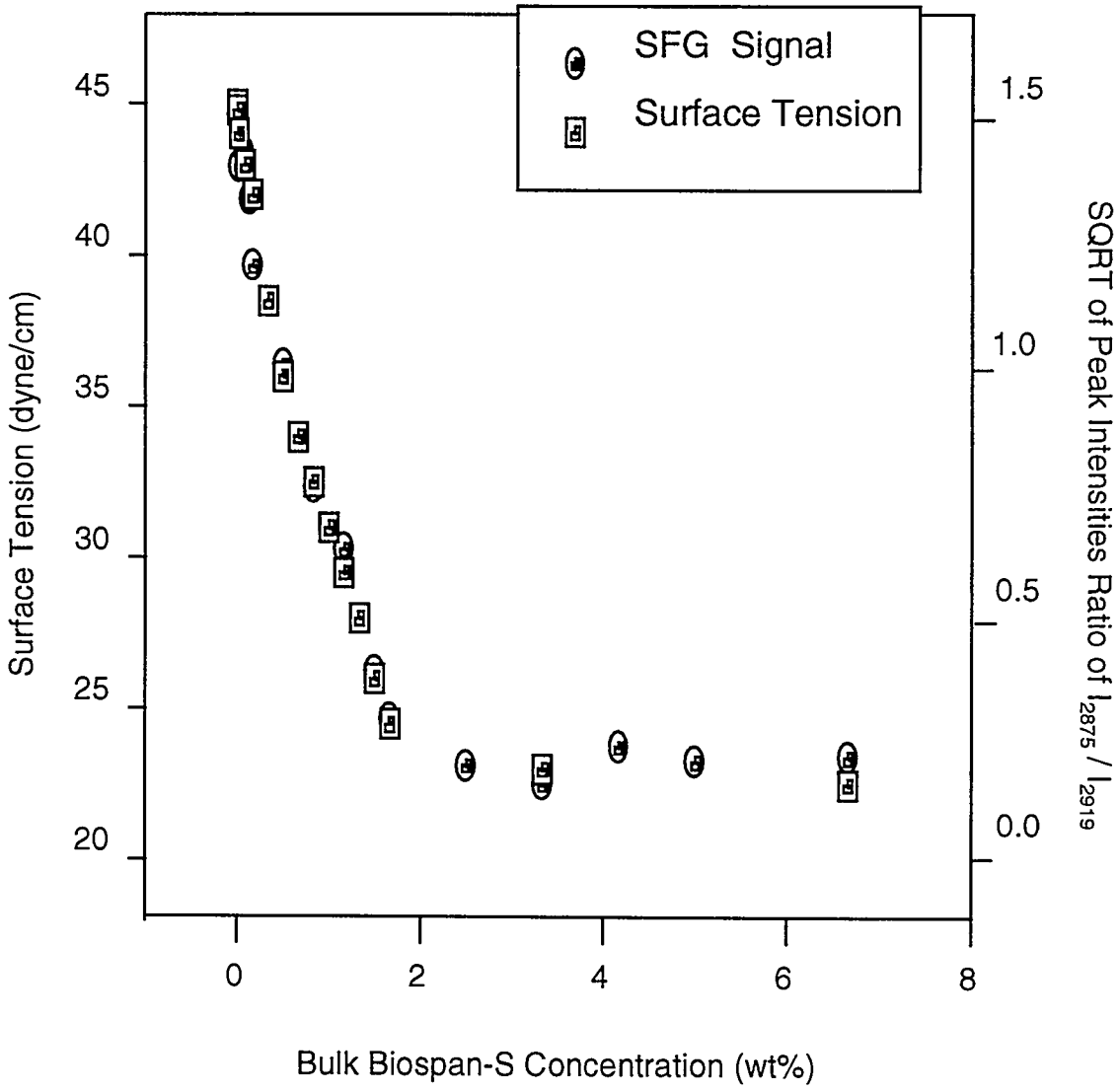

Figure 8.4 Square root of SFG peak intensity ratios and surface tensions as a function of BS bulk concentration. As can be seen the surface is saturated with BS at a bulk concentration of ~1.7 wt. %. At this concentration, the surface tension also dramatically decreases.

8. 3. 4 Comparison between SFG and contact angle measurements. Non-ideal behavior: As seen in fig. 8.4 , the change of surface tension correlates well with the relative BP surface composition measured by SFG. The result clearly shows the surface enrichment of the low surface-energy component (BS) in order to minimize the overall surface free energy of the binary macromolecular system. This interfacial behavior of adsorption of BS at the polymer blend surface is very similar to what has been universally observed for binary liquid mixtures of small organic molecules[9]. However, it should be noted that the changes of the surface tension (g), as a function of the concentration (C), of the lower surface energy component, are different for polymer blends and liquid mixtures. The usual analysis of such a function of a binary liquid mixture uses the Gibbs equation[10]. In a typical g -log C plot, the slope of the curve remains essentially unchanged in a given region where the surface tension keeps changing, indicating that the surface concentration of the surface active component reaches a constant maximum value at the liquid surface. However, in our study, as shown in Fig. 8.5, both the surface composition and the surface tension change simultaneously with the BS bulk concentration in the region of 0.17 to 1.7 wt%. Then both of them reach the constant value when the BS bulk concentration is 1.7 wt%. This different behavior between the polymer blend and the liquid mixture will be discussed further later on.

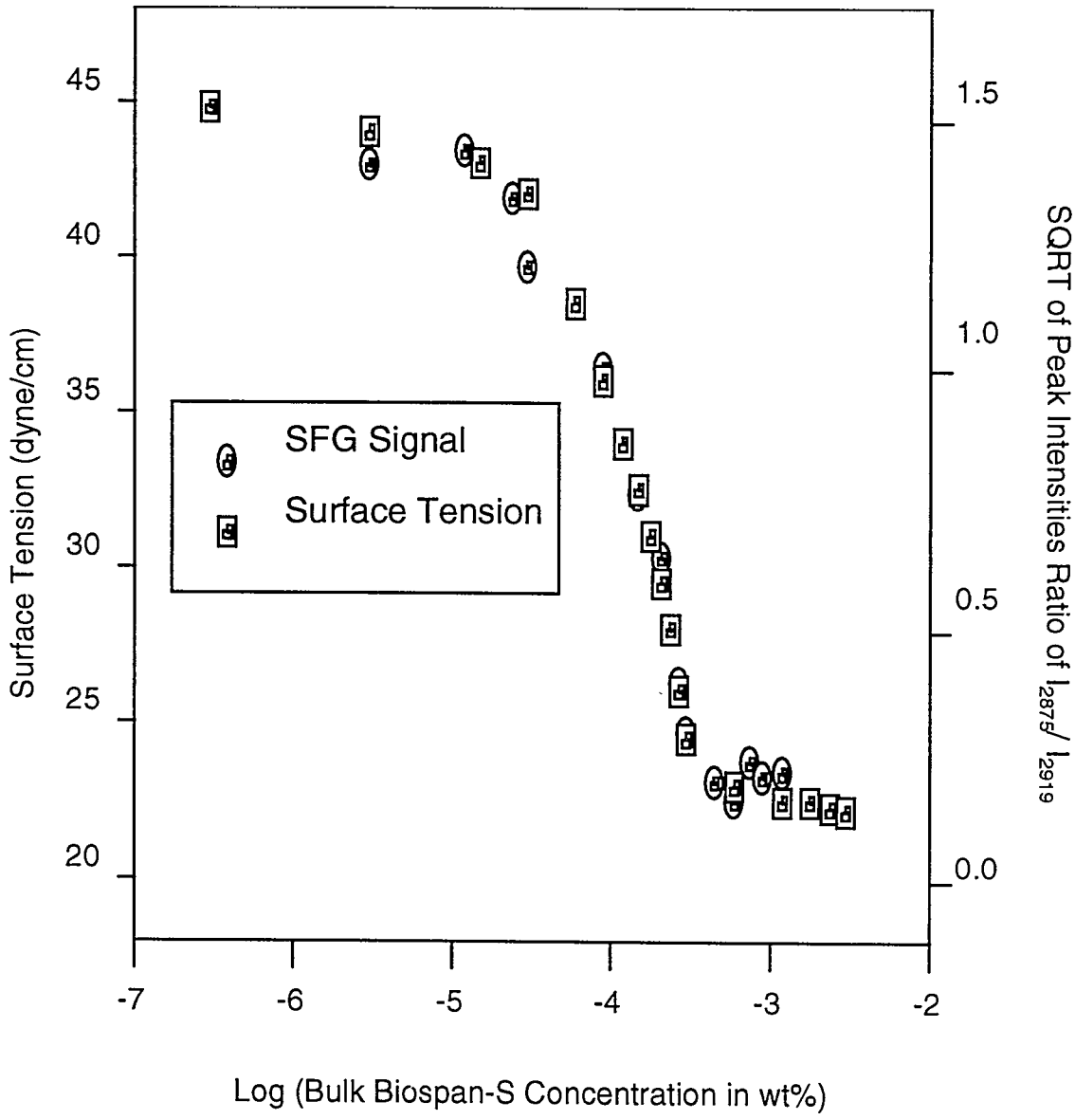

Figure 8.5 Square root of SFG peak intensity ratios and surface tensions as a function of log BS bulk concentration. As can be seen the surface concentration changes, when Gibbs behavior predicts a constant value.

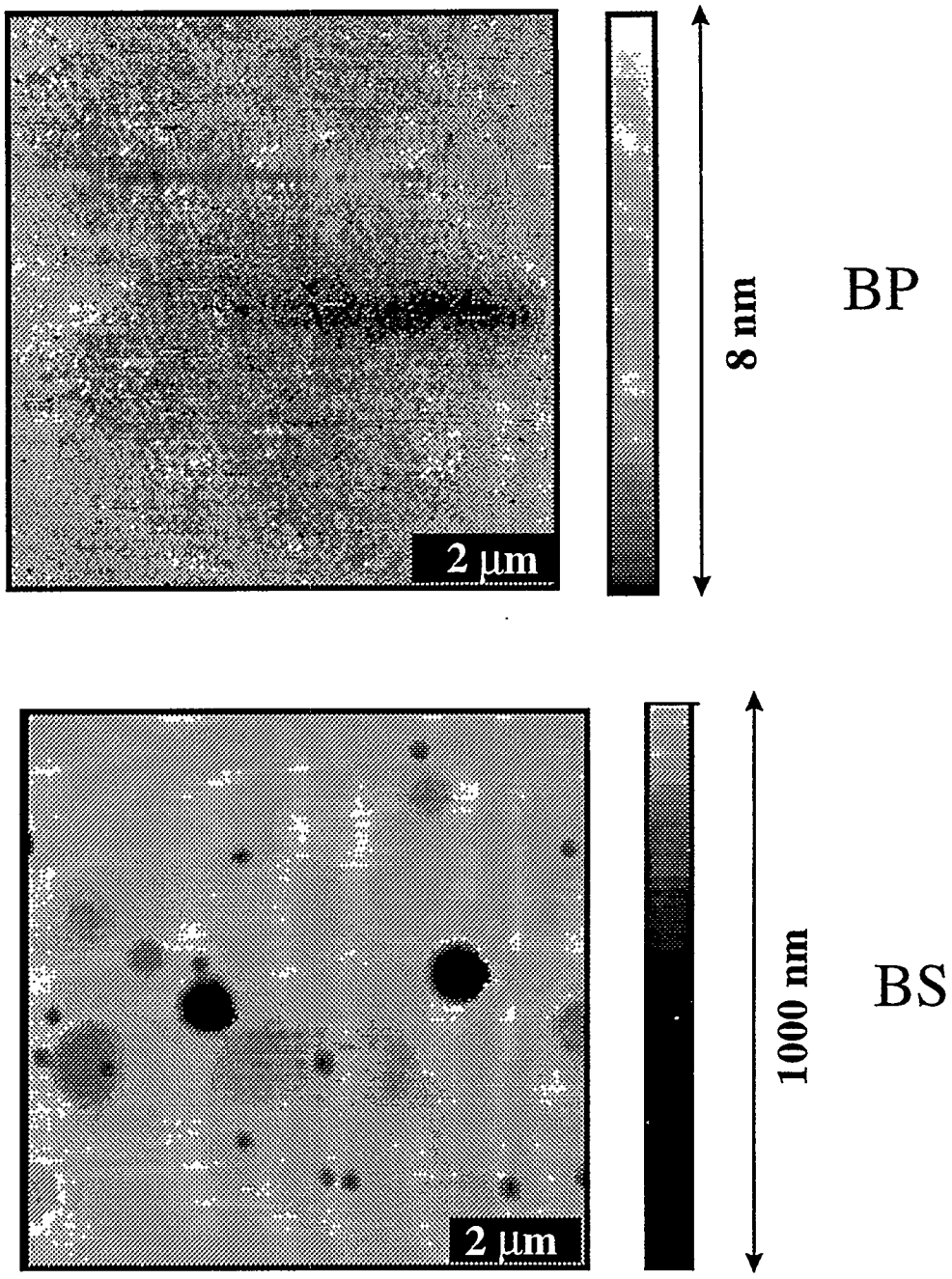

Figure 8.6 Topographic SFM images of pure BP and pure BS obtained in the contact mode

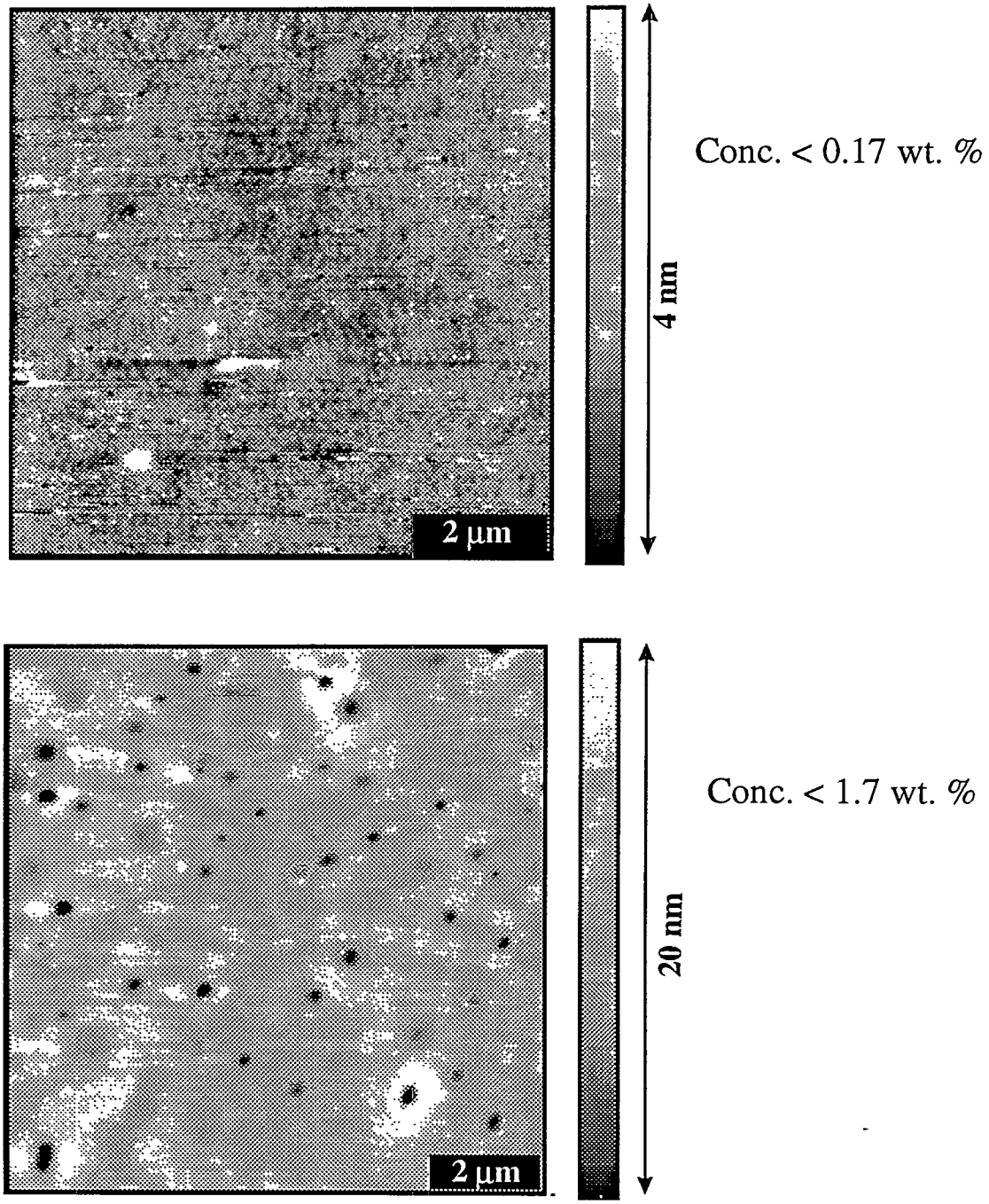

Figure 8.7 Topographic SFM images of the blend surface at concentrations of BS < 0.17 wt. % and > 1.7 wt. % resembling that of pure BP and pure BS resp.

8. 3. 5 SFM images of pure BS and BP: The SFM images of the morphology of pure BP and BS are shown in Fig. 8.6. The surface of BP is featureless with an r.m.s. roughness of ~ 5 nm. The BS surface contains large holes. These holes range from 100 nm to 500 nm wide and 20 nm to 1 micron deep and are observed all over the surface. The reason for the hole formation is not clear but could result from solvent evaporation from the cast film during sample preparation.

8. 3. 6 SFM images of the blend as a function of bulk concentration of the components: The topographic images of the blend surface change as the bulk concentration is varied. For BS concentrations lower than 0.17 wt%, (Fig. 8.7 (a)), the surface appears featureless and resembles that of pure BP (fig 8.6 (a)). This correlates well with the SFG result which shows that the blend surface consists mainly of BP in this concentration regime. Fig. 8.7 (b) is an image obtained at concentrations higher than 1.7 wt% and consists of holes. This is similar to the surface of pure BS (figure 8. 6 (b)) and is consistent with the presence of BS at the surface of the blend at these concentrations as observed by SFG.

What is perhaps more interesting are the AFM images of blend surfaces for BS bulk concentrations in the range of 0.17-1.7 wt%. As shown in fig. 8.8 and 8.9, they exhibit a domain structure, very similar to the patterns observed in other phase segregated macromolecular systems[11]. The average height of the ridges is around 4 nm, which is equivalent to stacking of only a few molecules.

The pattern appears to be very stable, it remains after a period of three months without any discernible change. It is of course interesting to know the composition of the ridges and the base. This we hoped to achieve by measuring the surface friction with the AFM. As references, we first measured and found the friction of pure BP to be higher than that of pure BS by a factor of two, at a load of 20nN. The higher friction on BP at these small loads can be explained by the higher surface energy of BP as compared to that of BS. This results in a larger contact area between the AFM tip and the surface[12], which increases the friction[13]. We then measured the frictional force on the segregated surface (0.17-1.7%) while simultaneously imaging the surfaces at a load of 20nN using the same tip and the same instrumental set-up. The friction image of the blend is shown in figure 8.9 (c). The images plotted are difference friction images. i.e. the difference in the friction signal for right and left scans. This is done to remove any artifacts that might be introduced by topography. As can be seen from the image, the friction on the ridges is higher than that of the base, and we can thus conclude that the ridges are rich in the BP component of the blend. We attribute these domains to the preferential segregation of the BS component to the surface. In doing so, the BP component gets displaced at the surface and forms the ridges. From the shape of these patterns one can conclude that the segregation is isotropic in the plane of the surface, since the polygons show no preferential orientation. The dramatically different morphologies are responsible for the large changes, at the blend surface, in this concentration regime, as indicated by the SFG and surface tension data.

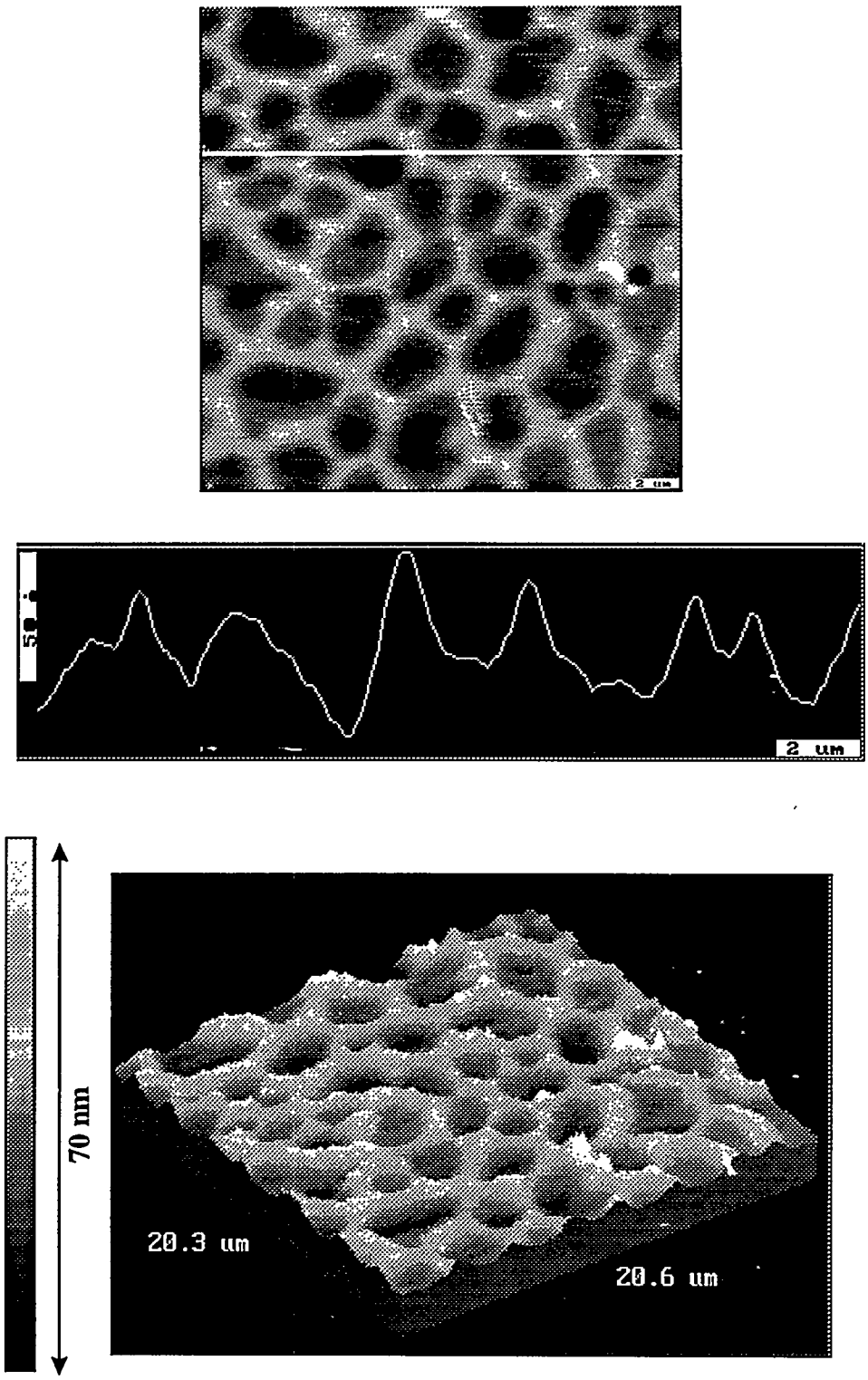

Figure 8.8 Topographic images of the segregated blend surface.

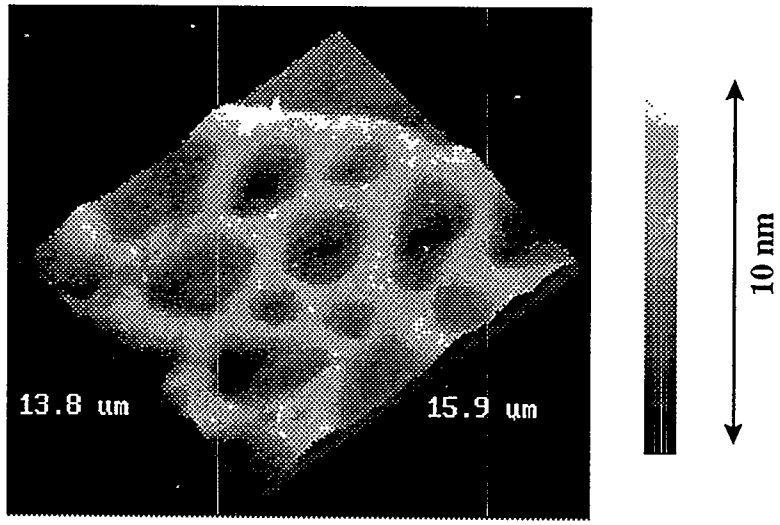

Topography

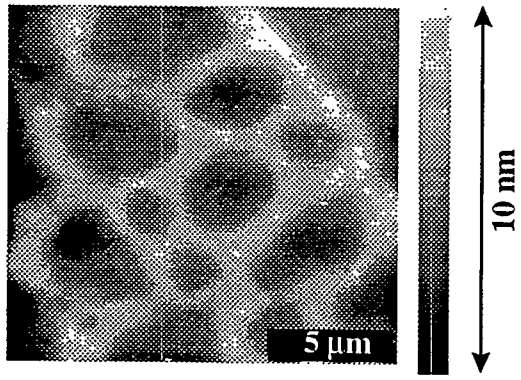

Friction

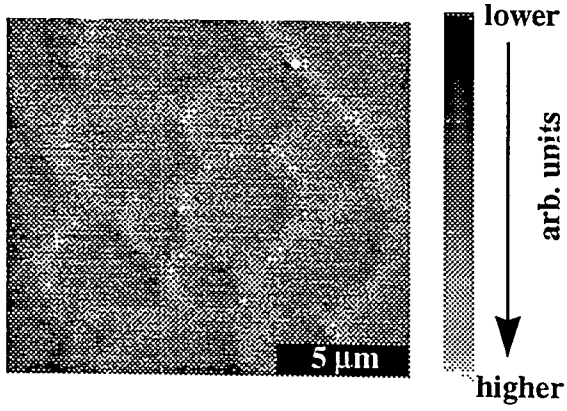

Figure 8.9 Topographic and friction images of the segregated blend surface.

8.4 Conclusions: In this chapter a combination of SFG and SFM was used yet again, this time along with contact angle measurements to study the surfaces of a two component miscible polymer blend[14]. As expected the surface structure of the polymer blend is very different from the bulk. The lower surface energy component is detected on the blend surface at bulk concentrations as low as 0.17 wt%. It increases with the bulk concentration and saturates the surface at a bulk concentration of 1.7 wt%. In the transition concentration regime between 0.17 and 1.7 wt. % , non-ideal behavior is observed as both the surface tension and the surface concentration of the components change. One explanation could lie in the fact that the miscible blends segregate or become immiscible on the surface in this concentration regime as is seen in the SFM images. Such a segregation behavior is not observed in ideal-Gibbs liquid component isotherms. It should be noted that these blends do not segregate in the bulk which has been observed by measuring a singular bulk glass transition temperature at different component concentrations[15].

It is clear that a combination of techniques has provided a deeper understanding into the fundamentals of polymer blend surfaces.

Chapter 8. References

[1] B. R. Liang, L. H. Pan and J. X. He, J. Appl. Polym. Sci. **66**, 217 (1997).

[2] C. D. Han ed. *Polymer blends and composites in multiphase systems*, (American Chemical Society, Washington, D.C., 1984, 206).

[3] P. S. Hope, J. G. Bonner and J. E. Curry, Pure and Appl. Chem. **68**, 1665 (1996).

[4] D. Zhang, R. Ward, Y. R. Shen and G. A. Somorjai, J. Phys. Chem. **101**, 9060 (1997).

[5] R. S. Ward, and K. A. White, US patent 5, 589, 563.

[6] K. A. White, R. S. Ward, R. S. Gill, F. Lim and S. C. Coviello, *Surface Modification of Segmented Polyurethaneureas via Oligomeric End Groups Incorporated During Synthesis, Surface Modification of Polymeric Biomaterials,* B.D. Ratner and D.G. Castner, eds. (Plenum Press, New York, 1996)

[7] S. Wu, *Polymer Interface and Adhesion* (Marcel Dekker, Inc., N. Y. 1982).

[8] Y. R. Shen, Nature **337**, 519 (1988).

[9] M. J. Rosen, *Surfactants and Interfacial Phenomena* (Wiley-Interscience: New York, 1985).

[10] A. W. Adamson, *Physical Chemistry of Surfaces* (Wiley-Interscience: New York, 1982).

[11] G. Bar, Y. Thomann, R. Brandsch, H. J. Cantow and M. H. Whangbo, Langmuir **13**, 14, 3807 (1997).

[12] L. Johnson, K. Kendall and A. D. Roberts, Proc. R. Soc. Lond. A **324**, 301 (1971).

[13] D. H. Gracias, D. Zhang, Y.R. Shen, Y.R. and Somorjai, G. A., Tribology Letters **4**, 3-4. 231 (1998).

[14] D. Zhang, D. H. Gracias, R. Ward, M. Gauckler, Y. Tian, Y. R. Shen and G. A. Somorjai, J. Phys. Chem. **102**, 32 (1998).

[15] K. A. White and R. S. Ward Mater. Res. Soc. Symp. Proc. **110** (1989).

Chapter 9. Comparison of nano and microscale friction mechanisms on polyethylene and silicon.

9. 1 Introduction: In the previous chapters, studies using the SFM to measure mechanical properties of polymer surfaces have been discussed. In chapter 4, the effect of the high pressure under conventional SFM tips was examined, which prompted the use of tips with larger radii of curvature. In this chapter we further examine the effect of changing the load and contact area in measurements of friction. This is because tribological measurements including that of friction force can be performed by various instruments, such as the scanning force microscope (SFM), the microprobe force microscope (MFM), and the classical pin-on-disk (POD) setup.[1-3] All of these instruments work in totally different load and contact area regimes. The SFM is used to apply loads in the nN range with tips of radii of curvature of the order of 100 nm. The MFM is a modified SFM that uses diamond tips of intermediate radii of curvature of 100 nm up to 20 mm and is capable of applying loads in the mN range. This instrument is well suited to bridge the gap between nanotribology and classical tribology. Finally, the POD can be used with a variety of tips of which blunt spherical tips of radii on the order of a few millimeters are the most common. While sensitive POD instruments can apply loads in the mN range, loads of the order of 1 N or higher can be applied with more rigid POD instruments. In the present investigation, friction experiments were performed on the same samples with all three instruments (SFM, MFM, and POD) using loads and apparent

contact areas varying by approximately eight orders of magnitude. The purpose of this study is to compare results obtained by the three instruments, and investigate possible trends that may have predictive value.

In this study we have chosen Low Density Polyethylene (LDPE), High Density Polyethylene (HDPE) and silicon as our samples. LDPE and HDPE have been investigated before with the SFM in chapter 4. In order to study the effect of a change in contact pressure and contact area on the polymers we have performed measurements on a "non-polymeric" sample, a silicon wafer (the 100 face of silicon). Apart from significant interest in the nano-/micro-tribological properties of silicon, the main structural material in microelectronics, the microstructure of silicon is insensitive to contact pressure variations and can be therefore used to determine whether transitions in the friction behavior of polymers associated with pressure-induced microstructure changes can be probed by the instruments used in this study. In view of profound differences in the microstructure and mechanical properties of polyethylene and silicon, increasing the contact load (mean pressure) may yield remarkably different sliding friction mechanisms.

9. 2 Experiments:

9. 2. 1 Sample Preparation: Pure granulates of low- and high-density polyethylene (Aldrich Chemical Co.) were heated and pressed onto a glass plate to produce flat disks. This was done to make flat samples as roughness introduces artifacts or "a topographic effect" into the friction measurements as

discussed in Chapter 4. Round disks of about 1.27 cm in diameter were cut from commercially available Si (100) wafers. Based on 10 mm x 10 mm surface area images, the root-mean-square (rms) roughness of the polyethylene and silicon disks was found equal to 30 and 4 nm, respectively.

9. 2. 2 Instrumentation and testing techniques

9. 2. 2. 1. SFM: A commercially available SFM (Park Scientific Instruments, Autoprobe MN5) was used to perform friction testing at the nanoscale. The tip deflection during surface probing is determined by a laser and a position-sensitive photodiode. Friction was measured by taking line scans at several predetermined repulsive loads. Several silicon probes with different spring constants and tip radii of 150 and 200 nm were used to apply normal loads between 5 and 700 nN. The sliding speed in all tests was fixed at 520 nm/s. The tip radius was estimated by scanning each probe tip over the very sharp wedges of a strontium titanate surface. To determine the magnitude of the friction force, the SFM was calibrated for each tip according to the technique of Carpick et al.[5] Calibration involves obtaining friction and topographic images on two well defined tilted planes (the 101 and 103 planes of $SrTi0_3$) at different loads, from which the instrumental dependence of the lateral signal on the vertical signal can be determined. Calibration of the exact frictional force for tips of radii of 100nm and 150 nm involved some error, as the method is ideal for much smaller tips of radii ~50nm. The errors are included with the results, and we are

still able to obtain a very good estimate of the friction coefficient so that we can compare it with that obtained by other instruments.

9. 2. 2. 2 MFM: Friction testing at the microscale was performed with a microprobe force microscope (MFM) consisting of an atomic force microscope (Digital Instruments, Nanoscope II) retrofitted with a capacitor force transducer (Hysitron Inc.). The vertical and lateral (friction) forces were determined by two independent capacitor plates that were previously calibrated for each tip. A 90° three-sided pyramidal diamond tip and a 60° conical diamond tip with radius of curvature equal to 100 nm and 16 mm, respectively, were used to scan the disk surfaces at loads in the range of 5-1000 mN and speeds of 400 nm/s.

9. 2. 2. 3 POD: A POD setup was used to perform friction testing at the milli-scale. A cantilever beam holding the pin (or flat plate) was wired with four strain gauges in a Wheatstone bridge configuration. The normal force was applied directly to the pin as a dead weight, and the friction force was measured by the strain gauges. The strain gauge output voltage was passed through an amplifier before collection by a data acquisition system. Friction coefficient data were collected continuously at a rate of 1.5 Hz. A blunt, diamond-coated tip with radius of 1.2 mm was used.

Table 9.1 summarizes the experimental parameters used in each instrument.

Instrument	Sliding speed	Sliding tip	Normal load
SFM	520 nm/s	Silicon (Radius = 150 nm)	5-20 nN
		Silicon (Radius = 200 nm)	20-700 nN
MFM	400 nm/s	Diamond (Radius = 100 nm)	2-100 mN
		Diamond (Radius = 16 mm)	2-1000 mN
POD	4.2 mm/s	Diamond (Radius = 1.2 mm)	20-275 mN

TABLE 9.1 Testing parameters for different instruments used in the study

To determine the prevailing deformation mode at the probe/substrate interface, images of each disk surface were obtained before and after testing with each instrument. Since SFM and MFM have both scratching and in situ imaging capabilities, surface imaging was performed with the same tip directly after testing at very light loads (of the order of a few nN). The wear tracks generated by the POD testers were observed with an optical microscope. The

experiments were performed at room temperature and relative humidity of approximately 40%

9. 3 Results and Discussion:

Assuming negligible plastic deformation and spherical probe tips, the contact area and pressure were obtained in terms of the tip radius, applied load, and elastic properties of the surfaces using the classical Hertz theory (discussed in Chapter 2) for the SFM and the POD tips. The elastic modulus of LDPE, HDPE, and silicon was assumed equal to 0.6, 0.9, and 98 GPa, respectively, and a Poisson's ratio of 0.3 for all materials. Where the penetration depth was large enough for the contact area to be affected by the global probe geometry (in the MFM), a projected contact area (and thus pressure) was calculated based on geometrical considerations.

These values are listed in Table 9. 2

Figs. 9. 1, 9. 2 and 9. 3 show the steady-state friction force as a function of normal load and apparent contact pressure for LDPE, HDPE and silicon obtained from sliding experiments performed with different instruments.

We have measured friction in all instruments in the repulsive regime, i.e. at loads at which the tip is pushed away from the sample. In the repulsive load range, all measurements reveal a linearity between friction force and load (or contact pressure).

Mat-erial	Instr-ument	Normal load	Apparent contact area	Contact pressure	Frict. coeff.
LDPE	SFM	5-200 nN	200 - 2800 nm^2	25-70 MPa	0.06
		200-700 nN	2800 - 6700 nm^2	70-105 MPa	0.17
	MFM	2-80 mN	1300 nm^2 - 1.9 mm^2	42-1625 MPa	0.18
		2-1000 mN	0.25 - 15 mm^2	8-67 MPa	0.13
	POD	17-85 mN	1900 - 5300 mm^2	9-16 MPa	0.41
HDPE	SFM	5-200 nN	200 - 2800 nm^2	25-70 MPa	0.06
		200-700 nN	2800 - 6700 nm^2	70-105 MPa	0.13
	MFM	2-30 mN	260 nm^2 - 0.059 mm^2	0.51-7.7 GPa	0.20
		30-80 mN	0.059 - 0.42 mm^2	0.19-0.51 GPa	0.39
		2-1000 mN	0.25 - 15 mm^2	8-67 MPa	0.11
	POD	17-210 mN	1900 - 9500 mm^2	9-22 MPa	0.17
Si	SFM	5-700 nN	17 - 450 nm^2	0.3-1.54 GPa	0.03
	MFM	10-70 mN	1060 - 3900 nm^2	9.4-18 GPa	0.25
		2-1000 mN	0.011 - 0.66 mm^2	0.19-1.51 GPa	0.11
	POD	17-270 mN	81 - 500 mm^2	210-540 MPa	0.08

TABLE 9.2 Friction coefficient of HDPE, LDPE and Si versus normal load, contact area, and mean pressure measured with the SFM, MFM and POD

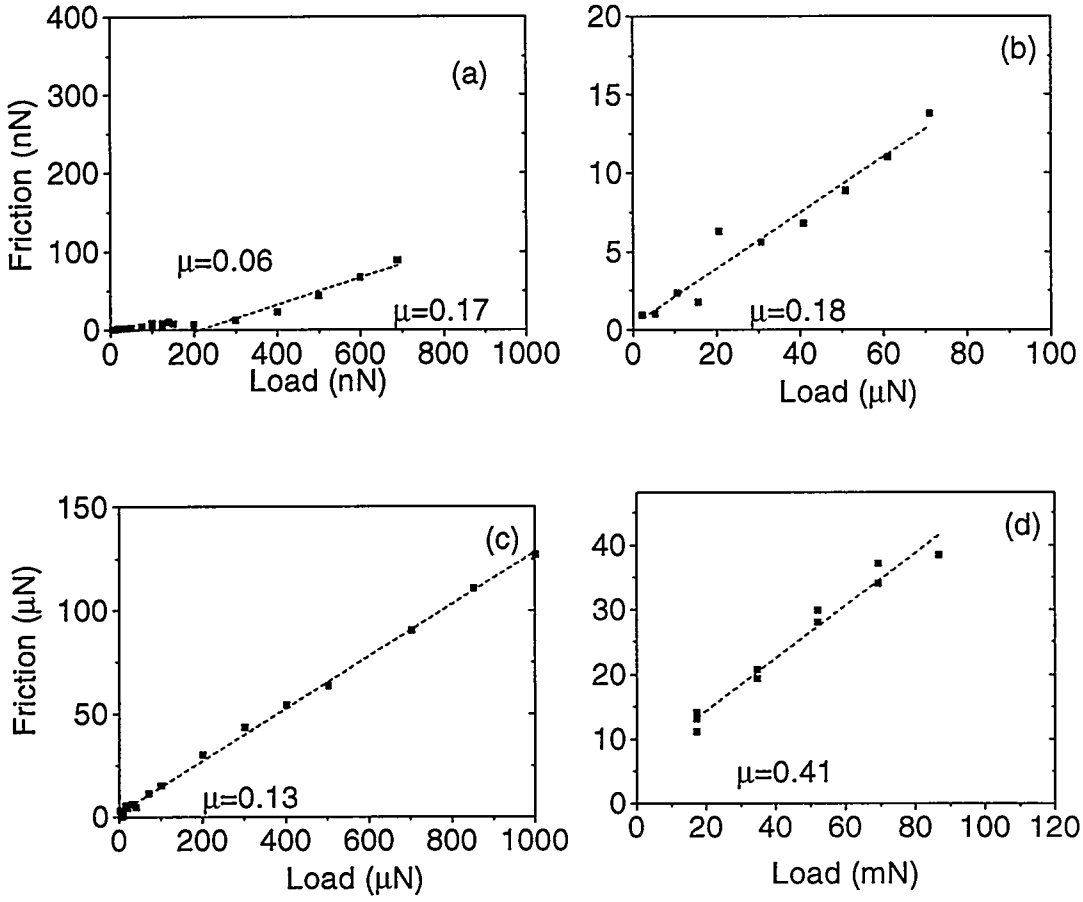

Figure 9.1 Friction force versus load for LDPE obtained with (a) SFM, (b) MFM (100-nm tip radius), (c) MFM (16-mm tip radius), (d) POD (1.2-mm pin radius).

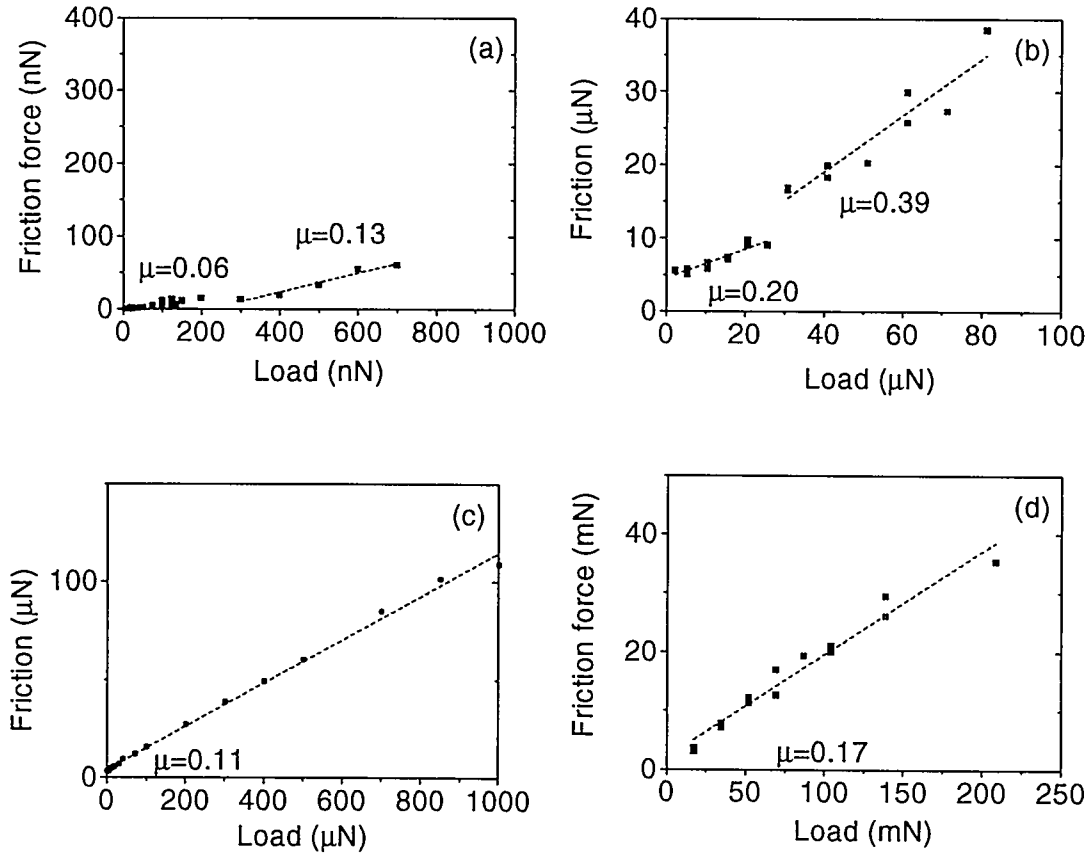

Figure 9.2 Friction force versus load for HDPE obtained with (a) SFM, (b) MFM (100-nm tip radius), (c) MFM (16-mm tip radius), (d) POD (1.2-mm pin radius).

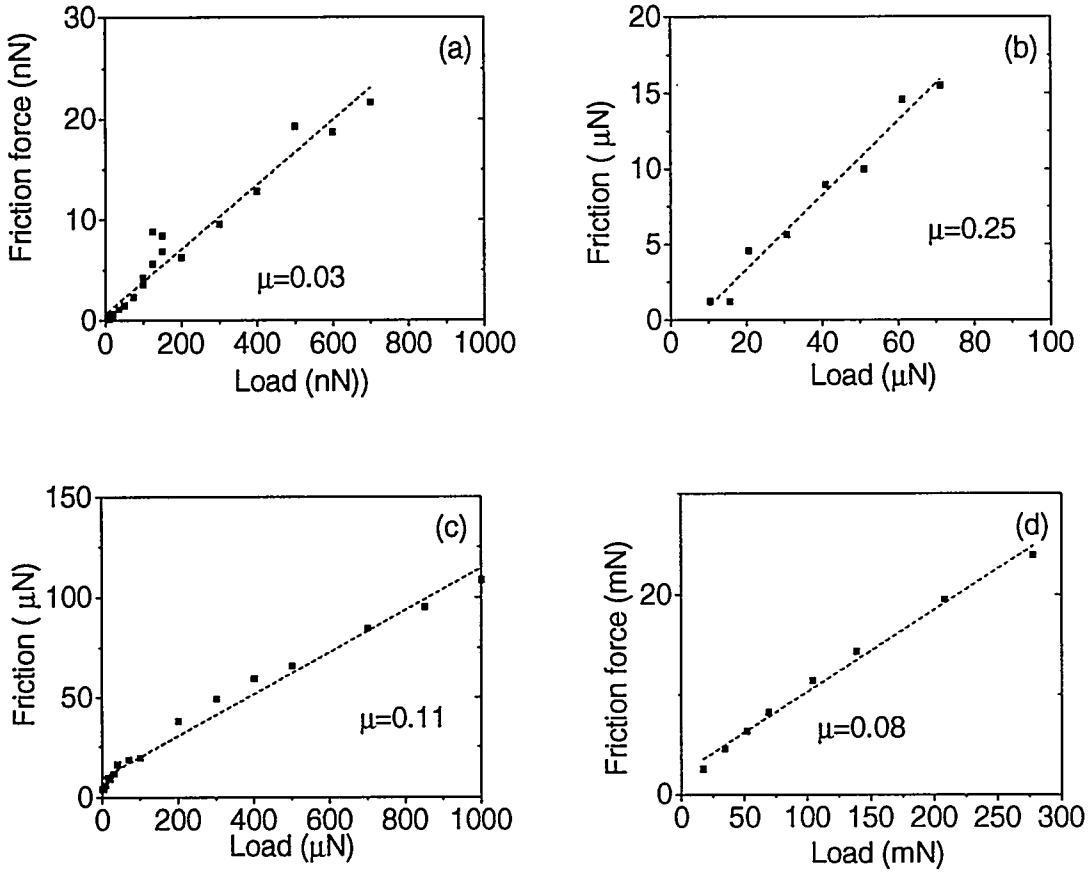

Figure 9.3 Friction force versus load for Si obtained with (a) SFM, (b) MFM (100-nm tip radius), (c) MFM (16-mm tip radius), (d) POD (1.2-mm pin radius).

This linear relationship has been observed in previous measurements reported in Chapter 4 and has been attributed to a pressure dependence of the shear strength of the polymer. Alternatively since the entire friction vs load curve

in these measurements was not obtained in a single measurement, the statistical nature of the measurement might preclude any observation of the exact functional dependence of the friction on the load. Due to the linear nature of the curves we have chosen to characterize them by a coefficient of friction, *m*, which is the slope of each friction trace.

The values for the friction coefficient are listed in Table 9.2.

A transition in friction within each load range was determined from the change of the slope of the friction force response.

From the values obtained we can comment on the effect of contact pressure, contact area, nature of the tip and the penetration depth.

9. 3. 1 The effect of contact pressure: From the values of friction coefficients obtained we see that as we increase the contact pressure the friction coefficients increase. This is more easily observable if we compare friction coefficients within a particular instrument. In SFM measurements on LDPE and HDPE, as the pressure increases from 25 to 105 MPa the friction coefficient increases from 0.06 to 0.17 and 0.06 to 0.13 respectively. In MFM experiments on LDPE as the pressure is increased from 8 to 1625 MPa the friction coefficient increases from 0.13 to 0.18. For HDPE when the pressure is in the range 8-67 MPa, the friction coefficient is 0.11 whereas when the pressure is 510-7700 MPa the friction coefficient is 0.20. For Si too, we observe in MFM measurements that as we increase the pressure from 0.19 to 18 GPa the friction coefficient increases form 0.11 to 0.25.

Typically small friction coefficients are expected at low pressures, and is indicative of predominantly elastic friction, with little or no wear of the sample. This low friction coefficient is observed on all the three samples. At high contact pressures we observe an increase in the coefficient of friction. This is observed in the SFM and MFM measurements on all three samples and can be explained by the onset of plastic deformation and the wear of the sample. An increase in friction coefficients has been observed in wear related friction due to the excess force required to cause plastic deformation. Since Si has a much higher yield strength it resists deformation and no discernible plastic deformation occurs at contact pressures even as high as 1 GPa, which keeps the friction coefficient low. To ensure that plasticity was significant in the load range of 5-1000 mN in the MFM, indentations were performed with the MFM using a 90° three-sided pyramidal diamond tip with a 100 nm radius. Fig. 9.4 shows representative results of loading/unloading indentation force curves obtained from these experiments with maximum loads about 5, 12, and 27 mN on LDPE. The development of force hysteresis curves indicates that plastic deformation occurred even at loads as low as 5 mN. The good agreement between the three loading paths is illustrative of the instrument's capability to reliably probe the mechanical behavior of the materials. Also it should be noted that the geometry of the MFM indentor is pyramidal and conical and results in higher contact pressures than spherical tips with the same radius of curvature. It was possible

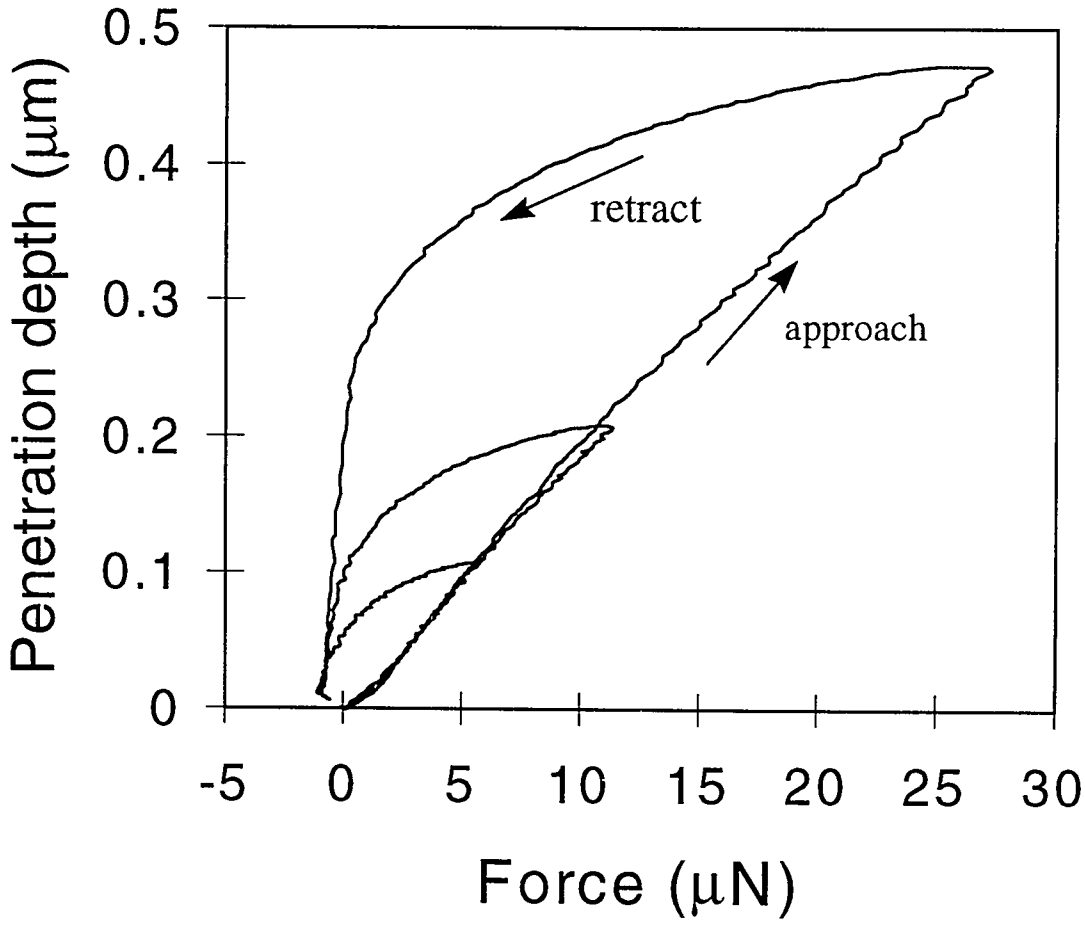

Figure 9.4 Indentation force versus penetration depth curves for LDPE obtained with a 90° three-sided pyramidal diamond MFM probe of radius 100 nm.

with the SFM to observe wear tracks on the surface by taking topographic images subsequent to the friction measurements. Shown in Fig. 9.5 is a wear track on the polymer at pressures of ~150 MPa. The POD measurements reveal high friction coefficients on the polymers which is very high compared to that expected at the pressure calculated for Hertzian contact in the POD. In the POD

experiments although the pressures listed in Table 9.2 are low, the real pressure

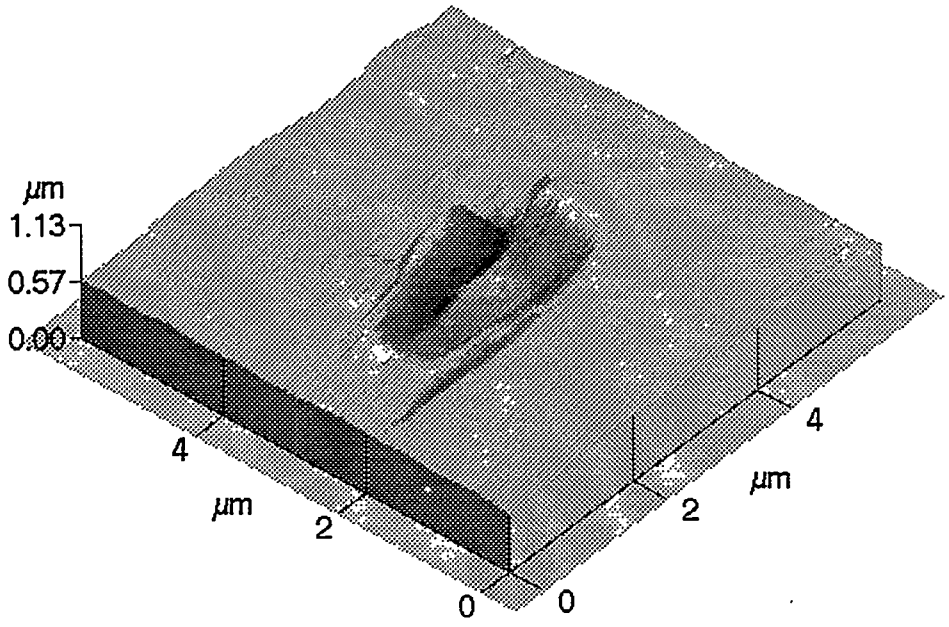

Figure 9.5 Wear groove observed on LDPE at contact pressures of ~150 MPa with SFM.

at the contact can be quite different and extremely high. This is due to multiple asperity contact, which results in a higher pressure at the contact of each asperity. However we observe low friction coefficient for the silicon surface (typical of a diamond tip sliding on a silicon surface[5]) in the POD measurements while we have large rises in the friction coefficient on the two polymer surfaces.

This implies that in addition to the contact pressure other parameters are influencing the friction measurements.

9. 3. 2 The effect of contact area: We observe that as the contact area increases to the order of a square micron, the coefficients of friction for the polymers increase much more than that observed on silicon. Now it has been reported that macroscopic sliding of polyethylene promotes the alignment of crystalline platelets (lamella) parallel to the direction of sliding.[6-7] Since the typical lamella size is about 20-50 nm, it is not likely that the very sharp probe tips used in the SFM and MFM instruments induced lamella alignment. With a much blunter tip, however, the real contact area is significantly larger and lamella alignment is enhanced. This may explain the larger friction coefficients observed in pin on disk measurements and the high friction coefficient of 0.39 observed with the MFM on HDPE.

9. 3. 3 The effect of penetration depth: It is important to distinguish which part of the sample is being deformed elastically / worn off plastically while performing friction measurements. This becomes important in the case of silicon. Silicon is known to contain a native oxide layer, which is only a few nm thick. At low contact pressure we are measuring the friction on the oxide layer. Since the friction coefficients of the oxide layer and pure silicon are different, we would get different friction coefficients at different penetration depths. This is clearly seen in the measurements, In the SFM measurement on silicon, we observe an

extremely low friction coefficients, the penetration depths in these experiments is of the order of a nm. Hence we are measuring the friction of the oxide layer. In the MFM measurement in the same pressure regime, (0.19 - 1.51 GPa) we have

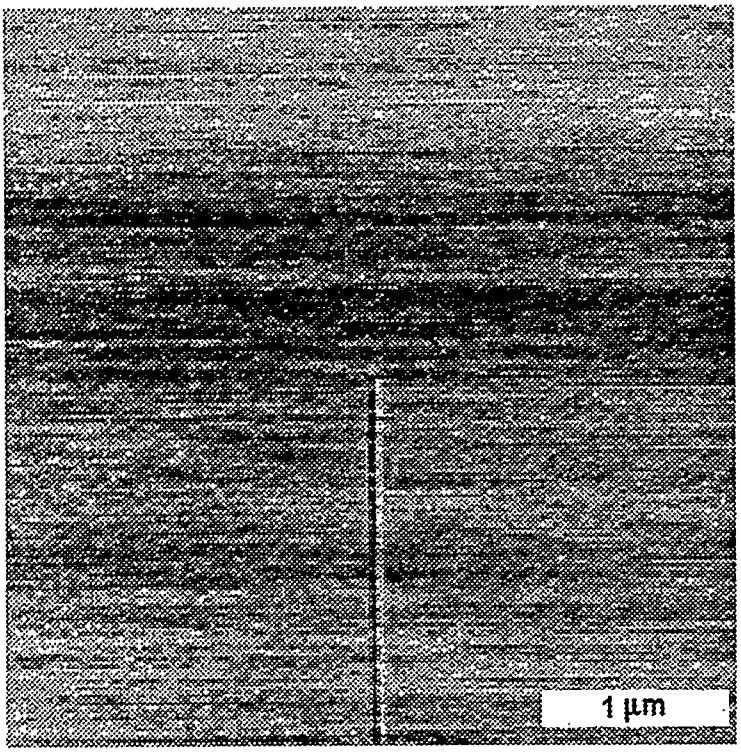

Figure 9.6 SFM image of Si(100) showing a scratch produced by an MFM probe with tip radius of 100 nm at a load of 70 mN.

penetration depths of the order of 100nm. In this region we are deforming both the oxide and the silicon layer elastically and hence the friction coefficient is larger. If this is true then we can conclude that the friction of the oxide layer of silicon is lower than that on silicon. Rupturing of this layer results in higher friction coefficients as seen at high pressures with the MFM (9.4-18GPa). Plastic

deformation of the oxide layer results in high friction coefficients as is observed in friction involving wear. Figure 9.6 shows a scratch obtained on Si in this regime.

9. 3. 4 Effect of chemistry of the tip: We have observed no significant difference in friction coefficients measured with the Silicon or Diamond tips especially on the polyethylene samples. This implies that either the surface chemistry and mechanical properties of the two tips are similar, or that the friction process is dominated by the polymer deformation and is independent of the chemical nature of the much more rigid tip. It has been observed that polymer friction (low surface energy) behavior does not depend strongly on the chemical nature of the rigid indentor. It has been observed that similar friction coefficients were measured during sliding with different metal indentors[8], which supports the latter view point.

In summary, the results for polyethylene show that the friction behavior strongly depends on the real contact area which affects the microstructure. The average lamellae size of polyethylene is dictated by crystallization thermodynamics and is approximately 20-50 nm, depending on the processing temperature, pressure, and level of undercooling. Hence, the profound role of lamellae alignment parallel to the direction of sliding can only occur with relatively blunt probes producing large contact areas. Thus, a significant change in the friction behavior can occur at a given contact pressure by increasing the contact area. In addition, increasing the load (and thus the pressure) without

changing significantly the real contact area causes a transition from elastic to plastic surface deformation characterized by the dominance of surface adhesion and plowing friction mechanisms, respectively. However, even within the elastic deformation regime, a change in the friction behavior might be observed due to the change of the polyethylene shear strength with pressure. The results obtained for silicon do not show a dependence of friction on contact area. This is expected because silicon possesses a very different microstructure. However, a transition from elastic to plastic deformation accompanied by a change from adhesion to plowing friction mechanisms was observed at contact pressures sufficiently high to cause rupture of the native oxide film.

9. 4 Conclusion: In this chapter an experimental investigation of the dynamic friction behavior of low- and high-density polyethylene and silicon was performed with different instruments at normal loads in the ranges of 5×10^{-9} to 0.3 N. All materials showed several friction regimes. A transition from elastic to plastic deformation accompanied by a change in the dominant friction mechanism from adhesion to plowing was observed with increasing contact pressure for all materials. In addition, a dependence of friction on the apparent contact area was observed for polyethylene. This was associated with the strong effect of pressure on the shear strength of polyethylene and the modification of the near-surface microstructure through the alignment of crystalline phases (lamellae) parallel to the sliding direction. This change of the polymer microstructure was not encountered with fine probe instruments producing real

contact areas of the order of the lamellae size. The results of the present study illustrate that significantly different friction properties can occur at different scales and provide new insight into frictional transitions over a wide range of loads and contact areas.

Chapter 9. References

[1] B. K. Yen, J. Mat. Sci **32**, 821 (1997).

[2] M. A. Spalding, D. E. Kirkpatrick, and K. S. Hyun, Poly. Eng. Sci. **33**, 423 (1993).

[3] B. Bhushan and S. Venkatesan, J. Mat. Res. **8**, 1611 (1993)

[4] D. F. Ogletree, R. W. Carpick, and M. Salmeron, Rev. Sci. Instrum. **67**, 3298 (1996).

[5] B. Bhushan and X. Li, J. Mater. Res, **12**,1 (1997), 54

[6] N. P. Suh, *Tribophysics* (Prentice-Hall, Englewood Cliffs, NJ, 1986).

[7] C. G'Sell, B. Paysant-Le Roux, A. Dahoun, C. Cunat, J. von Stebut, and D. Mainard, *10th Int. Conf. On Deformation, Yield and Fracture of Polymers*, The Institute of Materials, London, U.K., 1997, pp. 57-60.

[8] F. P. Bowden and D. Tabor, *The Friction and Lubrication of Solids* (Oxford University Press, UK, 1964).

10. Miscellaneous Experiments.

10. 1 Introduction: In this chapter three more experiments will be described in which the SFM was used to map out mechanical properties of polymer surfaces. The first involves the structural changes occurring in the polymer surface during electron beam damage of PolyMethylMethacrylate (PMMA), which is used as a resist in lithography. The second involves the study modification of polymer surfaces with diamond like carbon (DLC) deposited by plasma techniques. Finally structural changes in a liquid crystalline polymer Vectra-A under microdeformation will be discussed.

10. 2. Electron Beam Damage of PMMA: PMMA is used as a resist in lithographic fabrication of micro and nano structures[1]. The primary use of these structures is in very large scale integrated circuit device manufacture. Typically the first step in this process is to spin coat this resist on a silicon wafer, the wafer with the resist is then baked. A collimated electron or photon beam is then used to transfer a required pattern onto the wafer. In this step a high energy electron beam is focused on the resist. The beam causes damage to the polymer. After this step the exposed polymer is then selectively removed, while the unexposed portions of the polymer remain intact on the substrate. This is called developing, whereby a solvent is used to selectiveiy dissolve the damaged part of the polymer. Later metal may be deposited and the undamaged portion of the polymer dissolved to produce the structure. In our study the elastic

Topography

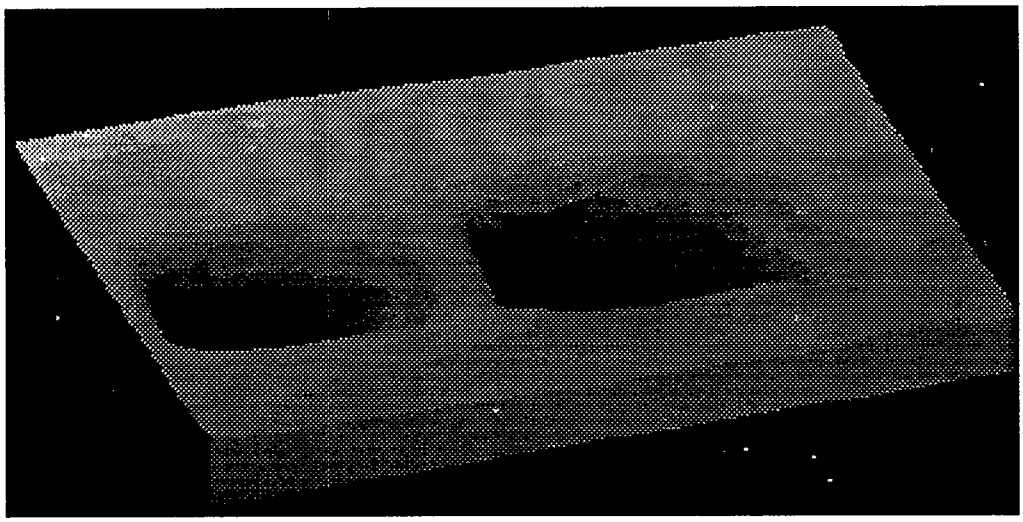

2.1 μm x 3.2 μm

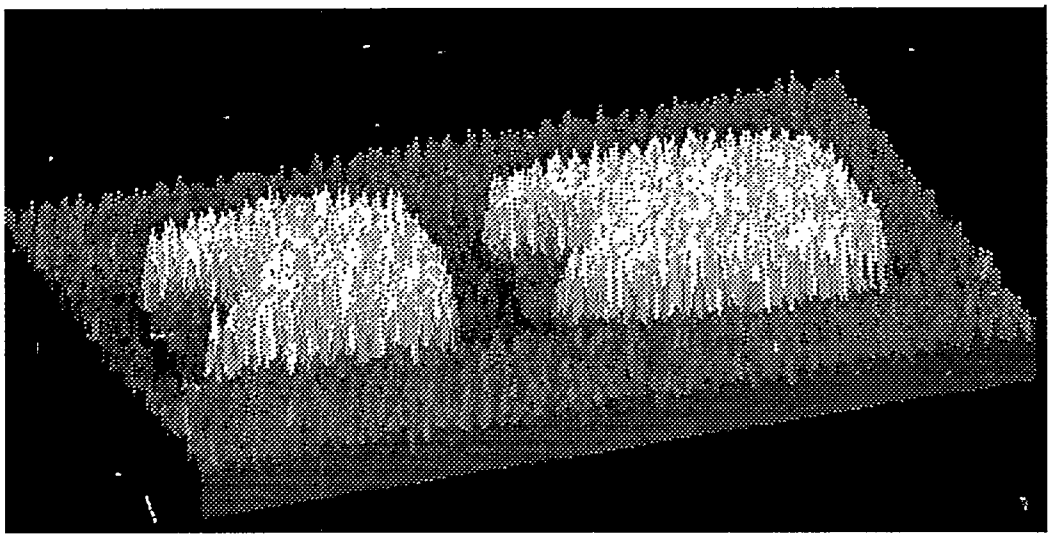

Compliance

Figure 10. 1 Topography and compliance images of damaged and undamaged polymer. The damaged polymer appears a little depressed in the SFM topographic image, and is more compliant. (lower modulus)

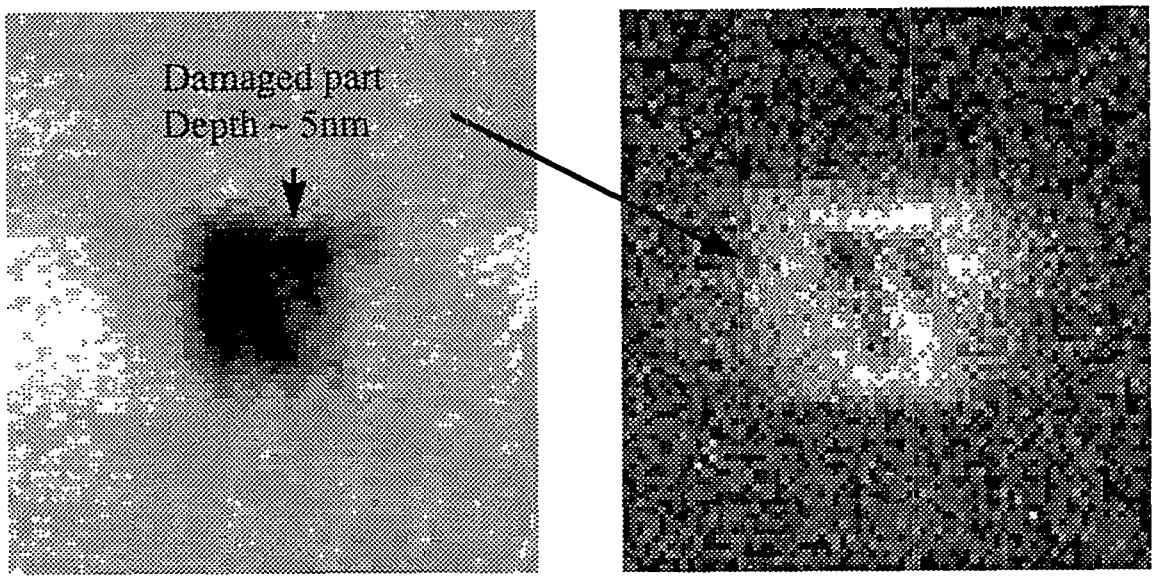

Figure 10. 2 Topography and compliance image of damaged and undamaged PMMA prior to development. The modulus of the damaged polymer is lower than that of the undamaged polymer.

modulus of the polymer was investigated after damage with the electron beam. Figs. 10.1 and 10.2 show topography and compliance maps of damaged regions of the PMMA after exposure to electron beams of the order of 1 milli Coulomb / cm^2, 30 keV. The exposed area can be observed in the topographic map, this may be either due to physical or chemical removal of some polymer during the e-beam process or due to imaging process of the SFM itself, which depends on the elastic modulus of the sample. When the surface elastic modulus is mapped by the SFM by oscillating the cantilever as described in Section 4. 3. 4, a

contrast is observed in the oscillation amplitude (compliance) over exposed and unexposed areas as seen in Figs. 10. 1 and 10. 2 This is indicative of a lower elastic modulus of the damaged polymer by the electron beam. This can be explained by the fact that the electron beam induces polymer chain cleavage, en route to a reduction in the molecular weight of the sample which results in a lower modulus.

By imaging the structures formed at the end of the lithographic process which have sharper edges than the tip, the radius of curvature of the tip was determined. Contact mechanics was then used to obtain an estimate of 3 GPa for the elastic modulus of the undamaged part of the polymer and 5 GPa for that of the damaged portion of the polymer.

10. 3 Surface modification of polymers with Diamond Like Carbon (DLC)[2]:

The aim of the project was to enhance the mechanical properties (decrease the friction and increase the modulus) of polyolefin surfaces by pulsed plasma deposition of amorphous carbon. The idea behind this was to retain the useful bulk properties of polymers (flexibility) while modifying the surface to a hard scratch resistant finish of DLC. The polymers used were low density polyethylene LDPE, and isotactic (IPP) and atactic polypropylene (APP). The polymers were prepared by heating on a glass plate and cooling, in a manner such that r.m.s. roughness was around 20nm on 100micron x 100micron areas, and around 2nm on a 50nm x 50nm area. The surface of the polyolefin was not

pretreated to enhance adhesion of the coating. The friction and elastic modulus were measured with SFM using methods described in Chapter 4.

Large scale topographic images were also taken. Deposition of the coatings was done under different bias voltages (supposed to increase the adhesion of the DLC film to the polymer). Moreover a pulsed source was used to reduce charging effects in the polymer. Previous studies[2] have focused on the deposition of thick films on polymers, and we wished to investigate the behavior of thin films.

The parameters used in our measurements were: tip radius: large 1000nm (reason is to reduce pressure and inelastic deformation). Loads applied for elastic modulus maps: 600-800nN which implies probing depths of 1-10nm.

The thickness of the DLC coating ~ 6nm-20nm

After looking at the penetration depth and thickness of the film one can conclude that the deformation is going to be partly borne by the coating and partly by the sample. This is crucial, because if we have a stiff coating on a less stiff substrate (i.e. the polymer) the two will behave as a composite.

This can be seen more clearly if we consider two springs, of force constants k (coating) and k' (polymer) in series. Now if a load is applied then the composite behaves as a spring with force constant $\frac{kk'}{k+k'}$. In our case one of the springs is the coating and the other is the polymer. Now it is known that the bulk elastic moduli of such carbon is of the order ~100GPa , while that of the polymer is

Polymer	Elastic Modulus	Friction Coefficient
LDPE	~0.8 GPa	0.3
LDPE+ (0 V, 250 shots DLC)	0.3 GPa	0.57
LDPE+ (-100 V, 250 shots DLC)	0.35 GPa	0.44
LDPE+ (-200V, 250 shots DLC)	0.7 GPa	0.35
APP	0.16 GPa	0.75
APP (0 V, 250 shots DLC)	0.18 GPa	0.42
APP (-200 V, 250 shots DLC)	0.28 GPa	0.37

Table 10. 1 Values of elastic modulus and friction coeff. measured on LDPE which show that as the bias voltage is increased while depositing the DLC, the friction coeff. of the resulting surface decreases and the modulus increases. However these changes for LDPE (representative of other polymers like IPP) are worse than the original polymer due to lack of adhesion of the coating to the polymer. For APP only there is an improvement of the mechanical properties of the polymer due to the coating.

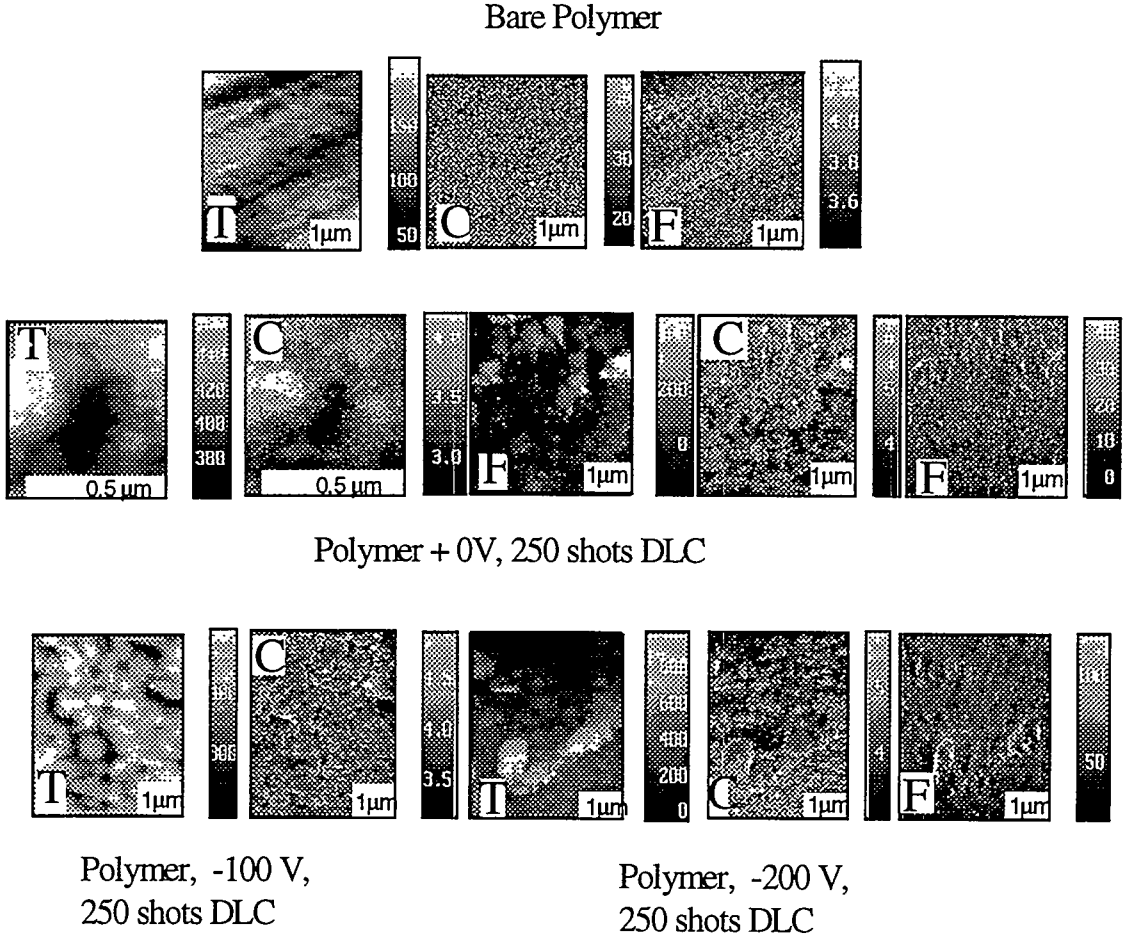

Figure 10.3 Topographic (T), Compliance (C) and Friction (F) images of the bare polymer IPP and DLC coated IPP while biasing the sample at 0 V, -100 V and -200 V. As can be seen the coatings do not seem to adhere well to the polymer and peel off, causing considerable debris and roughness on the surface.

~1GPa. Thus if the loading were ideal the two springs would behave as $k>k'$ and the force constant measured would be $\sim k'$. Thus even though the elastic

modulus values appear not to have changed much from the polymer it should be noted that the measurement has been influenced by the composite beam effect.

We observed a correlation between bias applied during deposition and the enhanced properties i.e. lower friction and higher elastic modulus with larger bias voltages. This can be explained by the fact that at high bias voltages the ions impinging the surface have high kinetic energy and can do chemistry with the surface which may improve the adhesion of these species to the surface. This can be seen in the results on LDPE and APP presented in Table 10. 1. However in only APP the properties of the coated interface were better than the original polymer, i.e. friction was higher and elastic modulus lower.

It was clear from the study that the reason for the worse performance of the DLC coated polymers was that the coatings did not adhere well. From the Fig. 10. 3 we can see platelets and the coated sample seems to have a lot of debris (peeled off coating) as compared to the bare IPP surface. The figure includes topography maps, amplitude damping (indicative of the elastic modulus) and friction. Note experiments were done on the samples 6 months after they were prepared and it is possible that the coatings peel off with time. One might imagine that a hard coating on a soft substrate will be in a stressed state, and a long time period between preparation and measurements could only have made the situation worse. In the future it would be interesting to pre treat the polymer (perhaps by oxidation) surface to enhance its adhesive properties. However in the present study we can see how the SFM very readily observes this peeling off, of the coating.

10. 4. Microdeformation mechanism in Vectra-A: Vectra (Hoechst Celanese Corporation) is an aromatic thermotropic copolyester of para hydroxy benzoic acid (HBA) - co - para hydroxy napthoic acid (HNA) with superior mechanical and thermal properties as compared to conventional polyesters[3]. The samples obtained consist of 73 % HBA and 27 % HNA. The rods were extruded at 282-288 ^{0}C and cut into pellets. Knife edged glass pieces were used in a

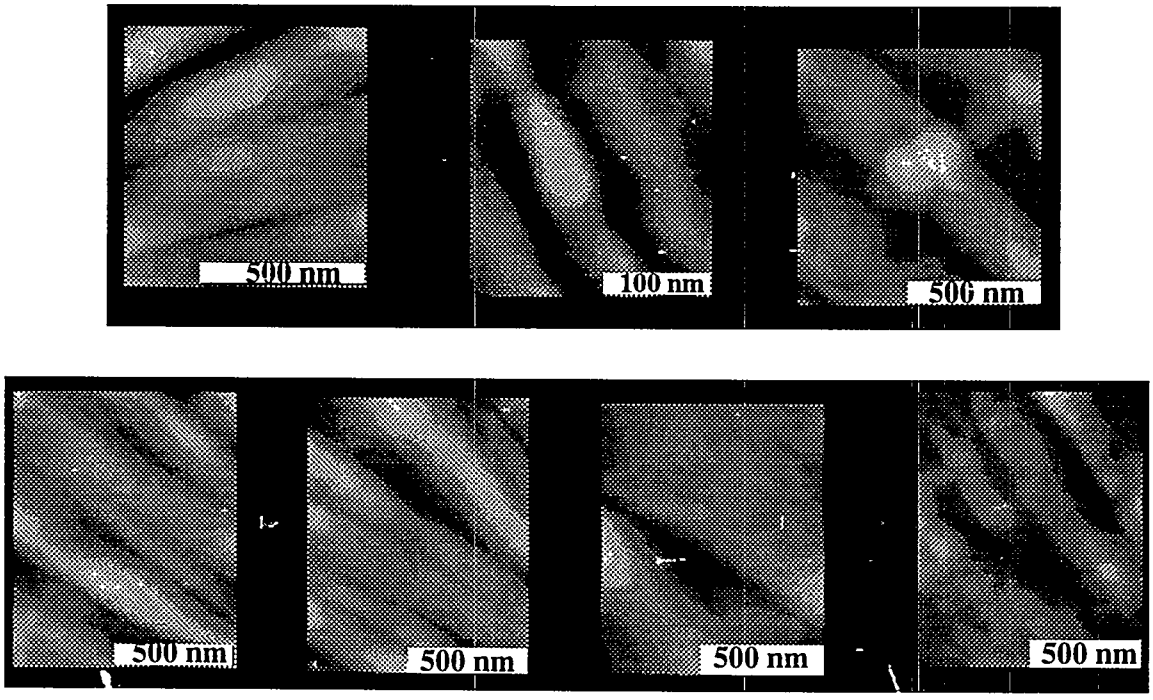

Figure 10.4 Topographic contact mode images of Vectra-A which show a fibrillar hierarhcy in the range of 50-500 nm.

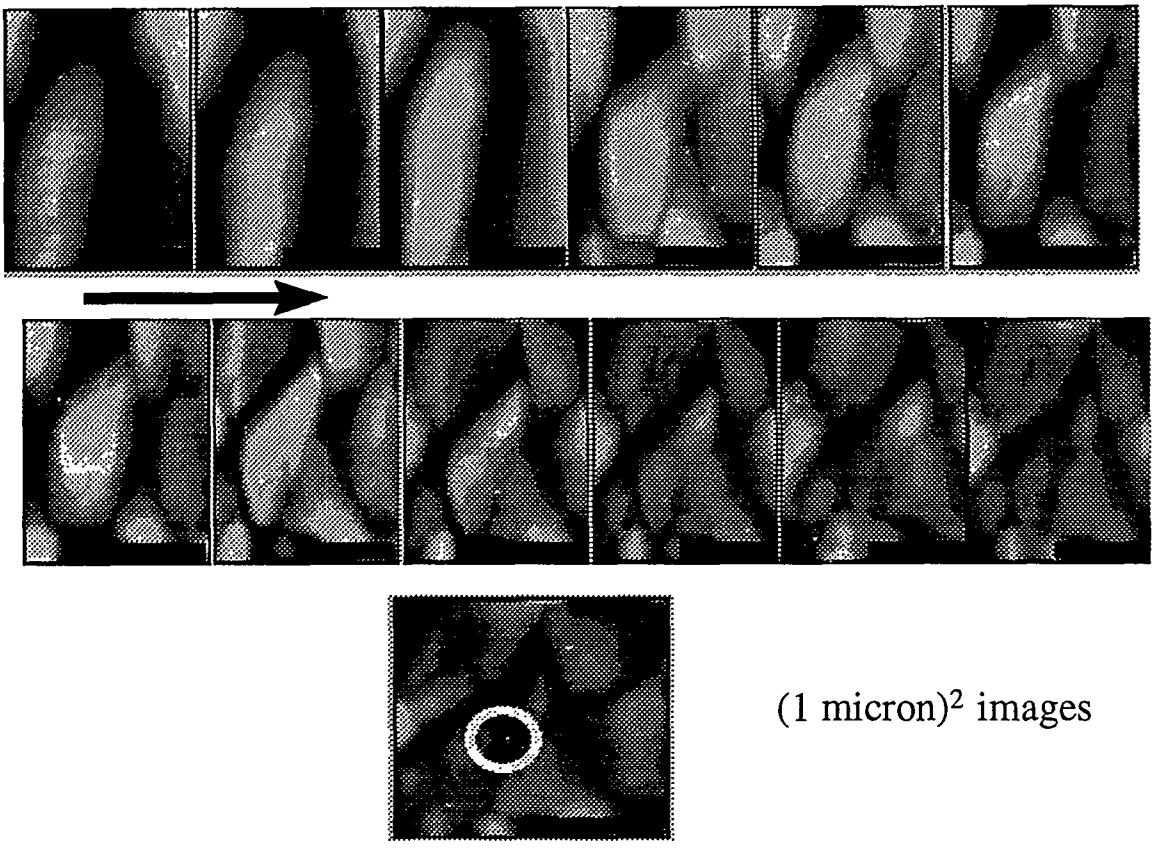

Figure 10.5 A series of images taken on the same area on the Vectra surface. In between images the tip is lifted off the surface and then pushed back down into the center of the image field. The area is then subsequently imaged to identify any change in the polymer microstructure. In the first row of images, the fibril twists to relieve stress. In the next set the fibril is depressed towards the bulk of the polymer. Finally in the last image an indent is formed.

microtome to section the pellet. The skin and the top few layers were discarded thereby exposing the inner layers. The pellets were then stored in a dissector in

a dry nitrogen environment. The bulk properties and morphology of Vectra has been elucidated in earlier studies[4-5]. A hierarchy of fibres was imaged with diameters ranging from 50 nm to 500 nm. Some of these images are shown in Fig. 10. 4.

Perhaps more interestingly, the plastic deformation mechanism of the polymer to applied load was investigated by nanoindentation experiments with the SFM. In this experiment loads of the order of the order of 500 nanonewtons were applied to the polymer surface, by pushing the SFM tip into the surface. The tip was then retracted and the polymer surface was imaged in the contact mode. Typically the time elapsed between deformation and imaging was on the order of 1 minute. These images are presented in Fig. 10.5. The stress is being applied to the center of the image. Initially the micorfibril twists to relieve the stress applied to it. This implies that this deformation mechanism is the most facile. More stress applied to the polymer dissipates itself by depressing the fibril into the bulk. This is due to the voids present in the bulk polymer. If the tip is pushed again into the surface, it results in a hole being formed. This is plastic deformation of an indent. If the total loads are added from image to image, the total load required to produce the twist is 19 micronewtons. A further 70 micronewtons was required to produce the indent which is around 50 nm in diameter.

10. 5 Conclusions: In this chapter the viability of the SFM to probe key mechanical properties of polymer surfaces has been further demonstrated. It has

been shown that the mechanical properties of polymers are dramatically influenced by physical and chemical properties of the surfaces, i.e. e-damage, adhesion. Finally a novel way to use the SFM to study micro structural deformation mechanisms has been discussed.

Chapter 10. References:

[1] M. X. Yang, D. H. Gracias, P. W. Jacobs and G. A. Somorjai, Langmuir **14**, 1458 (1998).

[2] John J. Pouch and Samuel A. Alterovitz *Properties and characterization of amorphous carbon films* (Aedermannsdorf, Switzerland ; Brookfield, VT, USA : Trans Tech Publication, Materials science forum ; c1990 v. 52-53).

[3] L. C. Sawyer, R. T. Chen, M. G. Jamieson, I. H. Musselman and P. E. Russell, Journal of Material Science Letters **11**, 69 (1992).

[4] J. Blackwell, G. Lieser, and G. A. Gutirrez, Macromolecules **16,** 1418 (1983).

[5] U. W. Gedde, D. Buerfer and R. H. Boyd, Macromolecules **20**, 573 (1987).